Mechanical and Image-Based Assessments of Histotripsy and Tumor-Induced Changes in Osteosarcoma Tumor-Bearing Bone

Preeya F. Achari

Dissertation submitted to the Faculty of the
Virginia Polytechnic Institute and State University
in partial fulfillment of the requirements for the degree of

Doctor of Philosophy
in
Biomedical Engineering

Caitlyn J. Collins, Chair
Eli Vlaisavljevich
Joanne Tuohy
Raffaella De Vita
Ashley Weaver

February 23rd, 2026
Blacksburg, Virginia

Keywords: Bone, Biomechanics, micro-CT, Focused ultrasound, Finite element analysis

Mechanical and Image-Based Assessments of Histotripsy and Tumor-Induced Changes in Osteosarcoma Tumor-Bearing Bone

Preeya F. Achari

(ABSTRACT)

Osteosarcoma (OS) is a rare and aggressive bone cancer that often requires invasive limb-resection or limb-salvage surgery, which may lead to significant biomechanical challenges and an elevated risk of fracture. Histotripsy, a noninvasive focused ultrasound therapy, offers a promising alternative by selectively ablating tumor tissue while preserving surrounding structures. Although the safety and feasibility of OS tumor histotripsy ablation has already been demonstrated, its effects on the structural and mechanical integrity of OS-affected and healthy bone remain unknown. This knowledge is critical for advancing histotripsy as a safe, noninvasive limb-sparing strategy for OS. This dissertation developed predictive finite element (FE) models to evaluate the biomechanical effects of histotripsy on OS-affected bone through two aims. Aim 1 assessed histotripsy's impact on the structural and mechanical properties of OS-affected bone in an *ex vivo* canine model using mechanical testing and high resolution CT imaging. Aim 2 investigated histotripsy's effects on whole-bone mechanics in an *ex vivo* murine model during tumor progression, integrating imaging data into FE models to predict fracture risk and evaluate treatment outcomes. The findings of this study establish critical data on the biomechanical effects of histotripsy on both healthy and diseased bone, advance predictive image-based FE modeling accuracy, and support the clinical translation of histotripsy as a noninvasive limb-salvage strategy for OS.

Mechanical and Image-Based Assessments of Histotripsy and Tumor-Induced Changes in Osteosarcoma Tumor-Bearing Bone

Preeya F. Achari

(GENERAL AUDIENCE ABSTRACT)

Osteosarcoma (OS) is a rare and aggressive bone cancer that primarily affects children and older adults. Currently, the standard treatment option involves surgically removing part or whole of the affected limb or attempting more complex surgeries to save it. These procedures can lead to infection, reduced mobility, and can weaken the bone and render the patient more susceptible to bone fractures. A novel treatment alternative called histotripsy uses sound waves to break down tissue without needing surgery. While early studies show that histotripsy can safely and effectively target bone tumors, it is not yet clear how this treatment effects the strength of the bone itself. This dissertation studies how histotripsy affects the structural stability and strength of OS-affected and normal bone through two aims. In Aim 1, pieces from the bones of canine OS patients were mechanically tested to see how histotripsy changed the structure and mechanical properties of clinical OS-affected bone. In Aim 2, whole mouse bones with tumors were studied over time, using advanced imaging scans and mechanical testing to track changes in bone structure and strength. Computational models were then developed to predict if and where a bone may fracture under bodyweight conditions. These results provide important knowledge about how histotripsy affects both healthy and OS-affected bone. This work improves the ability to predict bone strength after treatment and supports the future use of histotripsy as a safe, noninvasive treatment alternative for OS patients.

Dedication

This dissertation is dedicated to my family. To my parents, Zhanna and Rajeev, who have shown me unwavering love, encouragement, and support throughout my academic journey. To my siblings, Avinash, Meera, and Shaila, without whom I would not be who I am today. Everything I do is for you.

Acknowledgments

Firstly, I'd like to wholeheartedly thank my PI, Dr. Caitlyn Collins. From the beginning, you welcomed me into your lab and showed me what it takes to be a great researcher. I couldn't have asked for a more motivating, supportive, and inspiring mentor.

To my fellow labmates and dearest friends, how lucky I am that I found both in the same place. Ed, Jandi, and Garrett, this one's for you.

To my committee, Dr. Eli Vlaisavljevich, Dr. Rafaella De Vita, Dr. Joanne Tuohy, and Dr. Ashley Weaver, thank you so much for providing your expertise and steering me in the right direction whenever I needed it.

To SBES at Virginia Tech, thank you for providing me with the best friends I could have asked for, the most wonderful professors I could have worked with, and all the free food that got me through it.

Contents

List of Figures

List of Tables

Chapter 1

Introduction

1.1 Motivation

Osteosarcoma (OS) is a rare, aggressive bone cancer and one of the most common malignancies in children and adolescents[1]. The survival rate for OS has not improved in decades due to the refractoriness of the metastatic disease to therapy. The 5-year survival rate for patients with primary OS is approximately 75%; however, this rate drops dramatically to 30-35% for those who present with pulmonary metastases[1–3]. While the standard combination of surgical resection, chemotherapy, and radiotherapy has improved patient outcomes, many patients remain ineligible for surgical resection due to tumor characteristics or disease progression[4]. Those who do continue with treatment may suffer from metastasis, infection, and reduced limb mobility and function post-treatment[5,6]. Therefore, there is a critical need for novel, noninvasive treatment options for OS.

Therapeutic ablation techniques, including high-intensity focused ultrasound (HIFU)[7], radiofrequency[8], and microwave ablation[9] are currently used for tumor ablation or palliative care in lieu of surgical resection. These approaches rely on thermal mechanisms to destroy tissue, which has demonstrated efficacy but requires careful management to control heat propagation and subsequent damage to surrounding tissues. In contrast, histotripsy is a noninvasive, nonthermal focused ultrasound (FUS) ablation technique that mechanically destroys tissue through controlled acoustic cavitation[10]. Previous histological *ex vivo* studies on canine OS tumor-bearing bone have shown that histotripsy effectively ablates primary

OS tumor cells without causing cell death or damage to normal, surrounding tissue[11–13]. However, the genomic instability exhibited by OS results in a highly heterogeneous tumor microenvironment characterized by mixed lytic and sclerotic lesions, complicating effective targeting of the whole tumor and increasing the risk of pathological fracture[14,15]. Despite promising histological outcomes, the biomechanical effects of histotripsy on bone at the tissue and whole-bone levels remain unexplored. Understanding these mechanical responses is critical for developing safe and effective OS treatment protocols that preserve structural integrity in both tumor-affected and surrounding healthy bone.

For effective treatment management, it is essential to assess treatment eligibility and plan prophylactic measures for OS tumor-bearing limbs following treatment. Image-based finite element (FE) analysis provides a noninvasive, cost-effective framework for predicting patient-specific fracture risk and informing surgical planning. FE models derived from computed tomography (CT), quantitative CT, and dual-energy x-ray absorptiometry (DXA) imaging have demonstrated accuracy in predicting fracture location and risk in clinical applications; however, their limited spatial resolution cannot precisely resolve the heterogeneous microarchitecture of OS lesions or successfully differentiate between tumor tissue and surrounding vasculature[16,17]. Consequently, current clinically-derived FE approaches are insufficient for evaluating how treatment-induced microstructural alterations influence mechanical integrity.

1.2 Summary of Research Goals

The primary goal of this research is to quantify how histotripsy-induced microstructural disruption affects the mechanical behavior of OS tumor-bearing and healthy bone via integration of high-resolution μCT imaging, mechanical testing, and FE modeling. The findings of this study will establish critical data on the biomechanical effects of histotripsy, improve predictive modeling accuracy, and facilitate its clinical translation as a noninvasive limb-

salvage strategy for OS.

1.3 Objective and Specific Aims

This goal is addressed through the following specific aims, which combine experimental techniques and computational modeling to link the microstructural changes caused by OS and histotripsy to the mechanical behavior of bone.

Aim 1: Quantify the effects of histotripsy on the mechanical properties of OS tumor-affected and surrounding healthy bone tissue.
Aim 1.1: Qualitatively evaluate structural heterogeneity in OS tumor-affected bone tissue.

Aim 2: Develop a predictive finite element tool to model the effects of histotripsy and OS on whole-bone mechanics.

1.4 Document Structure

This document comprises 7 chapters and an appendix.

Chapter 1 outlines the motivation for research in OS tumor-bearing bone and potential treatment alternatives, as well as the overarching objectives and methods employed to address them.

Chapter 2 presents a literature review covering the biomechanics of OS-affected bone, focused ultrasound methods and their applications in bone, existing FE tools and their potential applicability to OS tumor-bearing bone, and comparative animal models currently used in these studies.

Chapter 3 describes the evaluation of OS heterogeneity and the efficacy and safety of histotripsy in a comparative canine OS tissue model via μCT image analysis and compression

testing. Portions of this work were presented at the Summer Biomechanics, Bioengineering, and Biotransport (SB^3C) annual conference in 2023 and 2024, and the full study was published in *Frontiers in Veterinary Science* in 2026[13].

Chapter 4 characterizes the effects of histotripsy on whole-bone mechanics in a murine OS tibia model via μCT image analysis and compression testing. The manuscript detailing the results of this work is under preparation.

Chapter 5 examines the effects of HIFU on murine OS tumor-bearing bone mechanics using methods similar to those in Chapter 4. While histotripsy ablates tissue via a nonthermal mechanism, this chapter explores how thermal FUS influences bone integrity, providing a comparative perspective across FUS modalities. The manuscript detailing the results of this work is under preparation.

Chapter 6 introduces an FE model capable of predicting fracture risk in histotripsy-ablated OS tumor-bearing and contralateral, healthy limbs in a murine OS model. This model was validated against experimental results, yielding a robust, subject-specific tool capable of predicting regions of high strain for both diagnostic and treatment planning applications. The manuscript detailing the results of this study is under preparation.

Finally, Chapter 7 summarizes the overall conclusions from the studies presented in previous chapters and highlights potential directions for future research.

Chapter 2

Review of Literature

2.1 Osteosarcoma: Disease overview

Pathology and etiology:

Osteosarcoma (OS) is an aggressive primary malignant bone tumor and the most prevalent bone malignancy in children and young adults[1,2]. Approximately 90% of OS cases originate in the metaphyseal region of long bones, particularly at sites of rapid bone growth such as the proximal humerus, distal femur, and proximal tibia. Peak incidence occurs between 10 and 24 years of age, coinciding with pubertal growth spurts[3–5]. Although OS accounts for only 0.2% of all human cancers and has an incidence rate of approximately 1.2/100,000 cases/year, its clinical impact is profound due to its aggressive nature and poor outcomes[2,6,7]. The 5-year survival rate for patients with localized OS is approximately 75%, but decreases dramatically to 30-35% for patients who present with pulmonary metastases, which are found in up to 20% of patients at time of diagnosis[1,6,8].

For most patients, the etiology of OS is unknown[9]. The tendency of OS to develop during pubertal growth spurts at sites of maximum bone turnover suggests a link with rapid bone proliferation. Risk factors include a history of radiation exposure, chemotherapy, or prior benign bone lesions[9]. Mutations in RB1 and TP53, associated with hereditary retinoblastoma and Li-Fraumeni syndrome, respectively, significantly increase susceptibility to OS[10,11]. In older adults, OS often develops secondary to Paget's disease of bone, a chronic bone remodeling disorder that produces structurally weak and tumorous bones[12].

Clinical presentation:

OS patients most commonly present with a dull, progressive pain in the affected limb, localized swelling, or a palpable mass. Pathological fracture is present in 5-10% of cases at time of diagnosis. Up to 80% of patients with OS eventually develop metastatic disease, with pulmonary metastasis being the most common. The nonspecific symptoms, pronounced heterogeneity, and rapid progression of OS often delay or lead to incorrect diagnoses. Common differential diagnoses, including osteomyelitis, Ewing sarcoma, and benign bone lesions, can mimic the clinical and radiographic features of OS, further obscuring definitive diagnosis and potentially leading to misguided treatment[3,13].

OS exhibits significant genetic and transcriptional heterogeneity, both of which contribute to its highly variable phenotype and behavior; the tumor matrix often contains osteoblastic, chondroblastic, and fibroblastic components that coexist within a single lesion[14]. Radiographically, this manifests as mixed lesions with poorly defined margins that contain sclerotic regions of excessive tumor osteoid production and lytic regions of bone resorption. Biologically, OS is characterized by simultaneous osteolysis and deposition of disorganized woven bone, resulting in cortical thinning, increased porosity, and substantial disruption of normal bone architecture[3,15]. These features not only contribute heavily to treatment resistance and metastatic potential, but also contribute to elevated risk of pathological fracture[16–18].

Current therapeutic approaches:

The standard of care for OS has changed little since the early 1980s and typically involves neoadjuvant chemotherapy followed by surgical resection and adjuvant chemotherapy[8,12]. Although this multimodal approach has improved overall survival, prognosis for OS patients remains poor; treatment ineligibility, resistance, local recurrence, implant failure, metastasis effects, and reduced limb function post-treatment limit patient outcomes and quality of life[19–21]. Many patients are ineligible for surgical resection due to tumor location, insufficient margins or involvement of critical structures. Additionally, adjuvant chemotherapy has

reached a therapeutic plateau, as OS often develops chemoresistance that limits long-term efficacy[14].

Limb amputation can have significant long-term consequences, particularly for pediatric patients, and limb-salvage surgery doubles the risk of local recurrence and can increase the likelihood of pathological fracture post-surgery[22]. Radiation therapy may be considered for unresectable, recurrent, or metastatic tumors; however, OS displays inherent radioresistance, requiring high doses and wide treatment margins to encompass microscopic tumor invasion. This increases radiation exposure to surrounding bone and soft tissue, resulting in decreased bone density, toxicity effects, and a higher risk of pathological fracture[23,24]. Martin et al. found that, although 84% of canine OS patients treated with stereotactic body radiation therapy for limb-salvage purposes had maximum lameness improvement for a median of 3 weeks post-treatment, 41% of patients fractured in the affected limb within 3 months[25]. More recently, targeted and immunotherapeutic approaches have been explored to improve outcomes, but the highly immunosuppressive tumor microenvironment of OS has led to limited clinical success thus far[26]. Given the challenges of current therapeutic strategies and the absence of identifiable precursor symptoms in OS, early and accurate detection is critical for improving patient outcomes[14].

2.2 Diagnostic imaging modalities in OS

Diagnostic imaging modalities such as plain radiographs, computed tomography, and magnetic resonance imaging provide essential information about tumor characteristics and impact, effectively guiding diagnosis and treatment planning.

Conventional radiography:

Plain radiographs are the current clinical gold standard for the initial detection and evaluation of suspected OS[27]. Radiographs provide essential information about tumor size, location,

extent of bone destruction, and periosteal reaction patterns that can help distinguish malignant from benign lesions. According to the World Health Organization (WHO), diagnostic features for the classification of bone tumors include aggressive periosteal reactions such as the sunburst pattern or Codman triangle, medullary and cortical bone destruction, and areas of tumor matrix ossification or calcification[22,28]. OS lesions are genetically and morphologically heterogeneous, often presenting as mixed sclerotic and lytic regions with cortical invasion and destruction[12]. Loss of trabecular bone microarchitecture and poorly defined tumor margins are also typically observed[27].

Although these features can support an OS diagnosis, no pathognomonic radiographic findings exist, and definitive diagnosis requires a histopathological analysis via bone biopsy[22]. Despite their diagnostic value, conventional radiographs have limited sensitivity and resolution; they cannot accurately evaluate bone marrow or soft tissue invasion, nor can they quantify the mineralized osteoid formation characteristic of OS[14,29]. Consequently, 3D imaging modalities such as computed tomography and magnetic resonance imaging have become important tools for tumor staging, surgical planning, and treatment monitoring.

Computed tomography (CT):

CT provides high-resolution imaging of bone anatomy and lesion composition, making it ideal for assessing cortical destruction, matrix mineralization, and variations in bone density[27]. CT scans of the chest are routinely performed to detect metastatic pulmonary nodules, which are resected together with the primary tumor[30,31]. CT is also particularly valuable in imaging smaller or more anatomically complex bones such as the mandible, pelvis, or vertebrae, and is often used to guide lesion biopsy for diagnostic confirmation[27,32]. However, while CT excels at delineating calcified or mineralized structures, it is less effective at defining tumor boundaries and assessing soft tissue or neurovascular involvement. The radiation exposure associated with repeated CT imaging also limits its longitudinal use in pediatric OS patients, highlighting the shift toward MRI-based assessment[33].

Magnetic resonance imaging (MRI):

MRI is the current gold standard for OS tumor staging and presurgical planning due to its superior soft tissue contrast and ability to accurately define intramedullary and adjacent joint, soft tissue, and neurovascular involvement[27,29]. It is also used to monitor treatment and to ensure sufficient surgical margins, typically 2-3cm from the tumor[31].

Conventional MRI sequences, however, have low signal intensity in cortical bone due to its short T2 relaxation time, making it challenging to visualize periosteal reactions, cortical disruption, and other traditional radiographic features of OS. To address these limitations, advanced sequences such as ultrashort echo time (UTE) and zero echo time (ZTE) have been developed. These sequences differentiate bound water, or water bound to the collagen-mineral matrix, from pore water, or water in the pore space of cortical bone, to noninvasively assess bone quality, porosity, and mechanical competence. Studies have shown that UTE MRI-derived bound and pore water concentrations can predict fracture risk and correlate with structural and material properties as measured by mechanical testing[34,35]. Structural parameters, including trabecular thickness, cortical porosity, and bone volume fraction, are essential image-derived parameters that inform fracture risk and treatment eligibility metrics. These quantitative metrics, when paired with mechanical testing, provide critical insight into the relationship between bone structure and function in both healthy and diseased bone states.

2.3 Quantitative assessments of bone structure and mechanics

Quantitative measures of bone structure and mechanics are essential for assessing bone health. Bone is a dynamic, load-bearing tissue that continuously adapts to mechanical stress through bone remodeling, a highly regulated process in which osteoblastic bone formation

and osteoclastic resorption are balanced to preserve mechanical competence under physiological loading conditions. This adaptive process gives rise to a heterogeneous, anisotropic, and porous material, enabling bone to achieve an optimal balance between stiffness, strength, and energy absorption[36,37]. Pathological disruption of bone remodeling, such as that induced by OS, alters both tissue composition and architecture, necessitating quantitative mechanical assessment to characterize changes in load-bearing capacity.

The skeleton is composed primarily of two tissue types: trabecular (cancellous) bone and cortical (compact) bone, each contributing distinctly to overall mechanical performance. Trabecular bone constitutes roughly 20% of the total bone mass, has high porosity (50-95%), and is typically found at the ends of long bones. It acts as a shock absorber by transferring mechanical loads from the articular surface to the denser cortical shell[38]. OS typically arises in the metaphyseal growth regions of long bones, sites of high trabecular density. Tumor-mediated upregulation of osteoclast activity leads to erosion of native trabeculae, increased bone resorption, and loss of trabecular architecture, ultimately resulting in compromised mechanical integrity[38,39].

The significantly denser cortical shell surrounds the trabecular bone, makes up the other 80% of total bone mass, and provides the primary structural support, mechanical strength, and protection for bone marrow and internal organs[38,39]. OS frequently invades and erodes the cortical shell, resulting in cortical thinning, increased porosity, and a disordered woven bone structure caused by accelerated, dysregulated bone turnover. These features contribute significantly to bone fragility and pathological fracture[39]. Clinically, pathological fracture in OS is associated with poor prognosis, involving complications such as fracture hematoma, spread of micro-metatases, and potentially reduced limb function[40,41]; Kelley et al. found that adult OS patients with a pathological fracture had significantly lower overall survival[15].

To assess bone structure and mechanical integrity, several quantitative material and mechanical parameters can be evaluated, including ultimate stress (σ) and strain (ε), elastic

modulus (E), stiffness (k), energy to failure, and toughness. Together, these metrics capture both tissue-level material behavior (i.e., elastic modulus and toughness) and whole-bone structural response (e.g., stiffness and energy to failure) to describe the load-bearing capacity of bone and its resistance to fracture under physiological loading conditions. Since OS alters both tissue composition and structural integrity, changes in these parameters reflect not only material degradation but also disruption of normal load transfer mechanisms, requiring distinct experimental methods for comprehensive analysis. Relevant mechanical properties and their physiological interpretations are listed in Table 2.1 below.

Table 2.1: Mechanical properties used to assess bone structure and integrity.

Mechanical metric	**Definition**	**Physical interpretation**
Elastic modulus (E)	Slope of the linear elastic region of the stress strain curve	Measure of stiffness; higher E indicates a stiffer material that deforms less under load
Stiffness (k)	Slope of the linear elastic region of the load-displacement curve	Reflects whole-bone resistance to deformation under applied loading
Ultimate stress (σ_{ult})	Maximum stress sustained before failure	Measure of strength; higher σ_{ult} indicates greater load-bearing capacity
Ultimate strain (ε_{ult})	Strain at failure	Measure of ductility; higher values indicate the material can withstand higher levels of deformation before fracture
Energy to failure	Area under the stress-strain curve up to failure	Reflects capacity to absorb energy before fracture
Toughness	Energy absorbed per unit volume before failure	Resistance to crack initiation and propagation

Experimental methods for structural assessment:

Mechanical testing is the primary experimental approach used to quantify bone structural integrity and material properties under load. Common methods include compression, tension, three- and four-point bending, torsion, and indentation-based techniques[42]. Loading mode should be selected based on the physiologically and clinically relevant *in vivo* load-bearing behavior of the bone of interest. Whole-bone mechanical tests in preclinical models, particularly murine long bones, are widely used to investigate bone mechanobiology, and how disease and treatment affect bone mechanics[42,43]. These tests are most often performed in bending and torsion to approximate *in vivo* loading conditions, whereas compression and tension tests allow for isolation of specific mechanical responses, such as axial stiffness or ultimate load.

At the tissue level, nanoindentation and atomic force microscopy provide complementary measurements of local material properties, including elastic modulus and hardness, which capture changes in mineralization and collagen organization. Many studies have applied

these approaches to characterize OS at the cellular or tumor-tissue scale using *in vitro* and *in silico* models to reveal how OS cells respond to biochemical and mechanical stimuli[44–47]. While informative, these models provide limited insight into how tumor-driven disruption affects whole-bone integrity. Experimental methods that assess bone under physiological loading are therefore required to determine clinically relevant mechanical competence of OS tumor-bearing bone.

The structural effects of OS on bone have not yet been quantified in humans; however, preclinical and translational models suggest tumor-induced alterations to bone stiffness, elastic modulus, and energy absorption via compression and bending tests[48–50]. Steffey et al. found that canine OS-affected antebrachia absorbed less energy to yield, were more compliant, and had a decreased ultimate load relative to controls[48]. Mechanical testing alone, however, provides only global measures of whole-bone behavior and cannot resolve how localized structural distruption, such as that caused by tumor invasion or treatment-induced remodeling, affects the spatial distribution of strain across the bone surface.

Integration of imaging and mechanical techniques to evaluate mechanical behavior:

Integrating mechanical testing with three-dimensional digital image correlation (DIC) allows for non-contact, full-field measurement of surface deformation, providing insights into local strain distributions that are inaccessible with traditional load-displacement analysis[51]. This integration is particularly valuable for bones affected by disease, such as OS, or during healing, where localized remodeling, disease-driven structural disruption, and implant presence may produce highly nonuniform strain fields[52,53].

To track displacement during loading using DIC, a randomized speckle pattern is applied to the specimen surface and two synchronized high-speed cameras in a stereo configuration track speckle displacements during loading to generate full-field surface strain maps[54,55]. By capturing both in-plane and out-of-plane displacements, DIC accurately measures strains even in curved, irregularly shaped bones or in specimens with heterogeneous material prop-

erties[56]. While strain gauges are frequently used to measure bone strain, they provide only localized measurements and may overestimate strain due to stress concentrations introduced by adhesive bonding[51,57]. Several studies have successfully combined DIC with mechanical testing in murine long bones to characterize whole-bone deformation and failure behavior[58–60]. Full-field strain data obtained from DIC are also used to validate image-based FE models, strengthening computational predictions of stress and strain distributions across the surface of the tissue[60,61].

Since whole-bone mechanical behavior is strongly influenced by bone geometry, image-based morphometric analyses provide essential context for interpreting mechanical outcomes[62,63]. μCT imaging complements mechanical testing by enabling high resolution, 3D visualization of cortical and trabecular architecture[64–66]. Although commonly used in clinical settings, X-ray-based bone mineral denstiy (BMD) measurements obtained from DXA or quantitative CT predict fracture risk with only 30-50% accuracy due to their inability to resolve microarchitectural parameters such as cortical porosity or trabecular bone volume fraction[67].

In contrast, μCT is considered the gold standard for preclinical bone morphology assessment due to its ability to quantify structural parameters directly linked to mechanical behavior, including anisotropy, mineral density distributions, trabecular connectivity, and cortical porosity[64,68]. When integrated with mechanical testing, μCT-derived morphometrics enable the attribution of changes in stiffness, strength, and failure behavior to such structural characteristics. Prior studies in osteoporotic, osteopenic, post-menopausal, and metastatic disease models consistently demonstrate that increased cortical porosity, reduced mineralization, and decreased trabecular bone volume fraction elevate fracture risk[67,69–71]. However, these structure-function relationships have not yet been characterized in primary OS, particularly in tumor-bearing bone exhibiting heterogeneous lesions and treatment-induced changes. Quantifying this morphological heterogeneity using μCT and linking it to experimentally measured whole-bone mechanics represents a critical next step toward improving fracture risk assessment and informing treatment planning in OS-affected limbs.

While μCT provides detailed insight into bone microarchitecture, its high radiation dose and long acquisition times limit its use to *ex vivo* and preclinical applications[65]. In human bone, trabecular thickness typically ranges from 50-200μm and cortical pore diameters from 30-100μm, whereas conventional clinical CT systems operate at resolutions of 100-400μm, insufficient to resolve these features[65,72]. High-resolution peripheral quantitative computed tomography (HR-pQCT) has emerged as a clinically translatable, low-dose imaging modality capable of resolving cortical and trabecular microarchitecture at a scale approaching that of μCT, enabling improved clinical assessment of bone quality beyond density-based measures alone[73]. Unlike DXA, which provides only areal BMD measurements without structural information, HR-pQCT can quanitfy parameters such as trabecular bone volume fraction (Tb.BV/TV), cortical porosity (Ct.Po), and cortical thickness (Ct.Th), all of which are strongly correlated with mechanical properties[74,75]. When combined with finite element modeling, HR-pQCT-derived measures can be used to estimate whole-bone strength, stiffness, and failure load, providing a more comprehensive and clinically relevant assessment of mechanical competence than BMD alone[76,77]. Several studies have demonstrated that image-based FE models improve prediction of fracture risk compared to density-based metrics, highlighting the importance of incorporating bone microarchitecture and spatial heterogeneity into clinical assessment[78,79].

Despite these advances, however, HR-pQCT is currently limited to peripheral skeletal sites such as the distal radius and tibia, and may not capture lesions located in proximal long bones or axial locations commonly affected in OS, especially considering the substantial structural heterogeneity induced by the tumor. Additionally, while its resolution exceeds that of clinical CT, it remains lower than CT, potentially limiting sensitivity to fine-scale structural changes. Even with these drawbacks, integrating HR-pQCT-derived morphometrics with finite element modeling provides a clinically feasible pathway to translate the structure–function relationships established in this work into patient-specific fracture risk prediction and treatment planning.

Impacts of current therapies on bone structure and mechanics

Osteosarcoma disrupts bone homeostasis through irregular osteoblast and osteoclast activity, resulting in the simultaneous deposition of abnormal, immature mineralized matrix and resorption of existing mature bone. Tumor-mediated upregulation of RANK/RANKL/OPG signaling enhances osteoclast differentiation and activity, shifting bone remodeling toward net resorption and driving cortical thinning, loss of trabecular architecture, and reduced BMD. These structural alterations reduce stiffness, strength, and energy absorption capacity, ultimately compromising the mechanical competence of bone and increasing pathological fracture risk.

Current therapeutic strategies for OS may further alter bone structure and mechanical behavior. Neoadjuvant chemotherapy preceding limb-salvage surgery or amputation typically consists of high-dose methotrexate, doxorubicin, and cisplatin (MAP), with ifosfamide incorporated in some protocols for poor responders[80,81]. These agents can impair bone remodeling and mineralization through multiple pathways. Methotrexate suppresses bone formation while increasing bone resorption, resulting in overall bone loss and a heightened risk of fracture. Although highly effective at targeting distant pulmonary metastases, it has been clinically associated with an increased rate of stress fractures and severe osteopenia in younger patients[82]. Experimental studies have demonstrated that methotrexate induces a pro-osteoclastogenic environment within bone, increasing osteoclast density and ultimately leading to trabecular thinning and reduced bone mass[83]. Cisplatin and ifosfamide are nephrotoxic agents that contribute to endocrine dysfunction and defective bone mineralization; ifosfamide in particular is associated with Fanconi syndrome, a renal tubular dysfunction that can cause rickets, or softening and weakening of bone, in pediatric patients[84]. Clinical imaging studies in pediatric OS patients treated with MAP have reported decreased lumbar spine BMD as measured by DXA[85].

While DXA provides clinically accessible measures of bone mineral density, it cannot resolve

changes in cortical architecture, porosity, or trabecular network integrity that are more directly predictive of mechanical competence and fracture resistance[86]. Relatively few studies have directly assessed the mechanical consequences of chemotherapy on bone strength. Pelker et al. assessed the effects of methotrexate and doxorubicin on intact and healing rabbit femora over a 16 week observation window via rapid torsional testing to failure, reporting significant impairment of fracture callus strength but no change in intact cortical bone torsional properties[87]. Van Leeuwen et al. demonstrated that treatment with MAP resulted in decreased bending resistance in the tibia and femur and reduced shear strength of the proximal tibial growth plate in an intact rat model[88,89]. Notably, these studies employed growth plate shear testing in a rat model, which differs from the uniaxial compression, bending, and torsional mechanical testing methods more commonly used to assess cortical and trabecular mechanics in murine long bone. The findings of such studies indicate that chemotherapy can directly impair bone mechanical properties independent of changes in BMD; however, variability in animal models, anatomical sites, and mechanical testing protocols limits direct comparison across studies and hinders a comprehensive understanding of how cytotoxic therapies influence bone mechanics. Further, the effects of cytotoxic therapy on cortical or trabecular bone mechanics in murine models using integrated whole-bone mechanical testing and μCT-based morphometric analysis have not yet been characterized. Nonetheless, these findings have significant implications for fracture risk in pediatric OS patients, whose skeletons are actively growing and already structurally compromised by tumor invasion.

Radiation therapy is another limb-sparing treatment modality that can also alter the mechanical competence of bone. Although not commonly used as a primary treatment for OS due to its inherent radioresistance, radiation may be applied for local tumor control or pain palliation in patients with unresectable tumors or recurrent disease. Ionizing radiation induces dose-dependent cellular-level changes in bone, including osteoblast and osteocyte death, suppression of bone repair capacity, and collagen crosslink degradation. These changes manifest as increased cortical porosity, reduced mineral apposition rate, and altered

collagen organization, all of which compromise fracture resistance at both the tissue and whole-bone levels[90]. Preclinical studies using murine models have demonstrated significant reductions in bone stiffness, ultimate load, and fracture toughness of whole bone following therapeutic radiation doses[91–93], with changes in structural and material properties as measured by μCT accounting for over 50% of reductions in bone strength[93]. These studies employed different rodent models and mechanical testing methods– Wernle implemented axial compression to determine the peak load of irradiated Balb/c mouse femurs[91], Bartlow used three-point bending to characterize fracture toughness in Balb/cJ mouse femurs[92], and Emerzian determined strength and stiffness of irradiated lumbar spine segments in a Sprague-Dawley rat model[94]. Similarly to studies evaluating chemotherapy effects, differences in species, anatomical location, and loading modality limit direct comparison across studies and hinder clinically relevant fracture risk assessment. Further, most preclinical studies evaluate radiation effects in grossly healthy bone, which may underestimate mechanical consequences in tumor-affected bone already compromised by OS invasion. Clinically, however, the structural impact of radiation-induced bone degradation is apparent, reflected in canine OS patients treated with stereotactic body radiotherapy (SBRT) as a limb salvage approach, where Martin and Altwal reported a pathological fracture rate of approximately 40% within 3-5 months of treatment[25,95].

Long-term antiresorptive treatments such as bisphosphonates and denosumab are being investigated as potential adjunct therapies for OS due to their capacity to reduce osteoclast-mediated bone resorption, which is upregulated by both the tumor and cytotoxic treatments. Bisphosphonates bind to hydroxyapatite at sites of active bone turnover to induce osteoclast apoptosis, reducing resorption and decreasing fracture risk[96], and have shown some promise in preclinical OS models in combination with radiation[97,98]. Denosumab, a monoclonal antibody that targets RANKL and thereby suppresses osteoclast differentiation and activity, is similarly employed to preserve bone mass in osteopenic and osteoporotic populations. However, their clinical application requires careful consideration; denosumab and

high-dose bisphosphonate use have been associated with atypical fractures and osteonecrosis of the jaw, rare but severe complications likely stemming from the long-term suppression of bone remodeling[99]. While both agents have demonstrated efficacy in maintaining BMD, their impacts on the structural and mechanical properties of tumor-bearing bone have not yet been directly quantified, highlighting the need for experimental approaches that directly link morphological changes to mechanical outcomes.

Across chemotherapy, radiation, and antiresorptive treatments, a common limitation in the literature is the lack of integrated structure–function analyses that directly relate therapy-induced morphological changes to the mechanical behavior of bone. Further, no studies to date have characterized the mechanical consequences of standard OS therapies in tumor-bearing bone, where pre-existing tumor-induced structural degradation may significantly alter the mechanical response to treatment. This represents a critical gap, as fracture risk in OS patients depends on the combined effects of tumor progression and therapeutic intervention. Addressing these limitations requires experimental approaches that directly link bone structure to mechanics under physiologically relevant loading conditions, enabling more accurate fracture risk assessment and the establishment of safe, patient-specific treatment thresholds.

Image-based computational modeling for noninvasive characterization of structural properties:

While mechanical testing provides direct measurements of bone strength and structural integrity, it is inherently destructive and requires tissue extraction, limiting its clinical applicability. Image-based FE modeling addresses this limitation by using advanced imaging modalities such as CT, MRI, or DXA to generate subject-specific 3D models of bone and noninvasively estimate mechanical behavior. These computational approaches enable prediction of stiffness, load distribution, and fracture risk through established density-modulus relationships and robust material mapping[100,101]. As a result, FE models have been extensively applied to evaluate fracture risk, bone healing, osteoporosis, aging-related deterioration, and

therapeutic effects in both human clinical studies and preclinical comparative animal models[101–104].

Bone exhibits strong anisotropy, with tensile and compressive strengths significantly higher along the longitudinal axis than along in the radial and circumferential directions[105]. Accordingly, healthy cortical bone is frequently modeled as transversely isotropic in computational models due to the comparatively small differences in material properties between the radial and circumferential axes[106]. Density-modulus relationships derived from quantitative CT measurements are commonly used to assign element-wise material properties within FE meshes[76,77,107]. These relationships describe the strong empirical correlation between image-derived mineral density (e.g., BMD or Houndsfield units (HU)) and elastic modulus. For cortical bone, these relationships are often approximated as linear, while trabecular bone typically follows a nonlinear power-law relationship due to its porous architecture and load-dependent structure[108]. Although the general forms of the density-modulus laws are consistent across CT modalities, the high spatial resolution of μCT allows capture of morphometric parameters not resolved by clinical CT, such as cortical porosity and trabecular architecture. As a result, μCT-based FE models are typically more representative of mechanical response, and numerous studies have validated the use of μCT-derived mechanical parameters across species and loading modes[60,107,109].

Despite these advances, image-based FE models for bone with primary OS lesions remain extremely limited. Goyal et al. developed a CT-based FE model of a human OS tumor-bearing femur, but the use of homogeneous material properties limited its ability to capture the heterogeneous structure of tumor-bearing bone and results were not validated against experimental mechanical testing data[110]. More recently, a CT-based canine radius FE model simulated OS tumor lysis with an osteotomy; however, this approach does not account for the mixed osteolytic and osteoblastic features typical of OS and therefore cannot accurately reproduce whole-bone mechanical behavior under physiological loading[111]. As a result, existing FE frameworks are insufficient for predicting how localized tumor progression or ther-

apeutic interventions affect bone morphology and structural integrity. Addressing these limitations with experimentally validated, high-resolution FE models capable of evaluating tumor-induced heterogeneity and treatment-related structural changes is critical for optimizing limb-salvage strategies.

Clinical translation: fracture assessment and patient stratification:

Clinically, fracture risk is most commonly assessed using tools such as FRAX and trabecular bone score (TBS), which provide population-based estimates of 10-year fracture risk in men over 50 and postmenopausal women, populations particularly susceptible to reduced bone density and pathological fracture. FRAX integrates clinical risk factors such as age, comorbidities, steroid use, and family history with optional DXA-derived BMD to estimate fracture risk. While commonly used in clinical applications, it relies on simplified, largely binary inputs and does not account for dose-dependent treatment effects, cumulative exposure to risk factors, or the severity and location of previous bone damage. Importantly, FRAX was originally developed using data from generally healthy, untreated populations and does not capture disease-specific structural changes. Although recent studies demonstrate preliminary predictive capability for fracture incidence in oncologic populations, FRAX remains nonspecific and does not incorporate tumor-induced heterogeneity or the complex effects of cytotoxic or antiresorptive therapies on bone**Ye et al 2024**. The addition of DXA-derived BMD improves fracture prediction, with density accounting for approximately 60-70% of bone strength[86,112]; however, even this combined metric does not capture the microarchitectural features or local, tumor-induced structural defects that are critical determinants of mechanical integrity in OS tumor-bearing bone.

TBS provides an indirect measure of trabecular microarchitecture by evaluating pixel gray-level variations in lumbar spine DXA images and has been shown to improve fracture risk prediction when used in conjunction with FRAX in osteoporotic populations[113]. However, similar to FRAX, TBS is limited in its applicability to OS due to its inability to resolve spatial

heterogeneity and its sensitivity to treatment-related changes. Antiresorptive and cytotoxic therapies may alter TBS values independent of mechanical competence, confounding interpretation. These tools highlight a key limitation of current clinical fracture risk assessment; namely, reliance on population-based and density-derived metrics without accompanying information about patient-specific bone geometry, microarchitecture, or mechanical behavior limits accurate assessment of bone quality and fracture risk, which is especially critical in structurally weakened OS-affected bone.

To address these limitations, a reduced parameter set for clinical translation that directly reflects the structural and mechanical determinants of fracture risk in OS tumor-bearing bone is proposed. Specifically, the most clinically relevant parameters are as follows: (1) trabecular bone volume fraction (Tb.BV/TV), (2) cortical porosity (Ct.Po), and (3) FE-derived estimates of whole-bone stiffness, strength, and post-yield behavior (i.e., toughness). Each of these parameters captures a distinct but complementary aspect of bone mechanical competence (Table 2.2). Tb.BV/TV reflects the ability of trabecular bone to distribute load, with reductions indicating compromised structural support and decreased whole-bone strength[74]. Ct.Po reflects degradation of the primary load-bearing cortical shell, where increased porosity is strongly associated with reduced strength and increased fracture susceptibility[75]. FE-derived whole-bone stiffness and strength provide patient-specific estimates of load-bearing capacity, while post-yield metrics such as toughness capture the resistance of bone to fracture and its energy absorption capability. Experimental studies have demonstrated that reductions in bone toughness can lead to brittle failure even when initial stiffness appears preserved[114], a feature particularly critical for diseased bone. Future work should establish quantitative thresholds for these parameters to define treatment eligibility and fracture risk in clinical populations. Each of these properties can be quantified from clinical imaging modalities such as HR-pQCT or clinical CT, with FE-derived mechanical properties computed using study-specific density-modulus relationships[73,115]. This enables fully image-based, noninvasive, patient-specific assessment of bone structure and mechanical integrity,

which is critical for accurately evaluating eligibility for emerging limb-sparing therapies. In OS tumor-bearing bone, clinically validated thresholds for treatment eligibility are currently undefined. However, existing evidence suggests that patients with preserved trabecular structure, low cortical porosity, and high predicted failure load and toughness are likely to tolerate treatment without elevated fracture risk. In contrast, patients with severely compromised mechanical properties may require prophylactic stabilization or alternative treatment strategies.

Table 2.2: Clinical interpretation of image- and computationally-derived structural and material properties

Parameter	Derivation	Clinical interpretation
Trabecular bone volume fraction (Tb.BV/TV)	μCT/HR-pQCT	Bone volume and load distribution capacity
Cortical porosity (Ct.Po)	μCT/HR-pQCT	Indicator of microstructural weakness and fracture susceptibility
Strength	FE/Mech testing	Estimated load to failure (fracture risk)
Stiffness	FE/Mech testing	Functional load-bearing capacity
Toughness	FE/Mech testing	Resistance to fracture

2.4 Focused ultrasound as a noninvasive, limb-sparing therapeutic

Focused ultrasound techniques such as high-intensity focused ultrasound and histotripsy have recently emerged as promising noninvasive approaches for treating both malignant and benign soft tissue disease. Treatments are typically performed under the guidance of ultrasound or MRI, allowing clinicians to visualize the treatment zone, monitor energy delivery, and adjust targeting throughout the procedure. Focused ultrasound offers the advantage of noninvasive therapy, no ionizing radiation exposure, reduced recovery time, and avoidance of common complications associated with surgical intervention, including infection and reduced limb function[116]. Although current clinical applications are largely confined to

soft tissue applications, both modalities are increasingly being explored for treating hard tissue malignancies, including OS.

High-Intensity focused ultrasound (HIFU):

High-intensity focused ultrasound is a thermal ablation technique that concentrates ultrasound energy at a focal point, rapidly heating tissue to high temperatures (60-85°C) to induce coagulative necrosis and subsequent tissue remodeling[117]. Clinically, HIFU is most widely applied for breast[118], prostate[119], pancreatic[120], and liver[121] cancers, as well as for treatment of uterine fibroids[122]. In oncological applications, HIFU is used primarily for pain palliation rather than curative treatment; by thermally ablating nerve fibers within the tumor, it provides substantial pain relief with minimal adverse side effects, particularly in late-stage cancers or or those with limited life expectancy[120,123].

Applications of HIFU in bone are largely limited to the palliative treatment of soft-tissue metastases, where the main therapeutic goal is pain relief and improved quality of life[117]. For primary osteosarcoma, the objective would be complete tumor eradication without compromising healthy tissue. However, OS arises within cortical bone, which absorbs approximately 50 times more ultrasound energy than soft tissue, limiting penetration depth and risking unpredictable heating patterns in surrounding healthy tissue. Real-time monitoring of cortical bone temperature or echogenicity is currently unavailable, so treatment instead relies on indirect measurements in the surrounding soft tissue.[117] Despite these challenges, previous studies investigating HIFU for treatment of primary OS tumors have shown effective reduction in pain, significant tumor response, and overall increases in survival and quality of life without severe adverse side effects[124,125]. HIFU has also been shown to stimulate bone remodeling, likely through localized thermal activation of osteoblasts; however, excessive exposure can compromise cortical bone integrity[126,127]. These limitations of thermal focused ultrasound in primary bone tumors have motivated the investigation of nonthermal approaches, such as histotripsy, which disrupt tumor tissue without heat, offering a potentially safer and

more precise treatment option for high-density tissues such as bone.

Histotripsy:

Histotripsy is a noninvasive, nonthermal ablation technique that uses focused ultrasound to mechanically destroy tissue. Unlike HIFU, histotripsy utilizes controlled inertial cavitation to disintegrate or liquefy tissue, rather than heat. This avoids complications associated with heat dissipation and vascular perfusion, which can lead to off-target tissue damage in thermal ablation[116,128–130]. Real-time treatment monitoring is possible using ultrasound or MRI, as cavitation bubble clouds and lesion formation can be directly visualized. This feedback is essential for identifying off-target cavitation and adjusting treatment parameters, which are crucial to ensure precise, patient-specific ablation[128,131,132].

Preclinical studies in a variety of cancer types, including liver[133], prostate[134], renal[135], breast[136], and pancreatic[137] tumors, have demonstrated that histotripsy can effectively liquefy tumor tissue while sparing surrounding structures. Canine OS *ex vivo* studies have similarly shown that histotripsy ablates primary OS tumor tissue while preserving extracellular matrix, neurovascular structures, and other non-target tissue within the ablation zone[49,131,138,139]. However, OS often infiltrates and degrades cortical bone via osteolysis and deposition of mechanically inferior woven bone matrix[3]. These changes significantly compromise bone stiffness and strength, increasing pathological fracture risk. The prognosis for OS patients with pathological fractures is poor, involving complications such as fracture hematoma and metastatic spread[40]. Consequently, characterizing how histotripsy influences the structural and mechanical integrity of OS-affected bone is critical for determining its viability as a noninvasive, bone-sparing therapeutic approach.

2.5 Comparative animal models

Due to the rarity of OS in the human population and the limited availability of human tissue in biomechanics studies, animal models serve as valuable tools to study disease pathology and progression, genetic mapping, and therapeutic response. Since the etiology and pathology of OS are not yet fully understood, no single model can fully replicate the complexity and heterogeneity of human disease. However, murine and canine models are able to capture distinct key aspects of OS biology, each providing its own advantages regarding genetic manipulability, reproducibility, and translational relevance.

Translational canine model:

Canine OS arises spontaneously in pet dogs and closely parallels human OS at the histological, molecular, and clinical levels, making it a valuable and robust comparative oncology model[140,141]. The disease exhibits similar patterns of presentation, genetic complexity, metastatic progression, and treatment response in both species. Many of the genes involved in human OS development, such as P53, RB, and PTEN, are also indicated in canine OS; transcriptional and histopathological analyses demonstrate that canine and human OS are indistinguishable at the tissue level, reinforcing the relevance of this naturally occurring model[140,142,143]. The high incidence of OS in large and giant breed dogs provides a consistent and accessible clinical population, and the shortened canine lifespan, intact immune system, and shared human environment enable accelerated evaluation of disease progression and therapeutic response, benefiting both veterinary and human medicine[144,145].

Histotripsy has recently been evaluated in canine OS as a potential noninvasive, limb-sparing treatment for OS. It has shown feasibility and efficacy in excised canine OS tumors, leaving no intact tumor cells within the ablation zone and preserving mechanical competence at the tissue level[49,138]. Subsequent work in a canine clinical population has demonstrated histotripsy's ability to safely ablate canine OS tumors *in vivo* at clinically relevant doses,

with gross and histological conformation of tumor destruction and no significant clinical adverse effects[139].

From a biomechanical perspective, canine long bones are well suited for translational study; their size, cross-sectional geometry, and loading environment closely approximate those of human long bones, and cortical material properties overlap significantly. Effective elastic modulus values for canine femoral cortical bone, measured via three-point bending, typically range from 13-17GPa, aligning well with human cortical bone values of approximately 10-20 GPa[146,147]. Additionally, comparative studies of canine trabecular bone demonstrate qualitative similarities in the strength and direction of relationships between mechanical properties such as elastic modulus and ultimate stress, and in the anisotropic response to loading[148,149].

Despite its strengths, there are several key limitations to the canine OS model. Breed-specific predispositions, genetic variability, and differences in body size introduce heterogeneity that can complicate interpretation of biological and biomechanical outcomes[140,150]. Furthermore, canine OS peaks in geriatric populations, whereas human OS primarily occurs in children and adolescents, creating differences in bone physiology, remodeling rates, and mutation burden[143]. Since canine companions constitute a naturally occurring clinical population, tumor characteristics and demographics, including breed, sex, and age, make it challenging to perform standardized experimental studies.

Preclinical murine model:

In contrast to canine models, murine systems provide a more controlled, low-cost, easily accessible platform for investigating tumor-bone interactions and evaluating therapeutic interventions. Several types of murine OS models have been developed, including xenogeneic[151,152], syngeneic[153,154], and genetically engineered mouse models (GEMMs)[155,156].

Xenogeneic models, in which human OS cells are implanted into immunocompromised mice, have been widely used for therapeutic screening, identification of genetic drivers, and analysis

of metastatic potential. Both subcutaneous and orthotopic xenografts provide reproducible and high incidence tumor growth, but the requirement for immunodeficient hosts limit their ability to model tumor-immune interactions, which are critical for understanding tumor or treatment-induced bone remodeling, tumor progression, and responses to immunomodulating therapies[140,151,153].

GEMMs reproduce aspects of human OS by manipulating key oncogenes or tumor suppressor genes such as p53, Rb, and c-Myc. GEMMs closely model human gene-transcription signatures and cytogenetic complexity; however, tumor onset if often variable, and mice may develop other malignancies (e.g., lymphomas) or require sacrifice before full OS development[155,157]. Furthermore, tumors in GEMMs may not arise in anatomically relevant sites, limiting translational applicability for bone mechanics studies[157].

Syngeneic models, which implant murine OS cells into immunocompetent mice, preserve the native immune system and more accurately reflect spontaneous tumor progression, metastasis, and tumor-immune and tumor-therapy interactions. Histotripsy studies using both ectopic[158] and orthotopic[154] murine OS models have demonstrated robust anti-tumor immune responses, including 40-50% reductions in tumor volume, highlighting the importance of intact host immunity for treatment evaluation[158,159].

Murine long bones are frequently used for whole-bone mechanical testing, mostly in bending, but also include compression and torsion, allowing for measurement of stiffness, yield, and failure properties[43,58,160]. 3- and 4-point bending tests are generally straightforward and apply loads to the center of the bone length, but function most accurately with geometrically simple and homogeneous bones, such as the femur. Torsion tests are commonly used in fracture healing studies, as they avoid applying loads directly to the center of the bone and are independent of the bone's cross-section[161]. While these methods provide valuable mechanical insight into the mechanical behavior of bone under stress, only uniaxial compressive loading recapitulates the *in vivo* loading environment of the tibia during nor-

mal weight-bearing. Although magnitudes of mechanical properties are lower than those in larger species due to scaling and geometric differences, murine models provide significant control over tumor induction, treatment application, and mechanical testing protocols. These features enable reproducible analysis of tumor or treatment-induced changes in the bone, particularly microstructural changes and how they influence whole-bone mechanical competence. Such models can be integrated with FE modeling to predict local strain distributions; several studies have validated experimental murine tibia models in compression and bending with FE models with 0-10% errors for cortical parameters and 10-30% for trabecular parameters[43,160,162]. Several studies investigate the effects of aging and bone maladies such as osteoporosis on whole-bone mechanical properties, but, to date, there are no studies investigating the biomechanical effects of OS on whole-bone structural properties.

Large animal models:

Although murine and canine models are the most established in OS research, large animal models such as pigs, sheep, and cows are emerging in the literature[163]. While canine models approximate human bone mechanics reasonably well, large animal bones allow the opportunity to explore disease and therapeutic effects under physiologically larger-scale loading conditions. Mechanical testing of bovine and ovine long bones yield elastic modulus and ultimate strength values comparable to those measured in human bone, supporting their relevance in translational biomechanical applications FE model validation.

Despite these advantages, large animal models are associated with higher cost, lower incidence rates, longer experimental timelines, and greater ethical considerations[163]. While preclinical porcine and ovine models have been applied in histotripsy studies for soft tissue cancer[164] and fetal tissue ablation[165], no studies to date have investigated histotripsy or osteosarcoma in the bones of large animals. Most translational studies in these species focus on surgically induced defects for bone regeneration rather than primary bone tumors[166,167].

Works Cited

(1) Huang, X.; Zhao, J.; Bai, J.; Shen, H.; Zhang, B.; Deng, L.; Sun, C.; Liu, Y.; Zhang, J.; Zheng, J. *J. Bone Oncol.* **2019**, *16*, 100230.

(2) Lindsey, B. A.; Markel, J. E.; Kleinerman, E. S. *Rheumatol Ther* **2017**, *4*, 25–43.

(3) Greenwood, A. C.; Arora, R. D.; Shaikh, H. In *StatPearls*; StatPearls Publishing: Treasure Island (FL), 2025.

(4) Nie, Z.; Peng, H. *Oncol. Lett.* **2018**, *16*, 6502–6514.

(5) Sugalski, A. J.; Jiwani, A.; Ketchum, N. S.; Cornell, J.; Williams, R.; Heim-Hall, J.; Hung, J. Y.; Langevin, A.-M. *J. Pediatr. Hematol. Oncol.* **2014**, *36*, e353–8.

(6) Luu, A. K.; Viloria-Petit, A. M. *Int. J. Mol. Sci.* **2020**, *21*.

(7) Luu, A. K.; Wood, G. A.; Viloria-Petit, A. M. *Front Vet Sci* **2021**, *8*, 734965.

(8) Xu, M.; Wang, Z.; Yu, X.-C.; Lin, J.-H.; Hu, Y.-C. *Orthop. Surg.* **2020**, *12*, 1021–1029.

(9) Ritter, J.; Bielack, S. S. *Ann. Oncol.* **2010**, *21 Suppl 7*, vii320–5.

(10) Le, T. T.; Ha, T. S.; To, L. M.; Dang, Q. M.; Bui, H. T. P.; Tran, T. D.; Vu, P. T.; Giang, H. B.; Tran, D. T.; Nguyen, X.-H. *Front. Oncol.* **2024**, *14*, 1458232.

(11) Agarwal, G.; Kochar, H. S.; Julka, P. K.; Bahadur, S. *Indian J. Otolaryngol. Head Neck Surg.* **2011**, *63*, 115–117.

(12) Rathore, R.; Van Tine, B. A. *J. Clin. Med.* **2021**, *10*, 1182.

(13) Hecker-Nolting, S.; Baumhoer, D.; Blattmann, C.; Kager, L.; Kühne, T.; Kevric, M.; Lang, S.; Mettmann, V.; Sorg, B.; Werner, M.; Bielack, S. S. *J. Cancer Res. Clin. Oncol.* **2023**, *149*, 1961–1967.

(14) Rozeman, L. B.; Cleton-Jansen, A. M.; Hogendoorn, P. C. W. *Int. Orthop.* **2006**, *30*, 437–444.

(15) Kelley, L. M. et al. *J. Clin. Oncol.* **2020**, *38*, 823–833.

(16) Sun, Y.; Zhang, C.; Fang, Q.; Zhang, W.; Liu, W. *J. Transl. Med.* **2023**, *21*, 99.

(17) Schiavone, K.; Garnier, D.; Heymann, M.-F.; Heymann, D. *Adv. Exp. Med. Biol.* **2019**, *1139*, 187–200.

(18) Prater, S.; McKeon, B., *Osteosarcoma*; StatPearls Publishing: 2023.

(19) Taran, S. J.; Taran, R.; Malipatil, N. B. *Indian J. Med. Paediatr. Oncol.* **2017**, *38*, 33–43.

(20) Tiwari, A. *J. Clin. Orthop. Trauma* **2012**, *3*, 4–9.

(21) Bläsius, F.; Delbrück, H.; Hildebrand, F.; Hofmann, U. K. *Cancers (Basel)* **2022**, *14*, 2694.

(22) Simpson, E.; Brown, H. L. *JAAPA* **2018**, *31*, 15–19.

(23) Locquet, M.-A.; Brahmi, M.; Blay, J.-Y.; Dutour, A. *BMC Cancer* **2023**, *23*, 742.

(24) Ciernik, I. F.; Niemierko, A.; Harmon, D. C.; Kobayashi, W.; Chen, Y.-L.; Yock, T. I.; Ebb, D. H.; Choy, E.; Raskin, K. A.; Liebsch, N.; Hornicek, F. J.; DeLaney, T. F. *Cancer* **2011**, *117*, 4522–4530.

(25) Martin, T. W.; Griffin, L.; Custis, J.; Ryan, S. D.; Lafferty, M.; Boss, M.-K.; Regan, D.; Rao, S.; Leary, D.; Withrow, S. J.; LaRue, S. M. *Vet. Comp. Oncol.* **2021**, *19*, 284–294.

(26) Lian, H.; Zhang, J.; Hou, S.; Ma, S.; Yu, J.; Zhao, W.; Zhao, D.; Zhang, Z. *Front. Immunol.* **2024**, *15*, 1498060.

(27) Cè, M.; Cellina, M.; Ueanukul, T.; Carrafiello, G.; Manatrakul, R.; Tangkittithaworn, P.; Jaovisidha, S.; Fuangfa, P.; Resnick, D. *Cancers (Basel)* **2025**, *17*.

(28) Yarmish, G.; Klein, M. J.; Landa, J.; Lefkowitz, R. A.; Hwang, S. *Radiographics* **2010**, *30*, 1653–1672.

(29) Zhao, X.; Wu, Q.; Gong, X.; Liu, J.; Ma, Y. *Biomed. Eng. Online* **2021**, *20*, 24.

(30) Picci, P. *Orphanet J. Rare Dis.* **2007**, *2*, 6.

(31) Wittig, J. C.; Bickels, J.; Priebat, D.; Jelinek, J.; Kellar-Graney, K.; Shmookler, B.; Malawer, M. M. *Am. Fam. Physician* **2002**, *65*, 1123–1132.

(32) Gaillard, F.; Le, L.; Silverstone, L. In *Radiopaedia.org*; Radiopaedia.org: 2008.

(33) Oh, C.; Bishop, M. W.; Cho, S. Y.; Im, H.-J.; Shulkin, B. L. *J. Nucl. Med.* **2023**, *64*, 842–851.

(34) Manhard, M. K.; Uppuganti, S.; Granke, M.; Gochberg, D. F.; Nyman, J. S.; Does, M. D. *Bone* **2016**, *87*, 1–10.

(35) Nyman, J. S.; Ketsiri, T.; Louie, E. A.; Harkins, K. D.; Manhard, M. K.; Gochberg, D. F.; Lee, D. H.; Desai, M. J.; Maslow, J.; Tanner, S. B.; Does, M. D. *Bone* **2023**, *176*, 116863.

(36) Doblaré, M.; García, J. M.; Gómez, M. J. *Eng. Fract. Mech.* **2004**, *71*, 1809–1840.

(37) Menshikh, K.; Banicevic, I.; Obradovic, B.; Rimondini, L. *Tissue Eng. Part B Rev.* **2023**.

(38) Ott, S. M. *Am. J. Nephrol.* **2018**, *47*, 373–375.

(39) Shoaib, Z.; Fan, T. M.; Irudayaraj, J. M. K. *Br. J. Pharmacol.* **2022**, *179*, 201–217.

(40) Lee, R. K. L.; Chu, W. C. W.; Leung, J. H. Y.; Cheng, F. W. T.; Li, C. K. *Pediatr. Blood Cancer* **2013**, *60*, 1118–1121.

(41) Zhou, Y.; Lu, Q.; Xu, J.; Yan, R.; Zhu, J.; Xu, J.; Jiang, X.; Li, J.; Wu, F. *Oncotarget* **2017**, *8*, 73037–73049.

(42) Jepsen, K. J.; Silva, M. J.; Vashishth, D.; Guo, X. E.; van der Meulen, M. C. H. *J. Bone Miner. Res.* **2015**, *30*, 951–966.

(43) Main, R. P.; Shefelbine, S. J.; Meakin, L. B.; Silva, M. J.; van der Meulen, M. C. H.; Willie, B. M. *J. Orthop. Res.* **2020**, *38*, 233–252.

(44) Müller, D. A.; Silvan, U. *Int. J. Dev. Biol.* **2019**, *63*, 1–8.

(45) Holenstein, C. N.; Horvath, A.; Schär, B.; Schoenenberger, A. D.; Bollhalder, M.; Goedecke, N.; Bartalena, G.; Otto, O.; Herbig, M.; Guck, J.; Müller, D. A.; Snedeker, J. G.; Silvan, U. *Mol. Biol. Cell* **2019**, *30*, 887–898.

(46) Stylianopoulos, T.; Martin, J. D.; Chauhan, V. P.; Jain, S. R.; Diop-Frimpong, B.; Bardeesy, N.; Smith, B. L.; Ferrone, C. R.; Hornicek, F. J.; Boucher, Y.; Munn, L. L.; Jain, R. K. *Proc. Natl. Acad. Sci. U. S. A.* **2012**, *109*, 15101–15108.

(47) Chen, H.; Cai, Y.; Chen, Q.; Li, Z. *Biomech. Model. Mechanobiol.* **2020**, *19*, 577–590.

(48) Steffey, M. A.; Garcia, T. C.; Daniel, L.; Zwingenberger, A. L.; Stover, S. M. *Vet. Surg.* **2017**, *46*, 539–548.

(49) Achari, P. F.; Vickers, E.; Ruger, L.; Vlaisavljevich, E.; Tuohy, J.; Collins, C. J. *Front. Vet. Sci.* **2026**, *12*.

(50) Uluçkan, Ö.; Segaliny, A.; Botter, S.; Santiago, J. M.; Mutsaers, A. J. *BoneKEy Rep.* **2015**, *4*, 670.

(51) Bogusz, P.; Krasoń, W.; Pazur, K. *Materials (Basel)* **2024**, *17*, 2577.

(52) Thompson, M. S.; Schell, H.; Lienau, J.; Duda, G. N. *Med. Eng. Phys.* **2007**, *29*, 820–823.

(53) Lugas, A. T.; Terzini, M.; Stacchi, C.; Lombardi, T.; Di Donato, D.; Baldi, D.; Schierano, G.; Bignardi, C. *J. Phys. Conf. Ser.* **2022**, *2293*, 012011.

(54) Murienne, B. J.; Nguyen, T. D. *Opt. Lasers Eng.* **2016**, *77*, 92–99.

(55) Chen, H.; Li, H.; Liu, G.; Wang, Z. *Sensors (Basel)* **2024**, *24*, 4031.

(56) Palanca, M.; Tozzi, G.; Cristofolini, L. *Int. Biomech.* **2016**, *3*, 1–21.

(57) Cordey, J.; Gautier, E. *Injury* **1999**, *30 Suppl 1*, A7–13.

(58) Carriero, A.; Abela, L.; Pitsillides, A. A.; Shefelbine, S. J. *J. Biomech.* **2014**, *47*, 2490–2497.

(59) Sztefek, P.; Vanleene, M.; Olsson, R.; Collinson, R.; Pitsillides, A. A.; Shefelbine, S. *J. Biomech.* **2010**, *43*, 599–605.

(60) Pereira, A. F.; Javaheri, B.; Pitsillides, A. A.; Shefelbine, S. J. *J. R. Soc. Interface* **2015**, *12*, 0590.

(61) Begonia, M.; Dallas, M.; Johnson, M. L.; Thiagarajan, G. *Biomech. Model. Mechanobiol.* **2017**, *16*, 1243–1253.

(62) Farooq, S.; Leussink, S.; Sparrow, L. M.; Marchini, M.; Britz, H. M.; Manske, S. L.; Rolian, C. *Sci. Rep.* **2017**, *7*, 10527.

(63) Oliviero, S.; Cheong, V. S.; Roberts, B. C.; Orozco Diaz, C. A.; Griffiths, W.; Bellantuono, I.; Dall'Ara, E. *Front. Endocrinol. (Lausanne)* **2022**, *13*, 915938.

(64) Shim, J.; Iwaya, C.; Ambrose, C. G.; Suzuki, A.; Iwata, J. *Sci. Rep.* **2022**, *12*, 8117.

(65) Campbell, G. M.; Sophocleous, A. *BoneKEy Rep.* **2014**, *3*, 564.

(66) Buie, H. R.; Campbell, G. M.; Klinck, R. J.; MacNeil, J. A.; Boyd, S. K. *Bone* **2007**, *41*, 505–515.

(67) McCreadie, B. R.; Goldstein, S. A. *J. Bone Miner. Res.* **2000**, *15*, 2305–2308.

(68) Tripp, J. A.; Squire, M. E.; Hedges, R. E. M.; Stevens, R. E. *Palaeogeogr. Palaeoclimatol. Palaeoecol.* **2018**, *511*, 462–471.

(69) Kanis, J. A.; Kanis, J. A. *Osteoporos. Int.* **1994**, *4*, 368–381.

(70) Bala, Y.; Zebaze, R.; Ghasem-Zadeh, A.; Atkinson, E. J.; Iuliano, S.; Peterson, J. M.; Amin, S.; Bjørnerem, Å.; Melton 3rd, L. J.; Johansson, H.; Kanis, J. A.; Khosla, S.; Seeman, E. *J. Bone Miner. Res.* **2014**, *29*, 1356–1362.

(71) Van der Linden, Y. M.; Kroon, H. M.; Dijkstra, S. P. D. S.; Lok, J. J.; Noordijk, E. M.; Leer, J. W. H.; Marijnen, C. A. M.; Dutch Bone Metastasis Study Group *Radiother. Oncol.* **2003**, *69*, 21–31.

(72) Lindtner, R.; Kampik, L.; Putzer, D.; Klosterhuber, M.; Pallua, A. K.; Streif, W.; Schirmer, M.; Degenhart, G.; Arora, R.; Pallua, J. D. *Bioengineering (Basel)* **2025**, *12*.

(73) Whittier, D. E.; Boyd, S. K.; Burghardt, A. J.; Paccou, J.; Ghasem-Zadeh, A.; Chapurlat, R.; Engelke, K.; Bouxsein, M. L. *Osteoporos. Int.* **2020**, *31*, 1607–1627.

(74) Perilli, E.; Baleani, M.; Ohman, C.; Fognani, R.; Baruffaldi, F.; Viceconti, M. *J. Biomech.* **2008**, *41*, 438–446.

(75) Bjørnerem, Å. *BoneKEy Rep.* **2016**, *5*, 846.

(76) Zysset, P. K.; Dall'ara, E.; Varga, P.; Pahr, D. H. *BoneKEy Rep.* **2013**, *2*, 386.

(77) Imai, K. *World J Exp Med* **2015**, *5*, 182–187.

(78) Leslie, W. D.; Luo, Y.; Yang, S.; Goertzen, A. L.; Ahmed, S.; Delubac, I.; Lix, L. M. *J. Clin. Densitom.* **2019**, *22*, 338–345.

(79) Sternheim, A.; Giladi, O.; Gortzak, Y.; Drexler, M.; Salai, M.; Trabelsi, N.; Milgrom, C.; Yosibash, Z. *Bone* **2018**, *110*, 215–220.

(80) Jiwani, Z. M.; Ramiz, S. W. S. *J. Clin. Oncol.* **2021**, *39*, e22006–e22006.

(81) Fan, X.-L.; Cai, G.-P.; Zhu, L.-L.; Ding, G.-M. *Drug Des. Devel. Ther.* **2015**, *9*, 5925–5932.

(82) Ecklund, K.; Laor, T.; Goorin, A. M.; Connolly, L. P.; Jaramillo, D. *Radiology* **1997**, *202*, 543–547.

(83) King, T. J.; Georgiou, K. R.; Cool, J. C.; Scherer, M. A.; Ang, E. S. M.; Foster, B. K.; Xu, J.; Xian, C. J. *Am. J. Pathol.* **2012**, *181*, 121–129.

(84) Martinez, D.; Rodelo, J.; Pelaez García, S. *Cureus* **2022**, *14*, e22755.

(85) Ahn, J. H.; Cho, W. H.; Lee, J. A.; Kim, D. H.; Seo, J.-H.; Lim, J. S. *Ann. Pediatr. Endocrinol. Metab.* **2015**, *20*, 150–154.

(86) Hernandez, C. J.; van der Meulen, M. C. *J. Bone Miner. Res.* **2017**, *32*, 1157–1162.

(87) Pelker, R. R.; Friedlaender, G. E.; Panjabi, M. M.; Markham, T.; Hausman, M.; Doganis, A. C.; McKay, J. *J. Orthop. Res.* **1985**, *3*, 91–95.

(88) Van Leeuwen, B. L.; Verkerke, G. J.; Hartel, R. M.; Sluiter, W. J.; Kamps, W. A.; Jansen, H. W. B.; Hoekstra, H. J. *Clin. Orthop. Relat. Res.* **2003**, *413*, 243–254.

(89) Van Leeuwen, B. L.; Hartel, R.; Jansen, H. W. B.; Verkerke, G. J.; Veth, R. P. H.; Kamps, W. A.; Hoekstra, H. J. *Arch. Orthop. Trauma Surg.* **2004**, *124*, 503–506.

(90) Pendleton, M. M.; Emerzian, S. R.; Liu, J.; Tang, S. Y.; O'Connell, G. D.; Alwood, J. S.; Keaveny, T. M. *Bone* **2019**, *128*, 115043.

(91) Wernle, J. D.; Damron, T. A.; Allen, M. J.; Mann, K. A. *J. Biomech.* **2010**, *43*, 2738–2746.

(92) Bartlow, C. M.; Mann, K. A.; Damron, T. A.; Oest, M. E. *PLoS One* **2018**, *13*, e0204928.

(93) Emerzian, S. R.; Wu, T.; Vaidya, R.; Tang, S. Y.; Abergel, R. J.; Keaveny, T. M. *J. Bone Miner. Res.* **2023**, *38*, 1032–1042.

(94) Emerzian, S. R., *Role of radiation treatment on bone strength and fracture risk [dissertation*, Berkeley, CA; University of California, 2021.

(95) Altwal, J.; Martin, T. W.; Thamm, D. H.; Séguin, B. *Vet. Comp. Oncol.* **2023**, *21*, 131–137.

(96) Misof, B. M.; Fratzl-Zelman, N.; Paschalis, E. P.; Roschger, P.; Klaushofer, K. *BoneKEy Rep.* **2015**, *4*, 634.

(97) Ohba, T.; Cates, J. M. M.; Cole, H. A.; Slosky, D. A.; Haro, H.; Ichikawa, J.; Ando, T.; Schwartz, H. S.; Schoenecker, J. G. *Bone* **2014**, *63*, 110–120.

(98) Ryu, K.; Murata, H.; Koto, K.; Horie, N.; Matsui, T.; Nishigaki, Y.; Sakabe, T.; Takeshita, H.; Itoi, M.; Kimura, S.; Ashihara, E.; Maekawa, T.; Fushiki, S.; Kubo, T. *Anticancer Res.* **2010**, *30*, 2713–2720.

(99) Lassoued, H.; Lamy, O.; Francioli, C.; Gonzalez Rodriguez, E. *Front. Endocrinol. (Lausanne)* **2026**, *17*, 1761311.

(100) Ghouchani, A.; Ebrahimzadeh, M. H. *Arch. Bone Jt. Surg.* **2021**, *9*, 1–4.

(101) Dailey, H. L.; Kersh, M. E.; Collins, C. J.; Troy, K. L. *Curr. Osteoporos. Rep.* **2023**, *21*, 266–277.

(102) Garavelli, C.; Curreli, C.; Palanca, M.; Aldieri, A.; Cristofolini, L.; Viceconti, M. *PLoS One* **2022**, *17*, e0272529.

(103) Haider, I. T.; Lobos, S. M.; Simonian, N.; Schnitzer, T. J.; Edwards, W. B. *Osteoporos. Int.* **2018**, *29*, 2703–2715.

(104) Edwards, W. B.; Schnitzer, T. J.; Troy, K. L. *Bone* **2014**, *60*, 141–147.

(105) Luo, C.; Liao, J.; Zhu, Z.; Wang, X.; Lin, X.; Huang, W. *Biomed Res. Int.* **2019**, *2019*, 3503152.

(106) Morgan, E. F.; Unnikrisnan, G. U.; Hussein, A. I. *Annu. Rev. Biomed. Eng.* **2018**, *20*, 119–143.

(107) Oliviero, S.; Roberts, M.; Owen, R.; Reilly, G. C.; Bellantuono, I.; Dall'Ara, E. *Biomech. Model. Mechanobiol.* **2021**, *20*, 941–955.

(108) Rho, J. Y.; Hobatho, M. C.; Ashman, R. B. *Med. Eng. Phys.* **1995**, *17*, 347–355.

(109) Wagner, D. W.; Lindsey, D. P.; Beaupre, G. S. *Bone* **2011**, *49*, 931–938.

(110) Goyal, M.; Kalra, P. *Int. J. Sci. Res. (Raipur)* **2014**, *3*, 1848–1850.

(111) Brekhus, C.; Labus, K.; Seguin, B.; Puttlitz, C.; Gadomski, B. *Ann. Transl. Med.* **2024**, *12*, 5.

(112) Ammann, P.; Rizzoli, R. *Osteoporos. Int.* **2003**, *14 Suppl 3*, S13–8.

(113) Palomo, T.; Muszkat, P.; Weiler, F. G.; Dreyer, P.; Brandão, C. M. A.; Silva, B. C. *Arch. Endocrinol. Metab.* **2022**, *66*, 694–706.

(114) Nyman, J. S.; Roy, A.; Shen, X.; Acuna, R. L.; Tyler, J. H.; Wang, X. *J. Biomech.* **2006**, *39*, 931–938.

(115) Cai, Y.; Zioupos, P.; Márquez-Grant, N.; Budair, B.; Junaid, S. *Front. Bioeng. Biotechnol.* **2025**, *13*, 1670428.

(116) Khokhlova, V. A.; Fowlkes, J. B.; Roberts, W. W.; Schade, G. R.; Xu, Z.; Khokhlova, T. D.; Hall, T. L.; Maxwell, A. D.; Wang, Y.-N.; Cain, C. A. *Int. J. Hyperthermia* **2015**, *31*, 145–162.

(117) Yeo, S. Y.; Bratke, G.; Grüll, H. *Cancers (Basel)* **2022**, *15*, 108.

(118) Merckel, L. G.; Knuttel, F. M.; Deckers, R.; van Dalen, T.; Schubert, G.; Peters, N. H. G. M.; Weits, T.; van Diest, P. J.; Mali, W. P. T. M.; Vaessen, P. H. H. B.; van Gorp, J. M. H. H.; Moonen, C. T. W.; Bartels, L. W.; van den Bosch, M. A. A. J. *Eur. Radiol.* **2016**, *26*, 4037–4046.

(119) Uchida, T.; Ohkusa, H.; Nagata, Y.; Hyodo, T.; Satoh, T.; Irie, A. *BJU Int.* **2006**, *97*, 56–61.

(120) Wang, K.; Chen, Z.; Meng, Z.; Lin, J.; Zhou, Z.; Wang, P.; Chen, L.; Liu, L. *Int. J. Hyperthermia* **2011**, *27*, 101–107.

(121) Leslie, T.; Ritchie, R.; Illing, R.; Ter Haar, G.; Phillips, R.; Middleton, M.; Bch, B.; Wu, F.; Cranston, D. *Br. J. Radiol.* **2012**, *85*, 1363–1370.

(122) Hindley, J. et al. *AJR Am. J. Roentgenol.* **2004**, *183*, 1713–1719.

(123) Wu, F.; Wang, Z.-B.; Zhu, H.; Chen, W.-Z.; Zou, J.-Z.; Bai, J.; Li, K.-Q.; Jin, C.-B.; Xie, F.-L.; Su, H.-B. *Radiology* **2005**, *236*, 1034–1040.

(124) Yu, W.; Tang, L.; Lin, F.; Yao, Y.; Shen, Z.; Zhou, X. *Surg. Oncol.* **2015**, *24*, 9–15.

(125) Li, C.; Zhang, W.; Fan, W.; Huang, J.; Zhang, F.; Wu, P. *Cancer* **2010**, *116*, 3934–3942.

(126) Yeo, S. Y.; Arias Moreno, A. J.; van Rietbergen, B.; Ter Hoeve, N. D.; van Diest, P. J.; Grüll, H. *J. Ther. Ultrasound* **2015**, *3*, 13.

(127) Smith, N. B.; Temkin, J. M.; Shapiro, F.; Hynynen, K. *Ultrasound Med. Biol.* **2001**, *27*, 1427–1433.

(128) Xu, Z.; Hall, T. L.; Vlaisavljevich, E.; Lee Jr, F. T. *Int. J. Hyperthermia* **2021**, *38*, 561–575.

(129) Roberts, W. W. *Curr. Opin. Urol.* **2014**, *24*, 104–110.

(130) Mauri, G.; Nicosia, L.; Xu, Z.; Di Pietro, S.; Monfardini, L.; Bonomo, G.; Varano, G. M.; Prada, F.; Della Vigna, P.; Orsi, F. *Br. J. Radiol.* **2018**, *91*, 20170641.

(131) Ruger, L. N.; Hay, A. N.; Gannon, J. M.; Sheppard, H. O.; Coutermarsh-Ott, S. L.; Daniel, G. B.; Kierski, K. R.; Ciepluch, B. J.; Vlaisavljevich, E.; Tuohy, J. L. *IEEE Trans. Biomed. Eng.* **2022**, *PP*.

(132) Allen, S. P.; Hall, T. L.; Cain, C. A.; Hernandez-Garcia, L. *Magn. Reson. Med.* **2015**, *73*, 204–213.

(133) Vlaisavljevich, E.; Owens, G.; Lundt, J.; Teofilovic, D.; Ives, K.; Duryea, A.; Bertolina, J.; Welling, T. H.; Xu, Z. *Ultrasound Med. Biol.* **2017**, *43*, 1237–1251.

(134) Schade, G. R.; Keller, J.; Ives, K.; Cheng, X.; Rosol, T. J.; Keller, E.; Roberts, W. W. *J. Urol.* **2012**, *188*, 1957–1964.

(135) Schade, G. R.; Wang, Y.-N.; D'Andrea, S.; Hwang, J. H.; Liles, W. C.; Khokhlova, T. D. *Ultrasound Med. Biol.* **2019**, *45*, 137–147.

(136) Hendricks, A. D.; Howell, J.; Schmieley, R.; Kozlov, S.; Simon, A.; Coutermarsh-Ott, S. L.; Vlaisavljevich, E.; Allen, I. C. *J. Immunol.* **2019**, *202*, 194.30–194.30.

(137) Gannon, J. et al. *Int. J. Hyperthermia* **2023**, *40*, 2247187.

(138) Arnold, L.; Hendricks-Wenger, A.; Coutermarsh-Ott, S.; Gannon, J.; Hay, A. N.; Dervisis, N.; Klahn, S.; Allen, I. C.; Tuohy, J.; Vlaisavljevich, E. *Ultrasound Med. Biol.* **2021**, *47*, 3435–3446.

(139) Ruger, L. N.; Hay, A. N.; Vickers, E. R.; Coutermarsh-Ott, S. L.; Gannon, J. M.; Covell, H. S.; Daniel, G. B.; Laeseke, P. F.; Ziemlewicz, T. J.; Kierski, K. R.; Ciepluch, B. J.; Vlaisavljevich, E.; Tuohy, J. L. *Cancers (Basel)* **2023**, *15*, 741.

(140) Guijarro, M. V.; Ghivizzani, S. C.; Gibbs, C. P. *Front. Oncol.* **2014**, *4*, 189.

(141) Simpson, S.; Rizvanov, A. A.; Jeyapalan, J. N.; de Brot, S.; Rutland, C. S. *Front. Vet. Sci.* **2022**, *9*, 965391.

(142) Makielski, K. M.; Mills, L. J.; Sarver, A. L.; Henson, M. S.; Spector, L. G.; Naik, S.; Modiano, J. F. *Vet. Sci. China* **2019**, *6*.

(143) Pu, F.; Guo, H.; Shi, D.; Chen, F.; Peng, Y.; Huang, X.; Liu, J.; Zhang, Z.; Shao, Z. *Genes Dis.* **2024**, *11*, 664–674.

(144) Mason, N. J. *Adv. Exp. Med. Biol.* **2020**, *1258*, 199–221.

(145) Lazarides, A. L.; Putterman, A. B.; Eward, W. C.; Eward, C. *Osteosarcoma–Biology, behavior and mechanisms* **2017**.

(146) Autefage, A.; Palierne, S.; Charron, C.; Swider, P. *Vet. J.* **2012**, *194*, 202–209.

(147) Reilly, D. T.; Burstein, A. H. *J Biomech* **1974**, *7*, 271–275.

(148) Vahey, J. W.; Lewis, J. L.; Vanderby Jr, R. *J. Biomech.* **1987**, *20*, 29–33.

(149) Kuhn, J. L.; Goldstein, S. A.; Ciarelli, M. J.; Matthews, L. S. *J. Biomech.* **1989**, *22*, 95–107.

(150) Liao, A. T.; McMahon, M.; London, C. A. *Anim. Genet.* **2006**, *37*, 248–252.

(151) Dass, C. R.; Ek, E. T. H.; Choong, P. F. M. *J. Cancer Res. Clin. Oncol.* **2007**, *133*, 193–198.

(152) Berlin, O.; Samid, D.; Donthineni-Rao, R.; Akeson, W.; Amiel, D.; Woods Jr, V. L. *Cancer Res.* **1993**, *53*, 4890–4895.

(153) Khanna, C.; Prehn, J.; Yeung, C.; Caylor, J.; Tsokos, M.; Helman, L. *Clin. Exp. Metastasis* **2000**, *18*, 261–271.

(154) Hay, A. N.; Imran, K. M.; Hendricks-Wenger, A.; Gannon, J. M.; Sereno, J.; Simon, A.; Lopez, V. A.; Coutermarsh-Ott, S.; Vlaisavljevich, E.; Allen, I. C.; Tuohy, J. L. *Biomedicines* **2023**, *11*.

(155) Walkley, C. R.; Qudsi, R.; Sankaran, V. G.; Perry, J. A.; Gostissa, M.; Roth, S. I.; Rodda, S. J.; Snay, E.; Dunning, P.; Fahey, F. H.; Alt, F. W.; McMahon, A. P.; Orkin, S. H. *Genes Dev.* **2008**, *22*, 1662–1676.

(156) Ng, A. J.; Mutsaers, A. J.; Baker, E. K.; Walkley, C. R. *Clin. Sarcoma Res.* **2012**, *2*, 19.

(157) Lavigueur, A.; Maltby, V.; Mock, D.; Rossant, J.; Pawson, T.; Bernstein, A. *Mol. Cell. Biol.* **1989**, *9*, 3982–3991.

(158) Sereno, J.; Hendricks, A. D.; Allen, I. C.; Vlaisavljevich, E.; Imran, K. M.; Tuohy, J. *J. Immunol.* **2021**, *206*, 64.20–64.20.

(159) Hay, A. N.; Ruger, L.; Hsueh, A.; Vickers, E.; Klahn, S.; Vlaisavljevich, E.; Tuohy, J. *Int. J. Hyperthermia* **2023**, *40*, 2274802.

(160) Oliviero, S.; Lu, Y.; Viceconti, M.; Dall'Ara, E. *J. Biomech.* **2017**, *65*, 203–211.

(161) Collier, C. D.; Hausman, B. S.; Zulqadar, S. H.; Din, E. S.; Anderson, J. M.; Akkus, O.; Greenfield, E. M. *Bone Rep.* **2020**, *12*, 100250.

(162) Jiang, F.; Liu, S.; Chen, A.; Li, B.-Y.; Robling, A. G.; Chen, J.; Yokota, H. *Int. J. Orthop. (Hong Kong)* **2018**, *5*, 863–871.

(163) Jarvis, S.; Koumadoraki, E.; Madouros, N.; Sharif, S.; Saleem, A.; Khan, S. *Cancer Treat. Res. Commun.* **2021**, *27*, 100307.

(164) Gannon, J. et al. *Ultrasound Med. Biol.* **2026**, *52*, 62–71.

(165) Kim, Y.; Fifer, C. G.; Gelehrter, S. K.; Owens, G. E.; Berman, D. R.; Vlaisavljevich, E.; Allen, S. P.; Ladino-Torres, M. F.; Xu, Z. *Ultrasound Med. Biol.* **2013**, *39*, 1047–1055.

(166) Malhotra, A.; Pelletier, M. H.; Yu, Y.; Christou, C.; Walsh, W. R. *Front. Surg.* **2014**, *1*, 37.

(167) Sun, S.; Zhang, H.; Wang, Q.; Zhu, D.; Wen, Y. *Sci. Rep.* **2025**, *15*, 8232.

Chapter 3

Assessment of Histotripsy as a Bone-sparing Tumor Ablation Technique in Ex Vivo Osteosarcoma Tumor-affected Limbs

The following work evaluates the biomechanical effects of histotripsy on OS-affected and grossly normal bone via μCT analysis and mechanical testing. This study represents the first mechanical assessment of histotripsy-treated bone tissue, providing critical insights into treatment safety and limb-sparing potential. The results were published in *Frontiers in Veterinary Science* in January 2026[1].

3.1 Abstract

Osteosarcoma (OS) is an aggressive bone cancer that is highly resistant to conventional therapies. Histotripsy is a non-invasive, non-thermal ablation technique that uses ultrasound to mechanically destroy tissue and has been recently explored as a novel treatment for OS in a canine comparative anatomy model with heterogeneous tumor phenotypes consisting of mixed lytic and sclerotic lesions. However, the effects of histotripsy on the biomechanics of OS tumor-affected bone and surrounding grossly normal bone have not been investigated.

The aim of this study was to evaluate the biomechanical effects of histotripsy on OS tumor-affected and normal bone and to characterize tumor heterogeneity. Using ex vivo limbs from canine OS patients, histotripsy ablation was performed on tumor-affected and normal bone specimens, with corresponding unablated tumor and normal controls. Mechanical testing, including uniaxial compression and 3-point bending, revealed significantly higher elastic and post-yield properties in normal bone specimens compared to tumor-affected specimens. No significant differences were detected within normal or within tumor-affected bone groups, indicating that histotripsy does not detrimentally affect the structural integrity of normal bone or further damage that of tumor-affected bone. Trabecular unablated tumor specimens exhibited higher and broader elastic modulus and ultimate strength values compared to other groups, highlighting OS tumor heterogeneity. CT analysis confirmed this variability, demonstrating differences in bone volume fraction across specimens. The results of the current work support the development and advancement of histotripsy as an effective, non-invasive, bone-sparing, and patient-specific treatment option for clinical OS.

3.2 Introduction

Osteosarcoma (OS) is an aggressive bone cancer that represents the most common bone malignancy in children and adolescents.[2,3] It accounts for <1% of all cancers in humans and has an incidence rate of 1.2/100,000 cases/year[3–5]. The 5-year survival rate for patients with primary OS is approximately 75%; however, this rate drops dramatically to 30-35% for those who present with pulmonary metastases. This significant reduction highlights the challenge posed by metastatic disease, which has remained largely resistant to therapy and has contributed to the stagnation in survival rates over the past decades[2,4,6]. The current standard of treatment involves a combination of chemotherapy and surgical resection; however, some patients may not qualify for surgical resection due to tumor location, insufficient treatment margins, involvement with critical structures, or presence of metastatic disease[6,7]. Patients

who receive standard treatment may still develop metastasis. Surgical treatment to resect the primary tumor is associated with potential complications and co-morbidities including infection and reduced limb mobility and function[6,8,9]. Non-surgical limb salvage options for treating the primary tumor remain extremely limited.

Canines have previously been used in osteological studies as comparative animal models. Studies have shown that adult dogs exhibit bone remodeling and age-related changes that are analogous to those present in human osteoporosis[10–12]. Kuhn et al. and Vahey et al. found qualitative similarities between the mechanical properties of human and canine trabecular bone[12,13]. The long bones of humans and canines also have similar cortical microstructure and vascularization, making the canine an ideal choice for comparative osteological studies regarding the biomechanics of bone[13]. Canines have also been established as a strong comparative oncology model for human OS. Canine OS develops spontaneously, and its incidence rate is 10-30x higher than that of human OS[14,15]. Canine OS also shares several biological characteristics with human OS, such as disease presentation, response to treatment, genetic complexity, and histological characteristics[14–16]. OS accounts for over 85% of bone tumors in canines, with 95% of patients presenting with spontaneous micrometastases and high levels of pain at time of diagnosis. Cure is achieved in fewer than 15% of dogs[15]. Current treatment options for canine OS are similar to those for human OS, the most common involving tumor resection via limb-amputation or limb-salvage surgery and adjuvant chemotherapy. Some dogs may not qualify for limb amputation, and serious complications after limb-salvage surgery such as implant failure and infection occur in 30-70% of patients[17,18]. These similarities between canine and human OS render the dog an ideal model for comparative and translational OS research[14,15]. Given the challenges outlined with current surgical treatment of canine and human OS, novel, non-invasive treatment options for canine OS are sorely needed.

Histotripsy is a non-invasive, non-thermal ablation technique that uses ultrasound to mechanically destroy tissue. Unlike thermally ablative forms of ultrasound, such as high-intensity

focused ultrasound (HIFU), histotripsy relies on inertial cavitation; microsecond-long, high-pressure pulses generate microbubbles that rapidly expand and collapse, subjecting cells to high levels of stress and strain and effectively liquefying target tissue[19]. This eliminates heat sink effects due to perfusion, which are common issues in thermal ablation methods and can lead to injury or ineffective treatment[19–21]. Since histotripsy relies on mechanical, rather than thermal or biochemical, interactions, it can achieve sub-millimeter precision and discriminate between tissues based on mechanical stiffness[22,23]. Histotripsy has been investigated as a cancer treatment in pre-clinical applications regarding liver[24–26], prostate[27], renal[28], breast[29], brain[30,31], and pancreatic[32,33] cancer as well as in soft tissue sarcomas[34]. Extending histotripsy to bone tumors, however, has introduced unique challenges not present in soft tissue, including ultrasound energy reflection from mineralized structures and the highly heterogeneous composition of tumor lesions[35]. Despite these challenges, recent studies have demonstrated the safety and feasibility of histotripsy for treating bone tumors through both *in vivo*[36] and *ex vivo*[35] ablation of canine OS tissue. In these studies, histotripsy effectively ablated localized regions of primary OS tumor tissue without causing cell death or damage to normal tissue outside the ablation zone at the same dose[22,35,36]. Tissue selectivity has also been demonstrated *invivo*, in which structures such as the extracellular matrix, blood vessels and nerves within the ablation zone remain structurally intact because their stiffnesses differ from that of the target tissue[35,37,38]. These findings establish a foundation for whole-tumor ablation and the development of effective post-treatment management strategies. However, the genomic instability exhibited by OS leads to highly heterogeneous tumors which often consist of mixed lytic and sclerotic lesions, making it difficult to effectively target and treat the entire tumor[39]. Furthermore, OS frequently invades the cortical bone, compromising its structure and, consequently, its mechanical integrity and strength, which may lead to pathological fracture. The prognosis for OS patients with pathological fractures is poor, involving complications such as fracture hematoma or the spread of micro-metastases[40–42]. To address these challenges, it is critical to characterize the effects of histotripsy on the biomechanics

of OS tumor-affected bone and how these properties vary spatially throughout the tumor.

Mechanical testing methods such as compression, tensile, nanoindentation, and fracture toughness tests have been used for decades to determine the material properties of bone at the cellular, tissue, and whole bone levels[43,44]. Kuhn et al. and Romanus have characterized the material properties (e.g. elastic modulus, ultimate stress) of canine trabecular and cortical bone via compression and flexural testing, respectively[12,45]. Key properties such as elastic modulus and yield strain derived from the resulting stress-strain curves give insight into a material's behavior both pre- and post-yield. Coupled with powerful, high-resolution imaging modalities such as CT, the gold standard for bone microarchitecture assessment, these methods can also facilitate the development of a relationship between CT intensity, bone mineral density, and elastic modulus, offering insight into structural heterogeneity within a tumor[46–49]. The objective of this study was to 1) to determine the effects of histotripsy on the biomechanics of OS tumor-affected and grossly normal bone; and 2) characterize OS tumor heterogeneity. In this study, compression and flexural, namely 3-point bending, tests were utilized to quantify elastic and post-yield mechanical properties of trabecular and cortical bone from ex vivo canine limbs, amputated as part of standard of care treatment for OS. The resultant biomechanics and CT imaging data serve as crucial next steps in developing histotripsy as a safe, effective limb-salvage treatment option for OS.

3.3 Methods

Amputated limbs (n=10) from canine patients (n = 9, 6.6+2.9 years, 33.5+8.36 kg) with primary OS tumors undergoing standard-of-care limb amputation at the Virginia-Maryland Veterinary Teaching Hospital (Blacksburg, VA) were acquired under an approved institutional IACUC protocol (22-091). Patients were enrolled according to predefined criteria, including 1) histologic or radiographic evidence of appendicular OS, 2) no radiographic

evidence of pulmonary metastasis, and 3) no previous use of cancer therapy at time of enrollment.(35) Patient demographic information is shown in Table 6.1. Pre-treatment MRI or CT scans were taken of OS-bearing limbs (n=6) to determine the tumor volume for histotripsy ablation, after which patients underwent standard-of-care limb amputation. Imaging modality varied as our clinical team transitioned from CT to MRI for treatment planning and ablation assessment. MRI offers superior soft tissue contrast and provides a more precise assessment of tumor extent and boundaries than CT[50–52]. As only the affected limb was surgically removed during standard-of-care treatment and patients remained under clinical care post-operatively, matching healthy (i.e. non-tumor bearing), contralateral limbs were not available for analysis for most patients. In one case, however, both an OS-bearing limb and a grossly normal limb were obtained from the same patient after receiving owner consent for limb excision after euthanasia. Untreated tumor tissue specimens were collected immediately following limb amputation for histological confirmation of OS. Histotripsy treatments were performed using a custom 32-element 500 kHz histotripsy transducer within 48 hours post-amputation to minimize tissue degradation and to preserve biomechanical and histological integrity. Pulses of 1-2 cycles (pulse duration: 2-4 s) were applied to the center of OS tumor samples and a matching volume of grossly normal bone at a pulse repetition frequency of 500 Hz with 1000 pulses/point, as described in previous studies regarding histotripsy ablation of canine OS[22,35]. Grossly normal bone was identified adjacent to the tumor, often from the opposing end (proximal vs distal) or in neighboring bones across a joint (tibia vs femur). Histotripsy treatments were guided in real-time using an ultrasound imaging probe (Model C5-2, Analogic Corporation, Peabody, MA, USA), and the cavitation cloud threshold for each sample was determined by visualizing the cavitation cloud and gradually increasing the pressure at the focus until a consistent cloud was observed on real-time ultrasound imaging[35,37]. Targeted volumes ranged from 10.1-24.0 cm3 and peak negative pressures, applied 20% above the cavitation threshold, ranged from 26.5-35.7 MPa. Post-treatment of the tumor-bearing limb, the affected bone was resected and split along the anatomical

axis for biomechanical and histological analysis. Specimens for biomechanical analysis were stored at -20°C until testing. Given that the tissue was not fixed, time between amputation and storage was limited to 48 hours post-amputation. Bone tissue from ablated tumor (AT, n=9), ablated normal bone (AN, n=10), unablated tumor (UT, n=7), and unablated normal bone (UN, n=16) were then extracted for biomechanical testing (Figure 6.1a). Treated and untreated tumor specimens were collected from different limbs, as the goal of the histotripsy treatment was to ablate as much of the tumor as possible.

Table 3.1: Demographic information for all patients

Patient	Breed	Age (years)	Gender	Weight (kg)	Tumor location
1	Greyhound	8	FS	30.7	Distal radius
2	Boxer	3	MN	30	Medial humeral condyle
3	Golden Retriever	1	MN	25	Distal ulna
4	Cane Corso	9	FS	50.4	Proximal humerus
5	Mixed breed	9	FS	25.9	Proximal tibia
6	Boxer	5	FS	26.1	Distal radius
7	Golden Retriever	9	FS	40	Proximal humerus
8	Golden Retriever	7	MN	35.5	Distal humerus
9	Great Dane	8	MN	38.3	Distal radius

Cubic specimens (7.5mm x 7.5mm x 7.5mm) were cut from the trabecular bone sections using an IsoMet low-speed precision saw under constant irrigation. The edges of the cubes were cut parallel to the primary axis of loading (Z) shown in Figure 6.1b. These samples were placed centrally between two steel compression disks mounted to an MTS Insight 10 materials testing system. Preconditioning cycles (n=5) ranging from 20-100N were applied at a loading rate of 0.01mm/s to ensure full engagement of the sample surface with the compression platens before testing. Then, repeat uniaxial compressive loading (n=3) was performed at a strain rate of 1%/s with a 20N preload in three anatomical directions (superior-inferior, medial-lateral, and anterior-posterior) until just under 3% strain to assess tissue anisotropy and to determine the compressive modulus of each sample. Compression to failure (10%

strain) along the primary axis of loading (Z-axis, Figure 6.1b) was performed to determine the yield and ultimate compressive stresses of each sample. Rectangular beam specimens (15mm x 2mm x 1mm) of cortical bone were cut from the diaphysis of each tissue region along the longitudinal bone axis. Specimens were subjected to 3-point bending until failure (ElectroForce 3200) with a constant displacement rate of 0.05mm/min and a support span of 12mm to evaluate pre- and post-yield cortical bone properties.

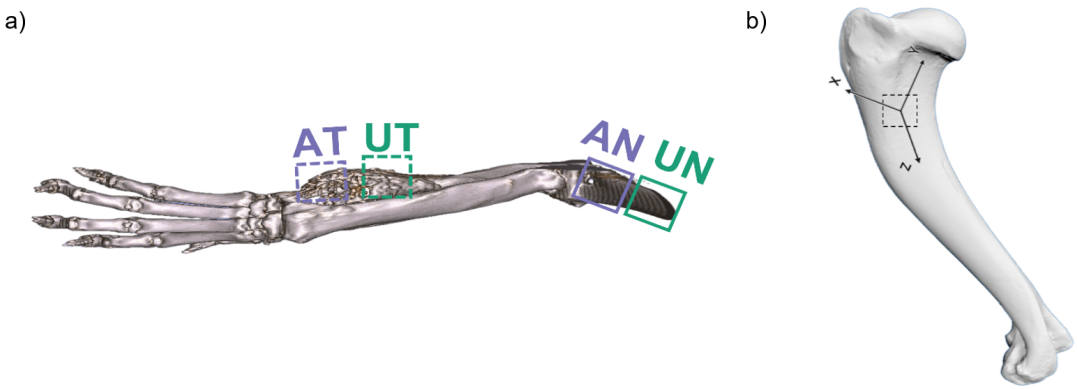

Figure 3.1: a) Representative 3D model of an OS tumor-bearing canine forelimb, generated from CT image data, with anatomical locations identified from which the ablated tumor (AT), unablated tumoe (UT), ablated normal (AN), and unablated normal (UN) cortical and trabecular bone specimens were excised– distal radius and distal ulna. b) The primary axis of loading (z-axis) for each bone was identified and utilized to define the remaining principal directions (x- and y-axis) for the trabecular bone specimens– canine humerus.

Trabecular, humeral UT specimens were micro-CT scanned (Bruker SkyScan 1172) prior to mechanical testing at a voxel resolution of 17.5x17.5x17.5 m (60kV, 167 A) for assessment. Specimens were placed in conical test tubes, submerged completely in phosphate buffer solution (PBS, pH 7.4, Sigma Aldrich), and mounted in a cylindrical specimen holder stabilized with a foam mold. Regions of interest (ROIs) were chosen to be uniform in size and space across specimens. Three-dimensional reconstructions of each specimen were obtained from the scans using scanner software and visualized in 3D Slicer. Binarized segmentation masks were created using 3D Slicer's Otsu thresholding method to identify mineralized bone from background. These masks were then used to calculate the trabecular bone volume fraction (BV/TV) of each specimen.

All trabecular and cortical specimens were stored at -20°C prior to testing and were kept hydrated with sprays of deionized water during testing to maintain mechanical integrity. All testing was performed within two months of limb amputation and ex vivo histotripsy treatment. For compression tests, stress (σ) and strain (ε) were calculated as follows[53]:

$$\sigma = \frac{F}{A} \tag{3.1}$$

$$\varepsilon = \frac{\Delta L}{L_0} \tag{3.2}$$

Where F is the applied load, A is the cross-sectional area of the specimen, ΔL is the crosshead displacement, and L_0 is the gauge length of the specimen. For 3-pt bending tests, stress and strain were calculated as follows[53]:

$$\sigma = \frac{3FL}{2bd^2} \tag{3.3}$$

$$\varepsilon = \frac{6Dd}{L^2} \tag{3.4}$$

Where L is the span length, D is the crosshead displacement at the midpoint of the specimen, and b and d are its width and thickness, respectively. Compressive and bending moduli were derived from the linear region of the stress-strain curves, consistent with Hooke's law, which relates stress to strain in elastic deformation.[53] Ultimate strength was also determined for both trabecular and cortical specimens to assess the impact of histotripsy on tissue strength, while compressive and bending moduli were used to evaluate tissue stiffness.

All statistics were performed in Python 3.9 (statsmodels 0.13.2, scipy 1.7.3). A linear mixed effects model was used to assess the impact of loading direction and tissue on the pre-

yield properties of the trabecular bone specimens. Due to the nonparametric nature of the collected data, a Kruskal-Wallis test was used to assess elastic and post-yield behavior of both the trabecular and cortical bone specimens; where necessary, Dunn's test was performed as a post-hoc measure to compare data between groups. The alpha value was set at 0.05 and p-values were adjusted for multiple comparisons. Coefficient of variation (CV), calculated as the ratio of the standard deviation to the mean, was also determined for each sample to assess the reproducibility of repeated uniaxial loading tests.

3.4 Results

The mechanical properties of 47 trabecular cubic specimens were analyzed. Cube dimensions varied by <2% in all directions. Mean CVs from repeat pre-yield compression tests for each group ranged from 4.6-13.5%, with the majority of specimens (85%) exhibiting CVs below 15%. Elastic modulus was significantly higher in UT specimens than in UN, AN, and AT specimens (p=0.0011, p=0.0026, p=0.0022, respectively). No significant differences were found in post-yield properties between groups; however, UT specimens exhibited a higher value and range regarding ultimate strength, and a higher range regarding yield stress and strain than the other groups (Figure 6.2a, Table 3.2). The BV/TV of these specimens was measured, with a mean of 0.411±0.166. CT analysis of UT specimens revealed a wide range of trabecular densities, highlighting high levels of tumor heterogeneity and a linear, albeit weak ($R^2 = 0.39$), trend between UT BV/TV and elastic modulus (Figure 6.3). Regarding anisotropy, stiffness was often higher in the primary loading direction for UN and UT specimens, but no significant differences were found within the three loading directions between unablated tissue groups. Stiffness in the primary loading direction for AN and AT specimens was significantly higher than in the other two directions (p=0.035, p<0.001, respectively).

The mechanical properties of 67 cortical beams were analyzed. Beam dimensions varied by <3% in all directions. Ultimate strength, taken from the point of highest load, was significantly higher in grossly normal bone (UN and AN) groups than in tumor tissue (UT and AT) groups. No significant differences were found within normal bone groups or within tumor tissue groups. Elastic modulus followed a similar trend; normal bone specimens were significantly stiffer than tumor tissue specimens, and no differences were found within normal bone groups or within tumor tissue groups (Figure 6.2b, Table 3.2). Toughness values were significantly higher in AN specimens than in AT and UT specimens (p=0.003, 0.003, respectively).

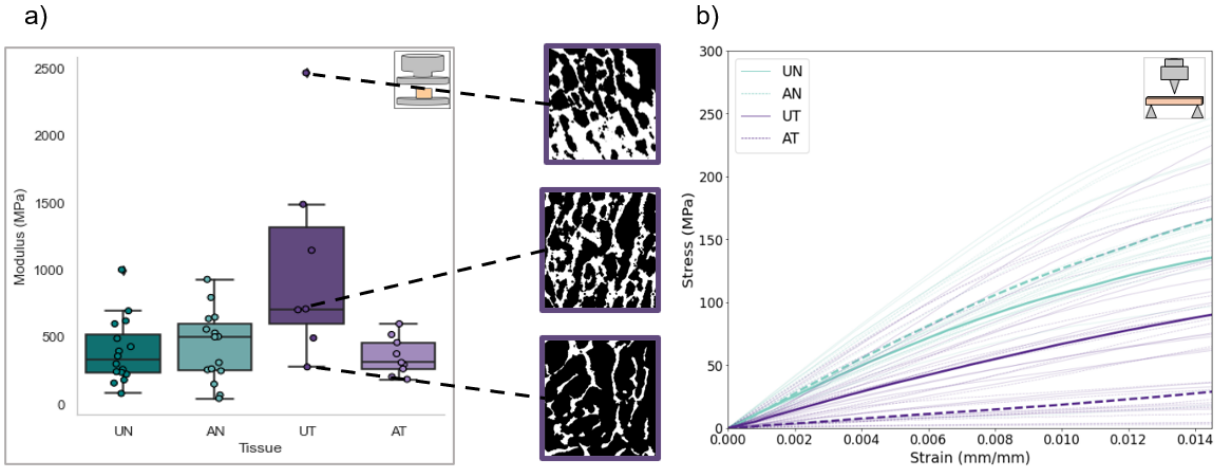

Figure 3.2: a) Elastic modulus distribution for a) cortical bone and b) trabecular bone specimens. CT slices of select UT specimens prepared for compression testing, demonstrating the range in bone volume fraction of the trabecular network.

Table 3.2: Material property data for trabecular and cortical bone specimens. Data reported as mean ± standard deviation or median (IQR).

Test Type	**Property**	**UN (n=16)**	**AN (n=10)**	**UT (n=7)**	**AT (n=9)**	**(p)**
Compression	Ultimate strength (MPa)	15.1 ± 8.06	15.0 ± 11.7	33.0 ± 18.3	14.9 ± 7.00	0.089
	Compressive modulus (MPa)	389 ± 241	427 ± 264	728 ± 446	354 ± 143	$\ll 0.001^*$
	Yield strength (MPa)	10.0 (9.40)	13.5 (12.5)	13.3 (21.4)	9.58 (9.30)	0.461
	Yield strain (%)	2.66 (0.631)	2.42 (1.21)	2.79 (2.10)	3.01 (0.691)	0.290
Bending	Ultimate strength (MPa)	189 (99.1)	214 (63.6)	116 (109)	115 (114)	$\ll 0.001^*$
	Bending modulus (GPa)	12.2 (6.85)	12.0 (4.91)	6.57 (6.47)	4.95 (7.07)	$\ll 0.001^*$
	Elastic work (J)	1.05 (0.401)	1.11 (0.341)	1.05 (0.766)	0.992 (1.07)	0.956
	Toughness (MJ/m^3)	3.93 (1.97)	8.35 (5.74)	2.80 (2.27)	2.23 (3.22)	$\ll 0.001^*$

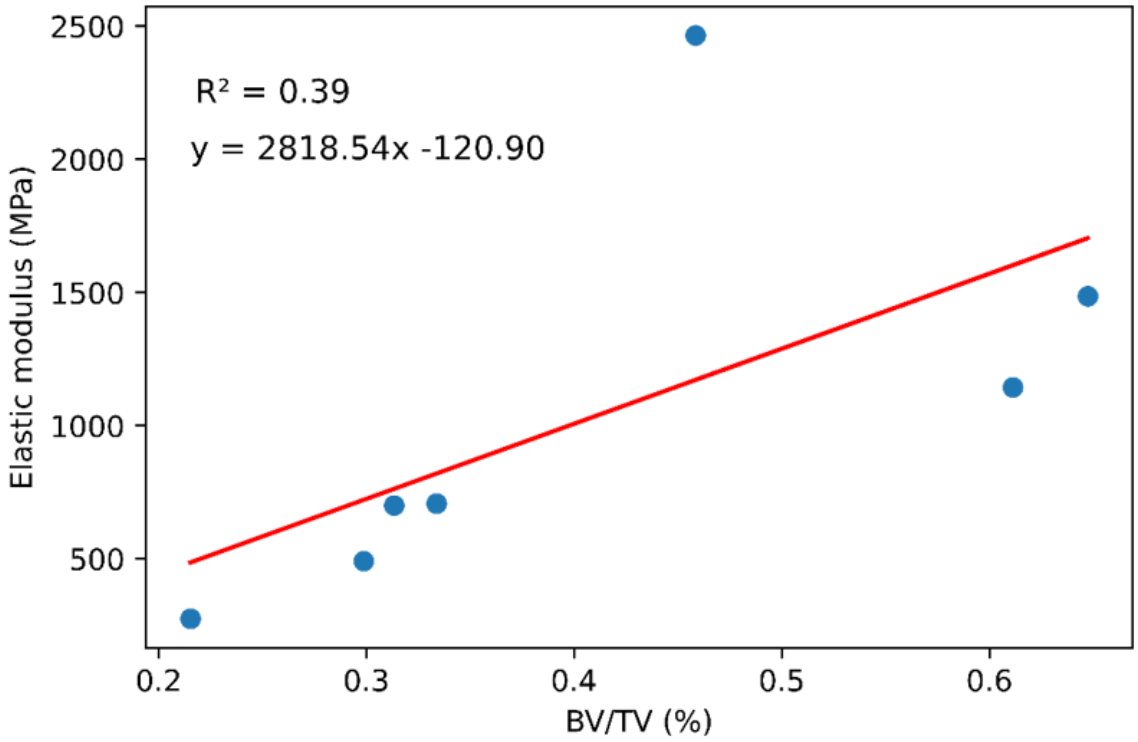

Figure 3.3: Relationship between BV/TV and elastic modulus of trabecular UT samples.

3.5 Discussion

The aim of the proposed study was to evaluate the biomechanical effects of histotripsy on OS tumor-affected and normal bone. This study successfully demonstrated that histotripsy ablation at clinical doses does not detrimentally affect the mechanical properties of normal bone, as no significant differences were observed between histotripsy-ablated and unablated normal bone. Similarly, the lack of differences in the mechanical properties of ablated and unablated tumor-affected cortical bone suggests that histotripsy treatment does not further compromise the structural integrity of tumor-affected bone. For standard-of-care surgical approaches, resection typically includes 2–3cm of surrounding bone and soft tissue to ensure complete excision of malignant cells[54,55]. In this study, histotripsy was applied without a margin; however, future applications may incorporate a conservative margin to effectively

target microscopic disease, similar in concept to those implemented in radiation therapy[56]. These results indicate that such a treatment margin could be feasible without further compromising bone integrity. Together, these findings support the histotripsy's potential as an effective treatment for OS tumors that does not increase risk of fracture in the affected limb. These tissue-selective features offer the potential for effective tumor ablation near critical structures, which has been a problem for other therapeutic interventions such as thermal ablation and radiation; thermal ablation methods such as HIFU often expose tissue to temperatures exceeding 50°C, leading to cell lysis, protein denaturation, and necrosis[57,58], while therapeutic doses of radiation have been reported to modify the histology of bone, damage its structural integrity, and delay healing[59–61]. The vessel-sparing and duct-sparing features of histotripsy are well established in the treatment of liver cancer, enabling safer and more effective tumor ablation compared to thermal-based approaches in both preclinical and clinical studies[24–26]. The findings in this study suggest that histotripsy's tissue-selective and bone-sparing properties can similarly be used for the treatment of OS. By effectively ablating tumors without increasing fracture risk, histotripsy represents a promising alternative for addressing the limitations of existing therapeutic modalities.

Histotripsy's ability to preserve the mechanical integrity of bone is highly significant given the already-compromised nature of OS-affected bone. The altered mechanical integrity of tumor-affected bone may increase the risk of pathological fracture, which occurs in 5-10% of patients and is a significant clinical concern[62,63]. Patients who present with pathological fractures have an increased risk of local recurrence, spread of micrometastases, and decreased survival rates[64,65]. This is further exacerbated by the highly variable mechanical phenotype of OS-affected bone, caused by its heterogenous nature. For example, lytic regions may have a catabolic effect, promoting bone degradation and structural weakening, while sclerotic regions induce an anabolic response, producing abnormally dense bone that is stiffer but potentially more brittle[66]. This variability complicates risk assessment and highlights the importance of optimizing histotripsy strategies to ensure effective ablation across varied

tumor compositions. Future studies will incorporate high-resolution CT imaging on all tumor-affected specimens to characterize lesion morphology and better quantify material properties. This will allow correlation of lesion composition with mechanical performance and treatment outcomes, ultimately informing patient-specific histotripsy treatment planning.

In the present study, mechanical testing results demonstrated that cortical bone properties in normal bone specimens were slightly lower than previously reported values[67–70]. This may be due to unintended trabecular involvement in samples taken from the endocortical surface, given the limited tissue availability in the distal segments of the sampled long bones. For the tumor tissue, no comparable mechanical properties for OS tissue are available in the literature, but the reduced mechanical properties observed in the OS tumor tissue relative to the grossly normal bone in these data reinforces the observed phenomenon of compromised structural properties of OS tumor tissue even prior to histotripsy treatment. Post-yield trabecular specimen properties are in line with previously published literature values for all groups (UN, AN, AT) except UT; Kang et al. found the elastic modulus and ultimate load of a healthy canine humeral head, which several of the specimens in this study were excised from, to be 350+171 MPa and 225+74 N, respectively[71]. The large range in trabecular properties for UT specimens reported in this study implies a significant degree of structural and material heterogeneity, which is characteristic of OS tumor tissue[72–74]. Evaluation of the structural properties, namely BV/TV, of select trabecular UT specimens also revealed a wide range of values, some of which fall above those previously published in literature for grossly normal canine trabecular bone; BV/TV of canine trabecular bone has been shown to range from approximately 15 – 45% when sampled from lumbar spine and femoral anatomical locations[75–77]. The higher BV/TV values reported here may demonstrate OS-induced osteoblastic activity, leading to disruption of trabecular architecture and the formation of high-density areas of sclerosis, or unintended cortical involvement. Regarding anisotropy, significant differences in elastic modulus between loading directions were only observed within ablated tissue groups. These findings may imply that histotripsy contributes to a stiff-

ening effect in the primary loading direction; however, confounding factors such as donor demographics and small sample size cannot be excluded. Future studies should assess the mechanical properties of histotripsy-treated bone in multiple loading directions to determine whether histotripsy affects bone anisotropy and directional load dependence.

This study has important limitations that should be considered when interpreting findings. The clinical nature of this pilot study prevented complete control over key variables such as tissue donor characteristics (age, weight, sex, etc.), tumor characteristics, the anatomical location from which sample tissue was extracted, and sample size. Small and uneven group sizes may have limited statistical power and the generalizability of results, highlighting the need for larger, more balanced cohorts. Variations in donor characteristics and tumor location may have also contributed to differences in baseline mechanical properties; future work should consider stratification by age, body weight, or tumor location to minimize these effects. Additionally, because patients remained under clinical care following standard-of-care amputation, matched contralateral limbs were not available for use as controls. As such, observed differences between groups may, in part, reflect these confounding factors. Trabecular bone architecture is also highly heterogeneous, making this type of tissue difficult to mechanically analyze without accompanying robust, density-calibrated image analysis[78–80]. To address these limitations, controlled, dose-dependent studies are needed to evaluate the biomechanical effects of histotripsy on healthy and OS-affected tissue, establish treatement guidelines, and determine safe thresholds for ablation that preserve surrounding, healthy structures. Further characterizing the relationship between tumor heterogeneity and histotripsy dose is also imperative for ensuring complete tumor ablation and maximizing therapeutic safety and efficacy.

Histotripsy is currently being explored in combination with chemotherapy for liver tumors, such as colorectal liver metastases[81] and preclinical studies are investigating its integration with immunotherapy and chemotherapy across various cancer types[82,83]. Although these studies are not yet osteosarcoma-specific, they establish a precedent for histotripsy's poten-

tial as a multimodal therapy. As a neoadjuvant therapy, histotripsy could reduce tumor burden prior to surgery and improve surgical outcomes. As an adjuvant therapy, histotripsy could be applied to post-surgical tumor to ablate residual disease, potentially reducing local recurrence. In combination with immunotherapy, histotripsy may enhance immune activation through the release of tumor antigens, supporting its own anti-tumor abscopal response[84].

3.6 Conclusions

In this study, the effects of histotripsy on the biomechanical properties of tumor tissue and grossly normal bone were evaluated, demonstrating its potential as a safe, bone-sparing treatment option for OS. Both trabecular and cortical bone specimens were mechanically tested to failure via compression and 3-pt bending, respectively. No significant differences were found in mechanical properties between ablated and unablated normal bone groups, supporting the hypothesis that clinical doses of histotripsy do not detrimentally affect the biomechanical properties of normal cortical or trabecular bone. Additionally, no significant differences were found in mechanical properties between ablated and unablated tumor groups, indicating that histotripsy treatment does not further compromise the biomechanical integrity of OS tumor-affected bone. Trabecular, unablated tumor specimens showed a wide range in trabecular density and mechanical properties, highlighting the heterogeneity of OS tumors and the difficulties that may arise while attempting to treat a whole tumor volume. Ultimately, the results of the current work will aid in the development and advancement of histotripsy as an effective, non-invasive, bone-sparing, and patient-specific treatment option for clinical OS.

3.7 Acknowledgements

The authors gratefully acknowledge the support of the National Institutes of Health (NIH) [R01CA289288], the Veterinary Memorial Foundation, the Focused Ultrasound Foundation, and the Virginia Tech COE EFO-O Program. We also extend our sincere gratitude to the canine patients and their owners, whose participation made this research possible. Dr. Caitlyn Collins is an iTHRIV Scholar. The iTHRIV Scholars Program is supported in part by the National Center for Advancing Translational Sciences (NCATS) of the NIH under Award Numbers UL1TR003015 and KL2TR003016. Lauren Ruger has an ongoing consulting relationship with Theraclion, and Eli Vlaisavljevich has an ongoing research partnership and financial relationship with HistoSonics, Inc.

Works Cited

(1) Achari, P. F.; Vickers, E.; Ruger, L.; Vlaisavljevich, E.; Tuohy, J.; Collins, C. J. *Front. Vet. Sci.* **2026**, *12*.

(2) Huang, X.; Zhao, J.; Bai, J.; Shen, H.; Zhang, B.; Deng, L.; Sun, C.; Liu, Y.; Zhang, J.; Zheng, J. *J. Bone Oncol.* **2019**, *16*, 100230.

(3) Lindsey, B. A.; Markel, J. E.; Kleinerman, E. S. *Junw* **2017**.

(4) Luu, A. K.; Viloria-Petit, A. M. *Int. J. Mol. Sci.* **2020**, *21*.

(5) Luu, A. K.; Wood, G. A.; Viloria-Petit, A. M. *Front Vet Sci* **2021**, *8*, 734965.

(6) Xu, M.; Wang, Z.; Yu, X.-C.; Lin, J.-H.; Hu, Y.-C. *Orthop. Surg.* **2020**, *12*, 1021–1029.

(7) Tiwari, A. *J. Clin. Orthop. Trauma* **2012**, *3*, 4–9.

(8) Jacques, C.; Renema, N.; Lezot, F.; Ory, B.; Walkley, C. R.; Grigoriadis, A. E.; Heymann, D. *J Bone Oncol* **2018**, *12*, 7–13.

(9) Wong, K. C.; Kumta, S. M.; Sze, K. Y.; Wong, C. M. *Comput. Aided Surg.* **2012**, *17*, 284–293.

(10) Detenbeck, L. C.; Jowsey, J. *Clin. Orthop. Relat. Res.* **1969**, *65*, 76.

(11) Snow, G. R.; Cook, M. A.; Anderson, C. *Calcif. Tissue Int.* **1984**, *36*, 586–590.

(12) Kuhn, J. L.; Goldstein, S. A.; Ciarelli, M. J.; Matthews, L. S. *J. Biomech.* **1989**, *22*, 95–107.

(13) Vahey, J. W.; Lewis, J. L.; Vanderby Jr, R. *J. Biomech.* **1987**, *20*, 29–33.

(14) Mason, N. J. *Adv. Exp. Med. Biol.* **2020**, *1258*, 199–221.

(15) Lazarides, A. L.; Putterman, A. B.; Eward, W. C.; Eward, C. *Osteosarcoma–Biology, behavior and mechanisms* **2017**.

(16) Makielski, K. M.; Mills, L. J.; Sarver, A. L.; Henson, M. S.; Spector, L. G.; Naik, S.; Modiano, J. F. *Vet. Sci. China* **2019**, *6*.

(17) Szewczyk, M.; Lechowski, R.; Zabielska, K. *Vet. Res. Commun.* **2015**, *39*, 61–67.

(18) Mitchell, K. E.; Boston, S. E.; Kung, M.; Dry, S.; Straw, R. C.; Ehrhart, N. P.; Ryan, S. D. *Vet. Surg.* **2016**, *45*, 36–43.

(19) Greillier, P.; Bawiec, C.; Bessière, F.; Lafon, C. *IRBM* **2018**, *39*, 227–235.

(20) Khokhlova, V. A.; Fowlkes, J. B.; Roberts, W. W.; Schade, G. R.; Xu, Z.; Khokhlova, T. D.; Hall, T. L.; Maxwell, A. D.; Wang, Y.-N.; Cain, C. A. *Int. J. Hyperthermia* **2015**, *31*, 145–162.

(21) Dubinsky, T. J.; Khokhlova, T. D.; Khokhlova, V.; Schade, G. R. *J. Ultrasound Med.* **2020**, *39*, 1057–1067.

(22) Ruger, L. N.; Hay, A. N.; Vickers, E. R.; Coutermarsh-Ott, S. L.; Gannon, J. M.; Covell, H. S.; Daniel, G. B.; Laeseke, P. F.; Ziemlewicz, T. J.; Kierski, K. R.; Ciepluch, B. J.; Vlaisavljevich, E.; Tuohy, J. L. *Cancers (Basel)* **2023**, *15*, 741.

(23) Xu, Z.; Hall, T. L.; Vlaisavljevich, E.; Lee Jr, F. T. *Int. J. Hyperthermia* **2021**, *38*, 561–575.

(24) Vlaisavljevich, E.; Owens, G.; Lundt, J.; Teofilovic, D.; Ives, K.; Duryea, A.; Bertolina, J.; Welling, T. H.; Xu, Z. *Ultrasound Med. Biol.* **2017**, *43*, 1237–1251.

(25) Vidal-Jove, J.; Serres, X.; Vlaisavljevich, E.; Cannata, J.; Duryea, A.; Miller, R.; Merino, X.; Velat, M.; Kam, Y.; Bolduan, R.; Amaral, J.; Hall, T.; Xu, Z.; Lee Jr, F. T.; Ziemlewicz, T. J. *Int. J. Hyperthermia* **2022**, *39*, 1115–1123.

(26) Worlikar, T.; Mendiratta-Lala, M.; Vlaisavljevich, E.; Hubbard, R.; Shi, J.; Hall, T. L.; Cho, C. S.; Lee, F. T.; Greve, J.; Xu, Z. *BME Front.* **2020**, *2020*, 1–14.

(27) Schade, G. R.; Keller, J.; Ives, K.; Cheng, X.; Rosol, T. J.; Keller, E.; Roberts, W. W. *J. Urol.* **2012**, *188*, 1957–1964.

(28) Schade, G. R.; Wang, Y.-N.; D'Andrea, S.; Hwang, J. H.; Liles, W. C.; Khokhlova, T. D. *Ultrasound Med. Biol.* **2019**, *45*, 137–147.

(29) Hendricks, A. D.; Howell, J.; Schmieley, R.; Kozlov, S.; Simon, A.; Coutermarsh-Ott, S. L.; Vlaisavljevich, E.; Allen, I. C. *J. Immunol.* **2019**, *202*, 194.30–194.30.

(30) Duclos, S.; Golin, A.; Fox, A.; Chaudhary, N.; Camelo-Piragua, S.; Pandey, A.; Xu, Z. *Int. J. Hyperthermia* **2023**, *40*, 2237218.

(31) Sukovich, J. R.; Cain, C. A.; Pandey, A. S.; Chaudhary, N.; Camelo-Piragua, S.; Allen, S. P.; Hall, T. L.; Snell, J.; Xu, Z.; Cannata, J. M.; Teofilovic, D.; Bertolina, J. A.; Kassell, N.; Xu, Z. *J. Neurosurg.* **2019**, *131*, 1331–1338.

(32) Gannon, J. et al. *Int. J. Hyperthermia* **2023**, *40*, 2247187.

(33) Hendricks-Wenger, A.; Sereno, J.; Gannon, J.; Zeher, A.; Brock, R. M.; Beitel-White, N.; Simon, A.; Davalos, R. V.; Coutermarsh-Ott, S.; Vlaisavljevich, E.; Allen, I. C. *IEEE Trans. Ultrason. Ferroelectr. Freq. Control* **2021**, *68*, 2987–3000.

(34) Ruger, L.; Yang, E.; Gannon, J.; Sheppard, H.; Coutermarsh-Ott, S.; Ziemlewicz, T. J.; Dervisis, N.; Allen, I. C.; Daniel, G. B.; Tuohy, J.; Vlaisavljevich, E.; Klahn, S. *IEEE Trans. Biomed. Eng.* **2023**, *70*, 768–779.

(35) Arnold, L.; Hendricks-Wenger, A.; Coutermarsh-Ott, S.; Gannon, J.; Hay, A. N.; Dervisis, N.; Klahn, S.; Allen, I. C.; Tuohy, J.; Vlaisavljevich, E. *Ultrasound Med. Biol.* **2021**, *47*, 3435–3446.

(36) Ruger, L. N.; Hay, A. N.; Gannon, J. M.; Sheppard, H. O.; Coutermarsh-Ott, S. L.; Daniel, G. B.; Kierski, K. R.; Ciepluch, B. J.; Vlaisavljevich, E.; Tuohy, J. L. *IEEE Trans. Biomed. Eng.* **2022**, *PP*.

(37) Vlaisavljevich, E.; Kim, Y.; Allen, S.; Owens, G.; Pelletier, S.; Cain, C.; Ives, K.; Xu, Z. *Ultrasound Med. Biol.* **2013**, *39*, 1398–1409.

(38) Lake, A. M.; Xu, Z.; Wilkinson, J. E.; Cain, C. A.; Roberts, W. W. *J. Urol.* **2008**, *179*, 1150–1154.

(39) Prudowsky, Z. D.; Yustein, J. T. *Cancers (Basel)* **2020**, *13*, 83.

(40) Lee, R. K. L.; Chu, W. C. W.; Leung, J. H. Y.; Cheng, F. W. T.; Li, C. K. *Pediatr. Blood Cancer* **2013**, *60*, 1118–1121.

(41) Zhou, Y.; Lu, Q.; Xu, J.; Yan, R.; Zhu, J.; Xu, J.; Jiang, X.; Li, J.; Wu, F. *Oncotarget* **2017**, *8*, 73037–73049.

(42) Chandrasekar, C. R.; Grimer, R. J.; Carter, S. R.; Tillman, R. M.; Abudu, A.; Jeys, L. M.; Cheung, W. G. H.; Sharma, R. *ISRN Oncol.* **2012**, *2012*, 512389.

(43) Morgan, E. F.; Unnikrisnan, G. U.; Hussein, A. I. *Annu. Rev. Biomed. Eng.* **2018**, *20*, 119–143.

(44) Collins, C. J.; Andriotis, O. G.; Nedelkovski, V.; Frank, M.; Katsamenis, O. L.; Thurner, P. J. In *Encyclopedia of Biomedical Engineering: Volume 2*, Narayan, R., Ed.; Elsevier: 2019; Vol. 2, p 22.

(45) Romanus, B. *Acta Orthop. Scand. Suppl.* **1974**, *155*, 1–101.

(46) Longo, A. B.; Salmon, P. L.; Ward, W. E. *J. Orthop. Res.* **2017**, *35*, 1690–1698.

(47) Chattah, N. L.-T.; Sharir, A.; Weiner, S.; Shahar, R. *Bone* **2009**, *45*, 84–90.

(48) Wagner, D. W.; Lindsey, D. P.; Beaupre, G. S. *Bone* **2011**, *49*, 931–938.

(49) Mulder, L.; Koolstra, J. H.; den Toonder, J. M. J.; van Eijden, T. M. G. J. *Bone* **2007**, *41*, 256–265.

(50) Hogeboom, W. R.; Hoekstra, H. J.; Mooyaart, E. L.; Freling, N. J.; Veth, R. P.; Postma, A.; Schraffordt Kopps, H. *Eur. J. Surg. Oncol.* **1992**, *18*, 67–72.

(51) Voss, E. E.; Goode, R. D.; Cook, J. L.; Crist, B. D. *Mo. Med.* **2022**, *119*, 261–265.

(52) Zimmer, W. D.; Berquist, T. H.; McLeod, R. A.; Sim, F. H.; Pritchard, D. J.; Shives, T. C.; Wold, L. E.; May, G. R. *Clin. Orthop. Relat. Res.* **1986**, 289–299.

(53) Dowling, N. E.; Kampe, S. L.; Kral, M. V., *Mechanical behavior of materials*, 5th ed.; Pearson: Upper Saddle River, NJ, 2018.

(54) Simpson, A. M.; Ludwig, L. L.; Newman, S. J.; Bergman, P. J.; Hottinger, H. A.; Patnaik, A. K. *J. Am. Vet. Med. Assoc.* **2004**, *224*, 236–240.

(55) Farese, J. P.; Bacon, N. J.; Liptak, J. M.; Kow, K. In *Veterinary Surgery: Small Animal*, Tobias, K. M., Johnston, S. A., Eds.; Elsevier: St. Louis, 2012, pp 304–324.

(56) Meier, V.; Staudinger, C.; Radonic, S.; Besserer, J.; Schneider, U.; Walsh, L.; Rohrer Bley, C. *Vet. Comp. Oncol.* **2021**, *19*, 266–274.

(57) Özsoy, Ç.; Lafci, B.; Reiss, M.; Deán-Ben, X. L.; Razansky, D. *Photoacoustics* **2023**, *31*, 100508.

(58) Haar, G. T.; Coussios, C. *Int. J. Hyperthermia* **2007**, *23*, 89–104.

(59) Spałek, M. J. et al. *Cells* **2021**, *10*, 366.

(60) Emerzian, S. R., *Role of radiation treatment on bone strength and fracture risk [dissertation*, Berkeley, CA; University of California, 2021.

(61) Limirio, P. H. J. O.; Soares, P. B. F.; Emi, E. T. P.; Lopes, C. d. C. A.; Rocha, F. S.; Batista, J. D.; Rabelo, G. D.; Dechichi, P. *Radiat. Oncol.* **2019**, *14*, 15.

(62) Gonzalez, M. R.; Bedi, A.; Karczewski, D.; Lozano-Calderon, S. A. *Clin. Orthop. Relat. Res.* **2023**, *481*, 2433–2443.

(63) Abudu, A.; Sferopoulos, N. K.; Tillman et al., R. M. *J. Pediatr. Orthop.* **1997**, *17*, 277.

(64) Salunke, A. A.; Chen, Y.; Xi, C.; Puhaindran, M. *J. Cancer Res. Ther.* **2015**, *11*, 1043.

(65) Ntombela, P.; Ndou, W. *Journal of Orthopaedic Reports* **2025**, *4*, 100628.

(66) Rosenberg, Z. S.; Lev, S.; Schmahmann, S.; Steiner, G. C.; Beltran, J.; Present, D. *AJR Am. J. Roentgenol.* **1995**, *165*, 1209–1214.

(67) Kaneps, A. J.; Stover, S. M.; Lane, N. E. *Bone* **1997**, *21*, 419–423.

(68) Autefage, A.; Palierne, S.; Charron, C.; Swider, P. *Vet. J.* **2012**, *194*, 202–209.

(69) Sogawa, T.; Yamaguchi, F.; Misumi, K.; Fujiki, M. *J. Vet. Med. Sci.* **2024**, *86*, 325–332.

(70) Saha, S.; Martin, D. L.; Phillips, A. *Med. Biol. Eng. Comput.* **1977**, *15*, 72–74.

(71) Kang, Q.; An, Y. H.; Friedman, R. F. *J. Mater. Sci. Mater. Med.* **1998**, *9*, 263–267.

(72) Sun, Y.; Zhang, C.; Fang, Q.; Zhang, W.; Liu, W. *J. Transl. Med.* **2023**, *21*, 99.

(73) Schiavone, K.; Garnier, D.; Heymann, M.-F.; Heymann, D. *Adv. Exp. Med. Biol.* **2019**, *1139*, 187–200.

(74) Menshikh, K.; Banicevic, I.; Obradovic, B.; Rimondini, L. *Tissue Eng. Part B Rev.* **2023**.

(75) Sniekers, Y. H.; Intema, F.; Lafeber, F. P.; van Osch, G. J.; van Leeuwen, J. P.; Weinans, H.; Mastbergen, S. C. *BMC Musculoskelet. Disord.* **2008**, *9*, 20.

(76) Kostenko, E.; Pockevičius, A.; Maknickas, A. *Open Vet. J.* **2023**, *13*, 1–10.

(77) Kuroki, K.; Cook, C. R.; Cook, J. L. *Osteoarthritis Cartilage* **2011**, *19*, 1142–1149.

(78) Menshikh, K.; Banicevic, I.; Obradovic, B.; Rimondini, L. *Tissue Eng. Part B Rev.* **2024**, *30*, 217–229.

(79) Oftadeh, R.; Perez-Viloria, M.; Villa-Camacho, J. C.; Vaziri, A.; Nazarian, A. *J. Biomech. Eng.* **2015**, *137*, 0108021.

(80) Wu, D. Mechanical analyses of trabecular bone and its interaction with implants, https://uu.diva-portal.org/smash/get/diva2:1342155/FULLTEXT01.pdf, Accessed: 2024-5-6, 2019.

(81) Ziemlewicz, T. J. et al. *Ann. Surg.* **2025**.

(82) Imran, K. M.; Ganguly, A.; Paul, T.; Powar, M.; Vlaisavljevich, E.; Cho, C. S.; Allen, I. C. *Int. J. Hyperthermia* **2023**, *40*, 2244206.

(83) Worlikar, T.; Hall, T.; Zhang, M.; Mendiratta-Lala, M.; Green, M.; Cho, C. S.; Xu, Z. *Int. J. Hyperthermia* **2024**, *41*, 2297650.

(84) Qu, S.; Worlikar, T.; Felsted, A. E.; Ganguly, A.; Beems, M. V.; Hubbard, R.; Pepple, A. L.; Kevelin, A. A.; Garavaglia, H.; Dib, J.; Toma, M.; Huang, H.; Tsung, A.; Xu, Z.; Cho, C. S. *J Immunother Cancer* **2020**, *8*.

Chapter 4

Tissue-Selective Bone Tumor Ablation with Histotripsy Preserves Whole Bone Integrity in an Orthotopic Osteosarcoma Murine Model

The following work represents the first biomechanical assessment of histotripsy-treated OS tumor-bearing limbs, integrating μCT-based structural analysis and uniaxial compression testing of murine OS tumor-bearing and contralateral, healthy tibiae. The manuscript detailing the results of this study is currently in preparation.

4.1 Introduction

Osteosarcoma (OS) is a rare, aggressive bone cancer and the most common primary malignant bone tumor in children and young adults. OS typically arises near the growth plates of long bones during periods of rapid skeletal growth, with peak incidence between 10 and 24 years of age[1–3]. OS accounts for 0.2% of all cancers in humans with an incidence rate of 1.2/100,000 cases/year, hindering clinical therapeutic development and advancements in treatment strategies[4,5]. Survival rates have not improved in decades, largely due to the refractoriness of metastatic disease; approximately 15-20% of patients present with pulmonary

metastases at diagnosis, for whom long-term survival is around 20-30%[6]. Despite improved patient outcomes with a combination of surgical resection, chemotherapy, and radiation, prognosis for OS patients remains poor. These conventional therapies also carry significant risks; therapeutic doses of radiation have been shown to weaken bone and delay healing[7–9], while chemotherapy can reduce bone density and introduce systemic toxicities such as gonadotoxicity and cardiotoxicity[10,11]. Treatment ineligibility, local recurrence, implant failure, metastatic effects, and reduced limb function post-surgical resection also limit overall survival and quality of life[12–14]. These factors highlight the pressing need for safer, bone-sparing, treatment alternatives for OS.

OS tumors exhibit significant genetic instability and histological heterogeneity, characterized by mixed lesions containing sclerotic regions of excessive bone formation and lytic regions of bone resorption. The high level of genetic and phenotypic heterogeneity characteristic of OS underlies its aggressive behavior, including resistance to therapy, compromised bone integrity, and high metastatic potential[15–17]. OS typically originates in the medullary cavity and proliferates through cortical bone, where tumor-driven osteolysis and abnormal bone remodeling substantially increase the risk of pathological fracture[18,19]. Such fractures occur in approximately 10% of patients and are associated with reduced survival, fracture hematoma, and the spread of micrometastases.[3,20–22] Given that conventional therapies can exacerbate bone fragility, therapeutic strategies that effectively target tumor tissue while preserving bone structure and function are critical.

Histotripsy, a noninvasive focused ultrasound technique that mechanically ablates tissue through controlled acoustic cavitation, has emerged as a promising alternative to surgery and radiation-based therapies[23]. Advantages of histotripsy include precise destruction of targeted tissue without ionizing radiation and the potential to induce abscopal effects that may facilitate control of metastatic disease. Histotripsy has received FDA approval for the treatment of liver cancer[24–26] and is currently being investigated clinically for renal[27] and prostate[28] cancers, as well as preclinically for brain[29,30], breast[31], pancreatic[32,33], and soft

tissue sarcomas[34]. In these soft-tissue applications, histotripsy has demonstrated tissue selectivity, liquefying parenchymal tissue while preserving collagen-dense structures such as nerves, bile ducts, and blood vessels within the ablation zone[35–37]. This selectivity likely reflects differences in resistance to histotripsy-induced mechanical damage, whereby stiffer tissues experience reduced bubble-driven deformation and tougher tissues withstand higher cavitation-induced stresses, ultimately requiring a higher acoustic dose for tissue disruption[37,38]. However, whether these features extend to mineralized, load-bearing tissues such as bone remains largely unknown.

Although substantial progress has been made in characterizing human OS, clinically effective bone-sparing therapeutic strategies remain limited[39]. In preclinical and canine clinical comparative oncology models, histotripsy has been shown to effectively ablate OS tumor tissue while preserving surrounding, normal bone tissue at the histologic level.[36,40,41] In our recent study, we demonstrated that histotripsy selectively ablated tumor tissue while preserving the mechanical competence of adjacent bone in *ex vivo* canine OS-affected limbs, supporting its potential as a bone-sparing ablation modality[42]. Canine OS remains a valuable translational model due to its shared biological and clinical features with human OS, including disease presentation, response to treatment, and genetic complexity[43–45], However, studies in canine companions are constrained by cost, availability, and limited experiental control opportunities for ethical reasons, similar to the limitations of human clinical trials[46]. To enable controlled investigation of OS tumor burden and therapeutic outcomes, several murine OS models have been developed, including xenogeneic[47,48], syngeneic[49,50], and genetically engineered models[51,52]. To date, immunological studies have demonstrated histotripsy's ability to ablate OS tumor tissue and induce immunomodulatory responses post-ablation in heterotopic[53] and orthotopic[54] murine OS models. However, no studies have evaluated how histotripsy affects bone morphology or mechanical competence at the whole-bone level, outcomes that are clinically critical given the high fracture risk associated with OS.

Mechanical testing methods such as compression[55,56], 3- and 4-point bending[57], and nanoin-

dentation[58] are commonly used to assess the mechanical properties of murine whole bone. Structural properties including stiffness and failure load, derived from force-displacement curves, describe the bone's response to loading both pre- and post-yield. Since whole-bone mechanical properties are highly dependent on bone geometry, morphometric analysis provides critical context for such mechanical findings[59]. High-resolution imaging modalities such as micro-computed tomography (CT), the gold standard for assessing bone microarchitecture, enable evaluation of material and morphometric properties such as bone density, volume fraction, cortical thickness, and porosity[60–62]. Although histotripsy has been investigated in OS models, integrated CT and mechanical evaluation of its effects on tumor-bearing whole bone remains limited, leaving it unclear whether histotripsy ablation preserves strength and fracture resistance.

In this study, syngeneic C3H/HeJ mice, which have been validated for investigation of OS in prior studies[63,64], were used to model key aspects of human OS. Tumors were induced in the proximal tibia using the DLM8 murine OS cell line[50]. To assess the impact of histotripsy ablation on tumor-bearing and normal bone, specimens were evaluated using CT and uniaxial compression to quantify changes in bone morphology and structural integrity. This study represents the first integrated assessment of histotripsy's effects on bone strength and structure in an orthotopic OS murine model, providing critical insight into its safety and therapeutic potential for primary OS tumors.

4.2 Methods

Murine model and OS tumor induction: 4-6-week-old, female C3H/HeJ mice (strain #: 000659, n=23) were acquired by our small animal veterinary team at the Virginia-Maryland College of Veterinary Medicine under an approved institutional IACUC protocol (23-198). Mice were anesthetized with isoflurane and $1x10^6$ DLM8 OS cells, which display aggressive growth and

high metastatic potential to the lung[50], were orthotopically implanted via paratibial injection into the right tibia. Tumors were allowed to grow until the largest diameter reached an average of 7mm across all mice. Mice were provided unrestricted access to food and water throughout the study. Tumor growth was monitored 3x/week using caliper measurements in two perpendicular directions, and overall body condition and weight were monitored 3-5x/week. All experiments were conducted in accordance with the NIH Guide for the Care and Use of Laboratory Animals.

Histotripsy ablation: Mice were anesthetized with isoflurane, after which a 1MHz, 8-element small animal histotripsy transducer, described in previous studies[54,65], was used to deliver single-cycle pulses to an ellipsoidal volume within the tumor region at a pulse repetition frequency of 500Hz. Treatments were delivered at 500 pulses per point with a spacing of 1mm x 0.5mm x 0.5mm. Treatments aimed to achieve 50% ablation of the tumor volume. Histotripsy treatments were guided in real-time using a coaxially aligned linear ultrasound imaging probe (L18-10L30H-4, Telemed, Vilnius, Lithuania, EU). The pressure for each sample was determined by visualizing the cavitation cloud and gradually increasing the pressure at the focus until a consistent cloud was observed on real-time ultrasound imaging. Peak negative pressures were kept at 34.3 + 1.5 MPa. The transducer was coupled to a computer-controlled 3D positioning system driven by a custom MATLAB script (MATLAB 2017a, MathWorks, Portola Valley, CA, USA) and submerged in degassed water maintained at 37 ± 4 °C throughout treatment.

Tissue harvest and grouping: Mice were euthanized via CO2 inhalation with secondary cardiac puncture at one of four post-treatment time points to assess acute (3 and 7 days), intermediate (14 days) and chronic (21 days) effects (Figure 4.1), or when predefined endpoint criteria were reached (>20% body weight loss or tumor size > 1000mm^3). Each mouse contributed both tibias, enabling paired comparisons within animals. At 3, 7, and 14 days post-treatment, mice contributed paired unablated normal (UN) and ablated tumor-bearing (AT) limbs. At 14 and 21 days post-treatment, additional cohorts contributed paired ablated

normal (AN) and unablated tumor-bearing (UT) limbs, as well as paired UN and UT limbs.

Following harvest, the fibula was removed to eliminate segmentation ambiguity during CT analysis and to ensure consistent geometry during mechanical loading. Tibial length was measured using calipers (16.0 + 1.04mm). Specimens were wrapped in phosphate-buffered saline (PBS)-soaked gauze and stored at -20°C in sealed 2mL screw-cap microtubes prior to CT scanning and compression testing. All tibias underwent no more than two freeze-thaw cycles.

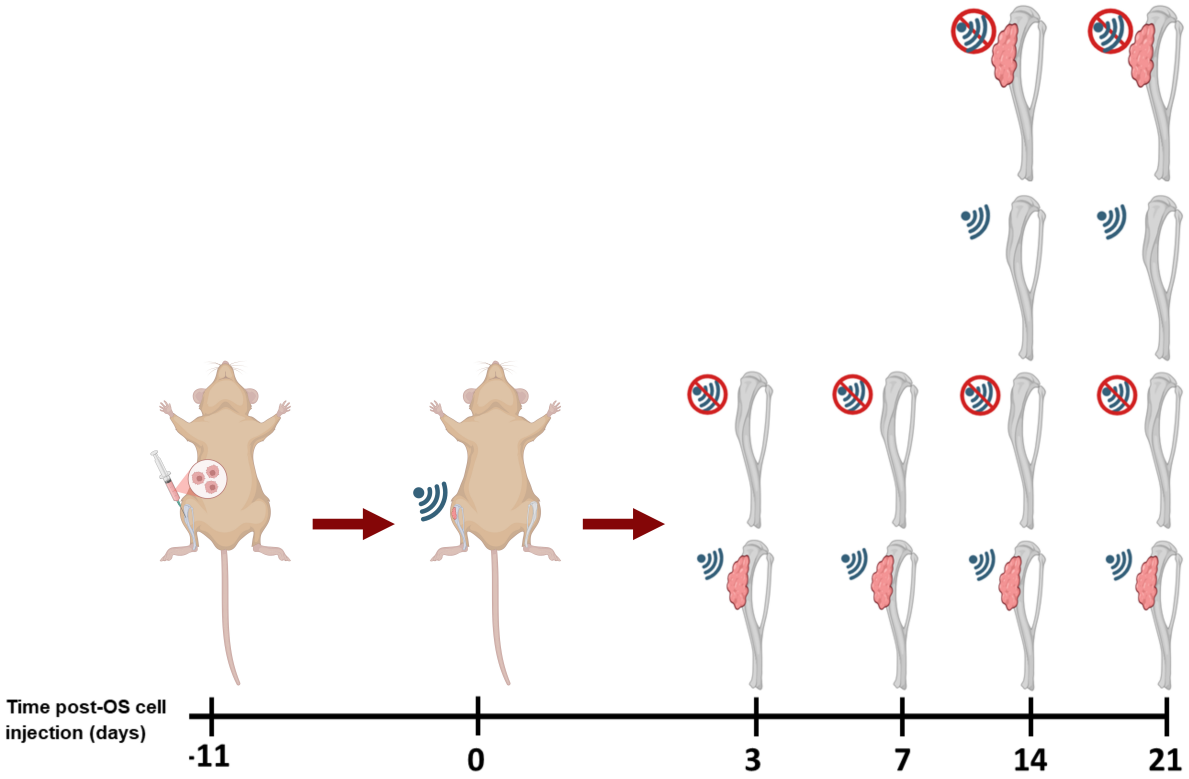

Figure 4.1: Timeline of OS tumor induction, histotripsy ablation, and endpoint tissue extraction at 3, 7, 14, and 21 days post-treatment for all ablated normal (AN), unablated normal (UN), ablated tumor-bearing (AT) and unablated tumor-bearing (UT) specimens. Treatment occurred 11 ± 2.4 days after para-tibial injection of DLM8 OS cells, therefore endpoints are reported at mean post-injection days. Only UN and AT specimens were collected at 3-7 days post-treatment, and all 4 groups were collected at 14-21 days post-treatment.

μCT imaging: All specimens were thawed and fully submerged in 2 mL screw-cap microtubes with PBS to prevent dehydration during scanning. CT scans were performed using a Nikon

VOXLS 40 C 450 system (Nikon Metrology, Tokyo, Japan) with the long axis of the tibia oriented vertically. Scans were acquired at an isotropic voxel resolution of 8.44μm (V=175 kV, I=160μA). After scanning, the bones were stored at -20°C in the PBS-filled microtubes until mechanical testing. 3D reconstructions of each specimen were generated from the scans using Inspect-X (Nikon Metrology, Tring, UK). Gaussian smoothing (3x3x3 kernel, standard deviation 0.8) was applied to reduce high-frequency noise.

Morphometric analysis: For cortical bone analysis, standard diaphyseal sites of 25%, 37%, and 75% of the bone's total length were chosen. Each tumor-affected bone was co-registered to the z-axis of its contralateral counterpart to ensure precise region of interest (ROI) matching using semi-automatic registration in Dragonfly (Object Research Systems, Montreal, QC, Canada), where an initial manual guess based on landmark features was refined automatically via sum of squared differences (SSD) optimization. For trabecular bone analysis, the ROI began 0.6mm distal to the proximal metaphyseal growth plate. ROIs were standardized across specimens with 119 slices, equivalent to a 1mm length in the longitudinal direction (Figure 4.2a). Binarized segmentation masks of the whole bone were obtained using Otsu thresholding[66] in Dragonfly (Object Research Systems, Montreal, QC, Canada), applied on a per-specimen basis. Segmentation of trabecular and cortical compartments was performed using Köhler's method[67] in the Bone Analysis module. Morphometric parameters including total volume (TV), trabecular bone volume fraction (Tb.BV/TV), trabecular thickness (Tb.Th), cortical porosity (Ct.Po; defined as 1-BV/TV), and cortical thickness (Ct.Th) were calculated to assess the impact of OS and treatment on bone structure.

Uniaxial compression testing: Prior to mechanical testing, specimens were thawed at room temperature (20°C) and hydrated in 1x PBS. The longitudinal axis of each tibia was vertically aligned using a reference standard, and 3mm of both ends were embedded in UV resin using a custom mold (Figure 4.2b). After potting, specimens were hydrated with PBS spray and placed between a compression platen (upper) and the mold (lower), which was rigidly fixed to the test frame (Figure 4.2c). Specimens were then preconditioned for 5

cycles at 0.042Hz between 1-4N to ensure sufficient contact with the sample. Immediately following preconditioning, the specimens were compressed to failure at a displacement rate of 0.03mm/s using an ElectroForce 3200 (TA Instruments, Eden Prairie, MN, USA). Force was measured using a 450N load cell, and displacement was recorded from the crosshead position. Failure was identified by a complete, visible fracture of the tibia accompanied by a sharp drop in load on the force-displacement curve. Mechanical properties including stiffness, ultimate load, and work to fracture were calculated from the resulting force-displacement curves to quantify the effects of histotripsy on the mechanical integrity of OS tumor-bearing and normal limbs. To account for variable specimen length and volume, work to fracture was normalized by an effective cortical volume (VOI cropped 3mm from each tibial end to account for potting material) of the mechanically loaded region to approximate toughness.

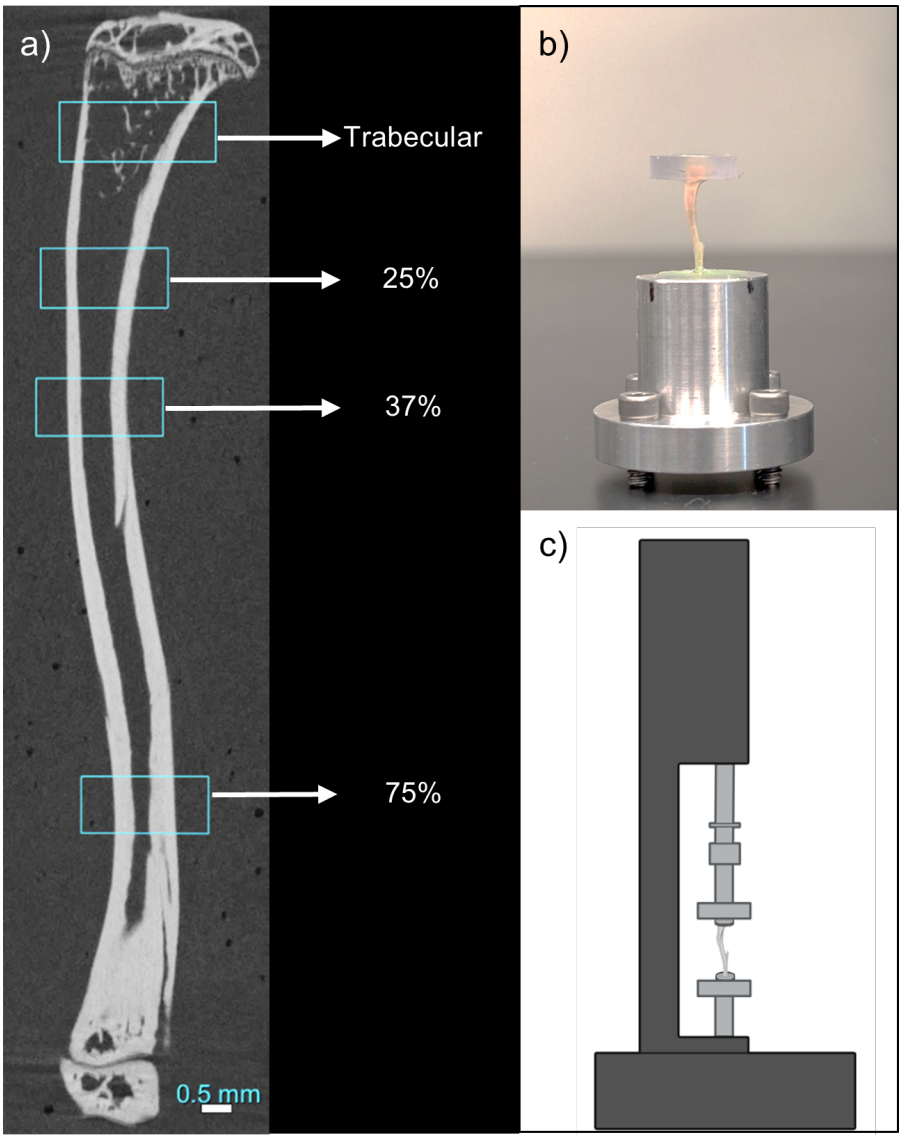

Figure 4.2: a) Sagittal CT slice of an unablated normal (UN) tibia with cortical and trabecular ROIs outlined in blue. b) Tibia setup in custom uniaxial compression jig. c) Pictorial representation of whole-bone compression

Statistical analysis: All statistical analyses were performed in Python 3.9 (statsmodels 0.13.2, scipy 1.7.3). Normality and homogeneity of variances assumptions were assessed using the Shapiro-Wilk and Levene's test, respectively. Data are reported as mean ± standard deviation for normally distrubuted data and as median (IQR) for nonparametric data. Statistical significance was set at $\alpha = 0.05$, and p-values were adjusted for multiple comparisons using the Holm-Bonferroni method unless otherwise specified.

To evaluate the early effects of histotripsy (3, 7, and 14 days post-ablation) on OS tumor-bearing bone, linear mixed-effects models (LMEM) were used to evaluate the interaction between time point and treatment group, with mouse included as a random effect to account for within-animal pairing. When interaction terms were not significant, the model was reduced and main effects were interpreted. Group differences within each time point were assessed using paired t-tests. Temporal changes within each group were analyzed using Welch's t-tests, since different mice were analyzed at each time point.

Cross-sectional comparisons at later endpoints (14 and 21 days post-ablation) were performed using Welch's ANOVA with Games-Howell post-hoc tests to accommodate small and unequal sample sizes. Associations between morphometric and mechanical parameters were evaluated using Spearman rank correlation (ρ). Coefficients of variation (CV=SD/mean) were calculated to quantify variability across groups and time points.

4.3 Results

A total of 22 mice completed the study, yielding 44 tibiae. One AT tibia collected 21 days post-treatment was excluded from further analysis due to insufficient AT sample size at that time point (n=1). Group assignments and final sample sizes for each time point are summarized in Table 4.1,4.2,4.3. Tumor ablation volume across all time points averaged 87.5 $\pm$ 12.7mm^3, achieving 50.9 $\pm$ 10.3% ablation for nearly all samples. To ensure consistent evaluation of the region most directly affected by tumor growth and histotripsy exposure, subsequent analyses focused on morphometric and mechanical outcomes within the 37% cortical ROI, closest to the OS tumor cell implantation site (Figure 4.3). Complete morphometric and mechanical data for all cortical ROIs can be found in Supplemental Information.

Table 4.1: Distribution of tibiae included in the mixed linear model by experimental group and post-ablation time point. Specimens included in this analysis are paired.

	Group	
Days post-ablation	UN (n=10)	AT (n=10)
3	3	3
7	3	3
14	4	4

Table 4.2: Distribution of tibiae included in the Welch's ANOVA analysis by experimental group and post-ablation time point. Specimens included in this analysis are unpaired.

	Group			
Days post-ablation	UN	AN	UT	AT
14	4	4	4	4

Table 4.3: Distribution of tibiae included in the Welch's t-test analysis by experimental group and post-ablation time point. Specimens included in this analysis are unpaired.

	Group		
Days post-ablation	UN	AN	UT
21	5	4	8

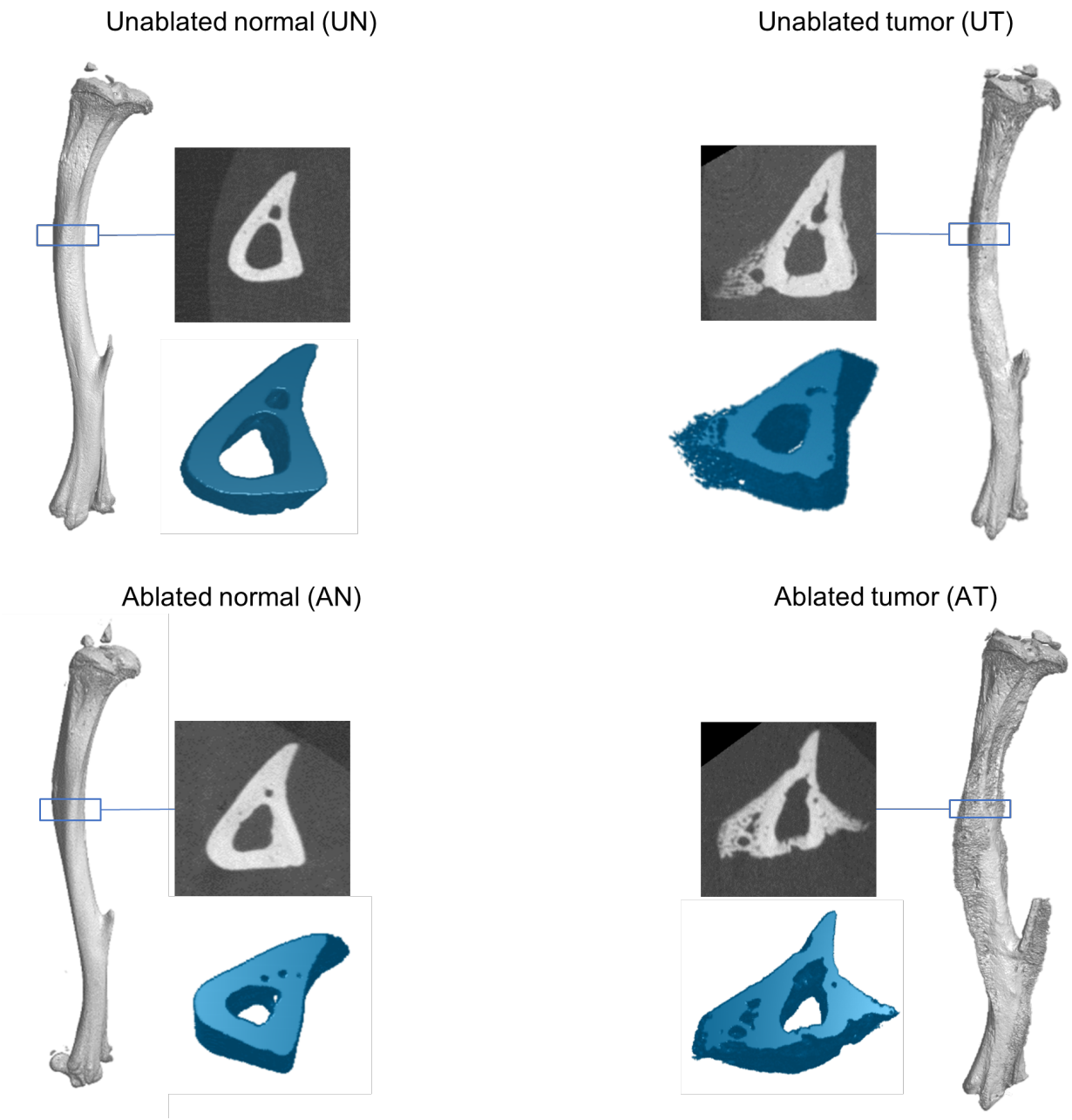

Figure 4.3: Axial CT images of the tibial cross section, highlighting changes in cortical porosity and thickness, with 3D renderings of the whole bone and selected ROIs located at 37% of total bone length distal to the proximal metaphysis (blue). Tumor-bearing bones have been mirrored for comparison.

Early time points post-histotripsy ablation exhibit altered cortical morphology but preserved mechanical behavior in tumor-bearing bone.

To determine the early effects of histotripsy on tumor-bearing bone, UN and AT specimens

at 3, 7, and 14 days post-ablation were analyzed. No significant interaction between time and group was detected, indicating that histotripsy did not alter the temporal progression of tumor- or bone-associated changes in structural or mechanical properties. However, a significant main effect of group was observed across all time points for all analyzed morphometric properties, with reduced Ct.Th and increased Ct.Po in AT specimens relative to UN controls ($p=0.002$ and 0.004, respectively). Ct.Ar was also greater in AT specimens ($p=0.044$), though variability was notably higher than in UN specimens (Figure 4.4). Tb.BV/TV was reduced in AT ($p=0.001$), consistent with localized trabecular bone loss associated with OS tumor presence. Post-hoc comparisons at individual time points did not reveal statistically significant group-wise differences.

Despite these morphometric differences, whole-bone mechanical properties, including ultimate load, stiffness, and toughness, were preserved across groups (Table 4.4). Although not statistically significant, AT specimens exhibited greater variability and a trend toward increased toughness compared to UN specimens.

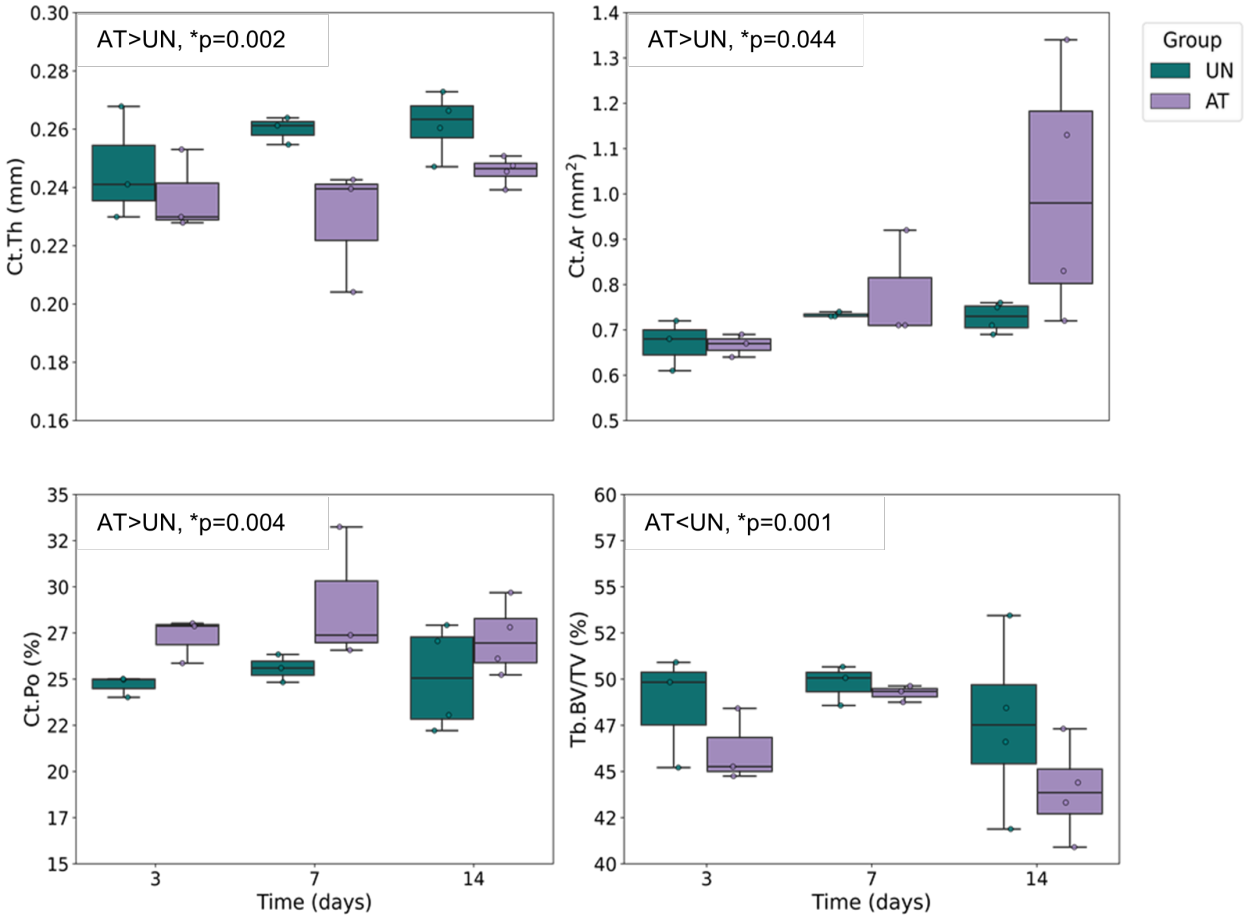

Figure 4.4: Selected morphometric data for UN and AT groups 3, 7, and 14 days post-ablation at the 37% cortical site and the trabecular site. All significant differences are interpreted based on LMEM main effects; post-hoc comparisons at individual time points did not yield significant differences.

Table 4.4: Whole bone mechanical properties for UN and AT groups 3, 7, and 14 days post-ablation. Data is reported as mean ± standard deviation or median (IQR)

Property / Group		Time point (days)		
		3	7	14
Ultimate load (N)	UN	40.7 ± 5.13	38.7 ± 7.06	35.6 ± 4.87
	AT	42.0 ± 10.6	53.5 ± 17.7	39.9 ± 13.4
Stiffness (N/mm)	UN	57.3 ± 3.62	71.4 ± 32.2	71.8 ± 15.0
	AT	68.3 ± 20.5	74.4 ± 24.7	53.9 ± 14.4
Toughness (MPa)	UN	1.63 ± 0.302	1.54 ± 0.179	0.873 ± 0.202
	AT	1.61 ± 0.534	2.00 ± 0.878	1.59 ± 0.848

Histotripsy induces a toughening effect and preserves mechanical integrity in normal bone despite morphometric changes 14 days post-ablation.

A cross-sectional analysis of all groups was performed 14 days post-ablation. Significant group-level differences were detected in Tb.BV/TV (p=0.007), Ct.Po (p=0.012), and Ct.Ar (p=0.003). Post-hoc analysis revealed Ct.Po was greater in AT than in AN, while Ct.Ar was significantly greater in UN than in AN specimens. Tb.BV/TV was higher in AN and UT compared to AT specimens (Figure 4.5).

Mechanical properties were largely preserved across groups (Table 4.5). Stiffness and ultimate load did not differ significantly, although normal bone specimens generally trended toward higher stiffness than those of their tumor-bearing counterparts. Overall differences in toughness were observed; however, post-hoc analyses did not identify significant differences, though AN trended toward higher toughness relative to UN (p=0.057).

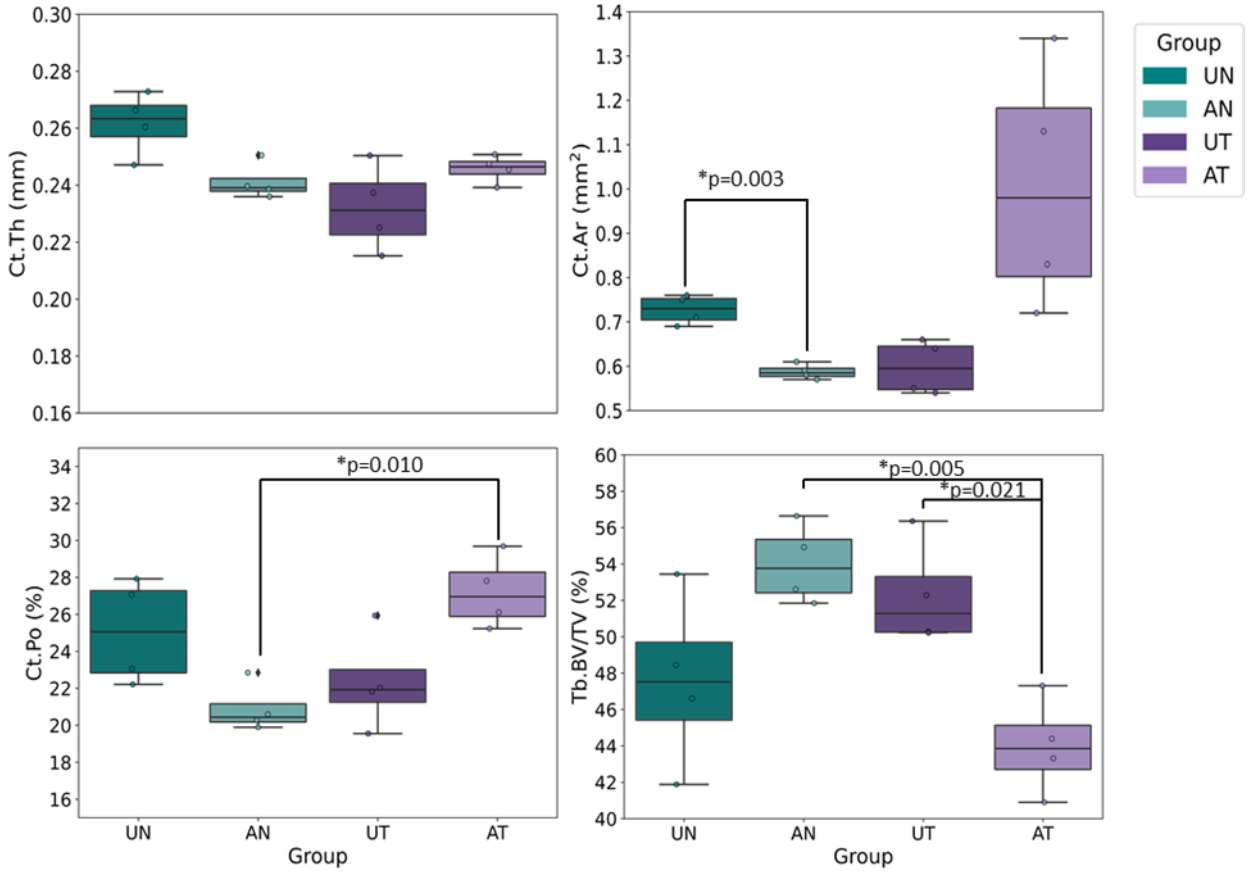

Figure 4.5: Selected morphometrics for UN, AN, UT, and AT groups 14 days post-ablation at the 37% cortical site and the trabecular site. * indicates statistical significance as determined by post-hoc analysis ($p<0.05$).

Table 4.5: Whole bone mechanical properties for UN, AN, UT, and AT groups 14 days post-ablation. Data is reported as mean ± standard deviation. * indicates statistical significance as determined by LMEM ($p<0.05$); post-hoc comparisons between groups did not yield significant differences.

Group	Ultimate load (N)	Stiffness (N/mm)	Toughness (MPa)
UN	35.6 ± 4.87	71.8 ± 15.0	0.873 ± 0.202
AN	54.9 ± 11.0	74.2 ± 17.1	3.14 ± 1.02
UT	43.3 ± 11.0	58.2 ± 12.5	2.44 ± 1.28
AT	39.9 ± 13.4	53.9 ± 14.4	1.59 ± 0.848
(p)	0.116	0.304	0.027*

Distinct chronic effects of tumor burden and histotripsy ablation on normal bone 21 days post-ablation.

To investigate the chronic effects of histotripsy ablation on normal bone, differences in properties between UN and AN tibiae 21 days post-ablation were analyzed. Histotripsy induced changes in cortical morphology in normal bone. Ct.Po and Ct.Ar were significantly lower in AN specimens compared to UN controls ($p=0.003$ and 0.002, respectively). Ct.Th trended higher in AN specimens ($p=0.186$, Figure 4.6). Tb.BV/TV did not differ between UN and AN groups. Whole-bone stiffness and ultimate load were preserved, while toughness was significantly greater in AN specimens ($p=0.037$, Table 4.6).

The late-stage impact of tumor burden on normal bone was also evaluated in UN and UT tibiae 21 days post-ablation. Tumor burden alone resulted in reduced Ct.Th in UT tibias relative to UN controls ($p=0.037$). However, no differences were observed in Ct.Po, Tb.BV/TV, or whole-bone mechanical properties, however, indicating that tumor-associated cortical thinning did not translate into measurable changes in structural strength within the assessed region.

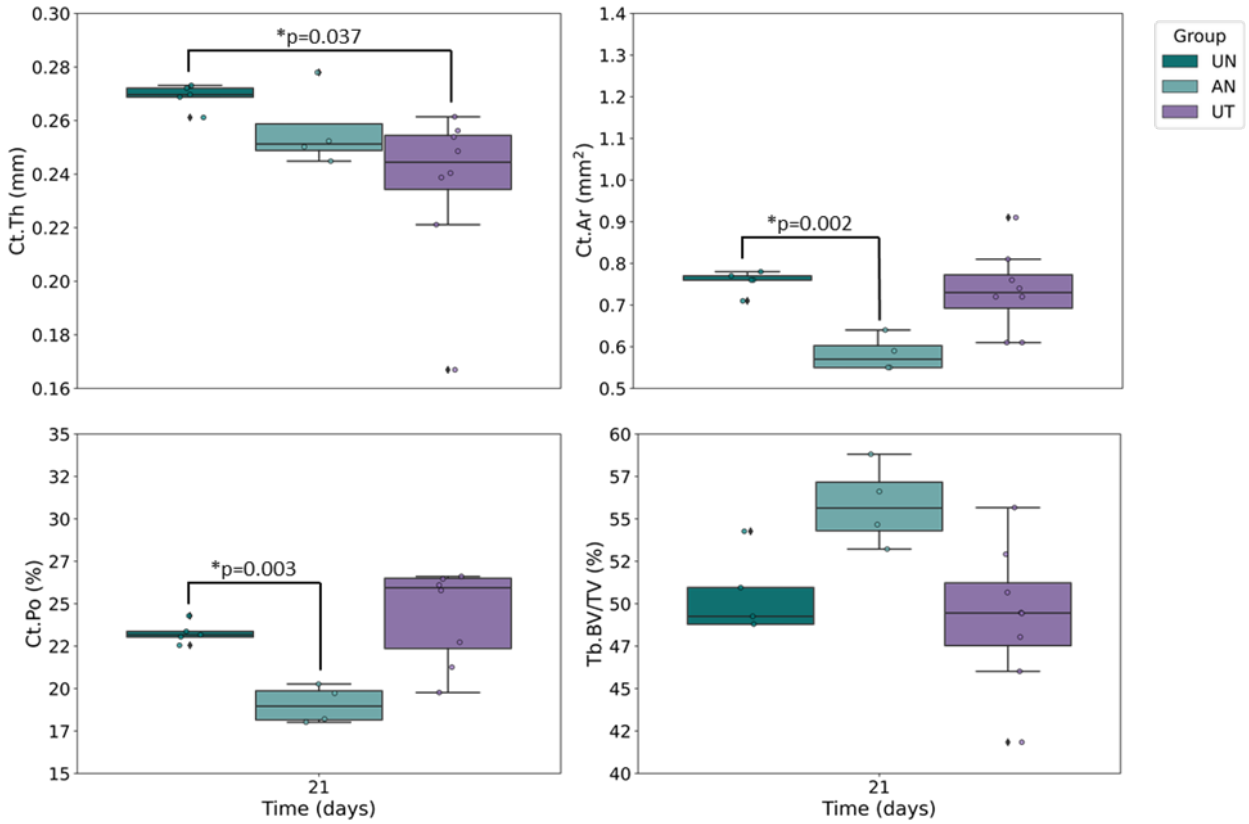

Figure 4.6: Selected morphometrics for UN, AN, and UT groups 21 days post-ablation at the 37% cortical site and the trabecular site. * indicates statistical significance as determined by post-hoc analysis ($p<0.05$).

Table 4.6: Whole bone mechanical properties of UN, AN, and UT groups 21 days post-ablation. Data is reported as mean ± standard deviation or median (IQR).

Group	Ultimate load (N)	Stiffness (N/mm)	Toughness (MPa)
UN (n=5)	44.4 ± 9.38	66.9 ± 18.8	1.51 ± 0.548
AN (n=4)	47.6 ± 6.30	60.3 (5.48)	2.49 ± 0.492
UT (n=4)	43.1 ± 10.7	74.3 ± 21.9	1.99 ± 0.866

Associations between bone morphology, mechanical properties, and variability

Significant albeit weak Spearman rank correlations (ρ) were observed between morphometric and mechanical parameters. Positive correlations were found between toughness and Tb.BV/TV, as well as between ultimate load and Tb.BV/TV. A negative correlation was found between toughness and Ct.Po (Figure 4.7).

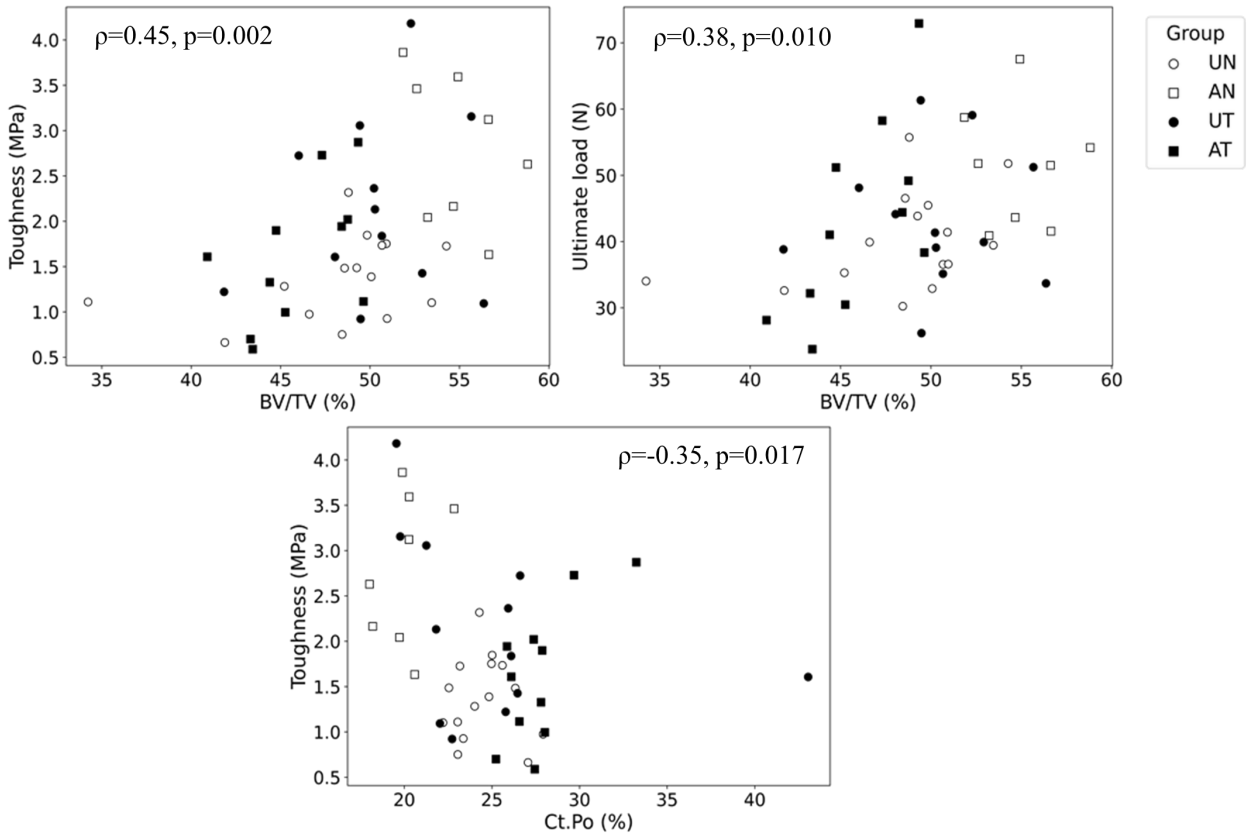

Figure 4.7: Spearman rank correlations between morphometric and whole-bone mechanical properties ($p<0.05$). Scatterplots show relationships between a) toughness and Tb.BV/TV, b) ultimate load and Tb.BV/TV, and c) toughness and Ct.Po.

Morphometric parameters exhibited relatively low variability across all groups and time points (mean CV: 7.3%), with the lowest variability observed in normal tibiae (UN and AN; 0.8-16%). Tumor-bearing tibiae demonstrated greater morphometric variability (UT and AT; 0.9-28%). Mechanical properties exhibited substantially higher variability overall (mean CV: 27%), particularly in tumor-bearing groups, where coefficients of variation for ultimate load, stiffness, and toughness often exceeded 30-50%.

4.4 Discussion

This study investigated the effects of histotripsy on bone morphology and whole-bone mechanical behavior in a murine OS model. By combining CT-derived morphometric parameters with uniaxial compression testing, this work demonstrated that histotripsy induces structural adaptations in OS tumor-bearing bone, but preserves the mechanical integrity of both normal and tumor-bearing tibiae. CT-derived morphometrics at the site 75% distal to the proximal tibial end showed minimal variation across all groups and time points, indicating that both histotripsy treatment and OS-associated structural changes were localized near the tumor implantation region. Morphometric trends at the site 25% distal to the proximal tibial end closely mirrored those observed at the 37% site, likely consistent with their proximity to this region.

Following histotripsy ablation, stiffness and ultimate load were largely preserved while toughness increased, indicating that treated tibiae absorbed more energy before failure without compromising strength. Similar preservation of strength despite structural changes has been reported in previous studies, where compensatory geometric and microstructural adaptations can maintain load-bearing capacity despite localized degradation of material properties[68,69] Notably, this increase in toughness was not observed in unablated tumor-bearing limbs, suggesting an association between treatment and altered mechanical behavior. These findings are consistent with a more ductile mechanical response and periosteal remodeling following treatment; however, the relative contributions of histotripsy vs. tumor-driven remodeling cannot be fully distinguished in this model, particularly in ex vivo specimens harvested at single time points[70,71].

Treated tumor-bearing limbs demonstrated morphometric patterns distinct from untreated tumor-bearing limbs while maintaining mechanical behavior. Compared to unablated normal bone, both unablated and ablated tumor-bearing limbs exhibited reduced cortical thickness, consistent with OS tumor-driven endosteal resorption[70]. However, while UT specimens

showed decreased cortical area and preserved porosity, AT specimens displayed increased cortical area and elevated porosity. These changes are consistent with active remodeling processes, including endocortical resorption and periosteal expansion[72,73]; Note that this bone expansion may also reflect tumor-induced sclerosis. Overall, the measured increases in total volume and cross-sectional area in the ablated tumor-bearing limbs may have helped preserve stiffness and failure load, despite reduced cortical thickness in the treated and untreated tumor-bearing limbs.

In normal bone, histotripsy ablation induced bone remodeling without compromising structural integrity. AN specimens often exhibited higher trabecular bone volume fraction and ultimate load than other groups. This positive correlation between trabecular bone volume fraction and ultimate load is well-established and reinforces trabecular bone volume fraction as a reliable indicator of bone strength in a murine model[74,75]. AN tibiae also showed reduced cortical porosity, thickness, and area relative to UN, suggesting that histotripsy ablation of normal bone may trigger a resorptive remodeling response that did not detrimentally alter structural integrity. In 4-6 week-old mice, early bone remodeling is dominated by periosteal deposition rather than resorption, which is brief[76]. Since AN tibiae were collected 14-21 days after treatment, any initial resorption caused by histotripsy ablation may have already been repaired, leaving a net reduction in cortical porosity. Such structural changes likely contributed to the observed preservation and slight though nonsignificant increases in stiffness and ultimate load in AN specimens.

The preservation of stiffness and load-bearing capacity in treated specimens despite cortical thinning and elevated porosity reflects the geometric advantage of periosteal deposition; as long bones grow, endocortical resorption and periosteal deposition expand the outer diameter of the cortex, shifting cortical bone radially outward. Bending resistance increases with distance from the neutral axis, therefore even modest periosteal expansion can enhance whole-bone strength[77,78]. Experimental studies in murine tibial loading models involving bone in both healthy and diseased states have similarly demonstrated that periosteal appo-

sition and geometric adaptations play a key role in maintaining or enhancing whole-bone strength despite accompanying endocortical resorption[57,79] Together, these results suggest that histotripsy mitigates structural deterioration while promoting adaptive bone remodeling that maintains whole bone strength.

Spearman correlation analysis supported the expected relationships between bone morphology and mechanical integrity. Toughness and failure load were positively correlated with trabecular BV/TV (ρ=0.45 and 0.38, respectively), indicating that denser trabecular architecture contributes to improved load-bearing capacity and energy absorption[75,80]. In contrast, toughness was negatively correlated with cortical porosity (ρ=-0.35), consistent with prior reports demonstrating that increased porosity compromises bone's capacity to deform without fracturing[77,78]. These relationships are consistent with prior studies demonstrating that trabecular bone volume fraction and cortical porosity are among the strongest predictors of whole-bone mechanical behavior across both preclinical and clinical populations[81–83]

Variability in the relationships between bone structure and behavior was greatest in tumor-bearing limbs, particularly for mechanical outcomes, likely reflecting the combined effects of tumor invasion, localized treatment-induced remodeling, and geometry-dependent loading during compression, which may obscure subtle mechanical differences despite measurable changes in bone morphology. Similar variability has been reported in other preclinical OS models, where tumor heterogeneity and aberrant remodeling contribute to high variability in mechanical outcomes[84,85] In contrast, morphometric measures exhibited lower variability across groups, suggesting that microarchitectural changes were more consistently captured than whole-bone mechanical responses. Normal groups exhibited lower variability regarding all measured parameters, indicating more uniform microarchitecture and mechanical behavior as is expected in normal bone as compared to tumor-affected bone.

This study has important limitations that should be considered when interpreting findings. Sample sizes were small, with an average of 3-4 mice per group per time point, which may

have contributed to the observed variability and low statistical power. However, consistent imaging and repeatable mechanical testing protocols were employed to improve reliability and repeatability of experimental results. Not all groups were represented at every time point, making direct, time-series comparisons across all groups challenging; nevertheless, cross-sectional trends were analyzed for all groups, providing meaningful insights into treatment and disease effects. The phenotypic heterogeneity exhibited by OS tumors may have also varied across mice, potentially masking subtle effects of histotripsy ablation. The natural curvature and irregular geometry of the murine tibia further complicates interpretation of whole-bone compression outcomes; uniaxial loading of long bones produces a combination of axial compression and mediolateral bending effects, with compressive strains concentrated on the posterior-lateral surface and tensile strains on the anterior-medial surface[79,86] To mitigate geometry-dependent variability, all bones were oriented consistently relative to the test frame, and preconditioning cycles were applied to ensure stable contact and reproducible loading. Despite these measures, mechanical outcomes remained inherently variable (11-63%) across groups and time points, reflecting biological and geometric complexity.

Future studies should aim to increase sample sizes, standardize groups across time points, and incorporate in vivo, longitudinal imaging to capture dynamic changes in bone morphology and mechanics. Further investigating the relationship between OS tumor heterogeneity, histotripsy dose, and bone response is critical for optimizing treatment parameters. Incorporating image-based finite element models could further link morphometric changes to whole-bone mechanical behavior and provide additional insight into the effects of histotripsy on bone quality and structure. Additional mechanical testing modalities, such as torsion or three-point bending, may also be considered in future studies to more comprehensively characterize the mechanical properties and loading response of tumor-bearing bones.

4.5 Conclusions

The aim of this study was to evaluate histotripsy as a potential noninvasive treatment option for osteosarcoma. Results demonstrate that histotripsy preserves whole-bone mechanical strength while enhancing energy absorption, suggesting stimulation of adaptive bone remodeling. Morphometric analyses further support this notion, showing evidence of both resorption and periosteal deposition in treated tumor-bearing and normal tibiae. Together, these findings provide foundational evidence that histotripsy can mitigate tumor-induced osteolysis without compromising structural integrity, highlighting its potential as an effective, non-invasive, limb-sparing therapeutic strategy for clinical OS.

4.6 Acknowledgments

The authors gratefully acknowledge the support of the National Institutes of Health (NIH) [R01CA289288], the Veterinary Memorial Fund at Virginia Tech, the Focused Ultrasound Foundation, and the Virginia Tech COE EFO-O Program. Elliana Vickers was supported by a Ruth L. Kirschstein Predoctoral Individual National Research Service Award from the National Cancer Institute [1F31CA294976-01] for the duration of this work. Lauren Ruger has an ongoing consulting relationship with Theraclion. Eli Vlaisavljevich is a cofounder and stockholder of Sound Blade Medical.

Works Cited

(1) Nie, Z.; Peng, H. *Oncol. Lett.* **2018**, *16*, 6502–6514.

(2) Sugalski, A. J.; Jiwani, A.; Ketchum, N. S.; Cornell, J.; Williams, R.; Heim-Hall, J.; Hung, J. Y.; Langevin, A.-M. *J. Pediatr. Hematol. Oncol.* **2014**, *36*, e353–8.

(3) Greenwood, A. C.; Arora, R. D.; Shaikh, H. In *StatPearls*; StatPearls Publishing: Treasure Island (FL), 2025.

(4) Lindsey, B. A.; Markel, J. E.; Kleinerman, E. S. *Rheumatol Ther* **2017**, *4*, 25–43.

(5) Brosa, M.; García del Muro, X.; Mora, J.; Villacampa, A.; Pozo-Rubio, T.; Cubells, L.; Montoto, C. *Expert Rev. Pharmacoecon. Outcomes Res.* **2015**, *15*, 331–340.

(6) Meazza, C.; Scanagatta, P. *Expert Rev. Anticancer Ther.* **2016**, *16*, 543–556.

(7) Spałek, M. J. et al. *Cells* **2021**, *10*, 366.

(8) Emerzian, S. R., *Role of radiation treatment on bone strength and fracture risk [dissertation*, Berkeley, CA; University of California, 2021.

(9) Limirio, P. H. J. O.; Soares, P. B. F.; Emi, E. T. P.; Lopes, C. d. C. A.; Rocha, F. S.; Batista, J. D.; Rabelo, G. D.; Dechichi, P. *Radiat. Oncol.* **2019**, *14*, 15.

(10) Ghosh, J.; Bajpai, J. *Pediatr. Hematol. Oncol. J.* **2017**, *2*, 41–47.

(11) Zhu, N.; Ni, H.; Guo, S.; Shen, Y.-Q.; Chen, Q. *Cancer Treat. Rev.* **2024**, *130*, 102828.

(12) Taran, S. J.; Taran, R.; Malipatil, N. B. *Indian J. Med. Paediatr. Oncol.* **2017**, *38*, 33–43.

(13) Tiwari, A. *J. Clin. Orthop. Trauma* **2012**, *3*, 4–9.

(14) Bläsius, F.; Delbrück, H.; Hildebrand, F.; Hofmann, U. K. *Cancers (Basel)* **2022**, *14*, 2694.

(15) Sun, Y.; Zhang, C.; Fang, Q.; Zhang, W.; Liu, W. *J. Transl. Med.* **2023**, *21*, 99.

(16) Schiavone, K.; Garnier, D.; Heymann, M.-F.; Heymann, D. *Adv. Exp. Med. Biol.* **2019**, *1139*, 187–200.

(17) Prater, S.; McKeon, B., *Osteosarcoma*; StatPearls Publishing: 2023.

(18) Schlegel, M.; Zeumer, M.; Prodinger, P. M.; Woertler, K.; Steinborn, M.; von Eisenhart-Rothe, R.; Burdach, S.; Rechl, H.; von Luettichau, I. *Oncology* **2018**, *94*, 354–362.

(19) Scully, S. P.; Ghert, M. A.; Zurakowski, D.; Thompson, R. C.; Gebhardt, M. C. *J. Bone Joint Surg. Am.* **2002**, *84*, 49–57.

(20) Lee, R. K. L.; Chu, W. C. W.; Leung, J. H. Y.; Cheng, F. W. T.; Li, C. K. *Pediatr. Blood Cancer* **2013**, *60*, 1118–1121.

(21) Zhou, Y.; Lu, Q.; Xu, J.; Yan, R.; Zhu, J.; Xu, J.; Jiang, X.; Li, J.; Wu, F. *Oncotarget* **2017**, *8*, 73037–73049.

(22) Chandrasekar, C. R.; Grimer, R. J.; Carter, S. R.; Tillman, R. M.; Abudu, A.; Jeys, L. M.; Cheung, W. G. H.; Sharma, R. *ISRN Oncol.* **2012**, *2012*, 512389.

(23) Greillier, P.; Bawiec, C.; Bessière, F.; Lafon, C. *IRBM* **2018**, *39*, 227–235.

(24) Vlaisavljevich, E.; Owens, G.; Lundt, J.; Teofilovic, D.; Ives, K.; Duryea, A.; Bertolina, J.; Welling, T. H.; Xu, Z. *Ultrasound Med. Biol.* **2017**, *43*, 1237–1251.

(25) Vidal-Jove, J.; Serres, X.; Vlaisavljevich, E.; Cannata, J.; Duryea, A.; Miller, R.; Merino, X.; Velat, M.; Kam, Y.; Bolduan, R.; Amaral, J.; Hall, T.; Xu, Z.; Lee Jr, F. T.; Ziemlewicz, T. J. *Int. J. Hyperthermia* **2022**, *39*, 1115–1123.

(26) Worlikar, T.; Mendiratta-Lala, M.; Vlaisavljevich, E.; Hubbard, R.; Shi, J.; Hall, T. L.; Cho, C. S.; Lee, F. T.; Greve, J.; Xu, Z. *BME Front.* **2020**, *2020*, 1–14.

(27) Schade, G. R.; Wang, Y.-N.; D'Andrea, S.; Hwang, J. H.; Liles, W. C.; Khokhlova, T. D. *Ultrasound Med. Biol.* **2019**, *45*, 137–147.

(28) Schade, G. R.; Keller, J.; Ives, K.; Cheng, X.; Rosol, T. J.; Keller, E.; Roberts, W. W. *J. Urol.* **2012**, *188*, 1957–1964.

(29) Duclos, S.; Golin, A.; Fox, A.; Chaudhary, N.; Camelo-Piragua, S.; Pandey, A.; Xu, Z. *Int. J. Hyperthermia* **2023**, *40*, 2237218.

(30) Sukovich, J. R.; Cain, C. A.; Pandey, A. S.; Chaudhary, N.; Camelo-Piragua, S.; Allen, S. P.; Hall, T. L.; Snell, J.; Xu, Z.; Cannata, J. M.; Teofilovic, D.; Bertolina, J. A.; Kassell, N.; Xu, Z. *J. Neurosurg.* **2019**, *131*, 1331–1338.

(31) Hendricks, A. D.; Howell, J.; Schmieley, R.; Kozlov, S.; Simon, A.; Coutermarsh-Ott, S. L.; Vlaisavljevich, E.; Allen, I. C. *J. Immunol.* **2019**, *202*, 194.30–194.30.

(32) Gannon, J. et al. *Int. J. Hyperthermia* **2023**, *40*, 2247187.

(33) Hendricks-Wenger, A.; Sereno, J.; Gannon, J.; Zeher, A.; Brock, R. M.; Beitel-White, N.; Simon, A.; Davalos, R. V.; Coutermarsh-Ott, S.; Vlaisavljevich, E.; Allen, I. C. *IEEE Trans. Ultrason. Ferroelectr. Freq. Control* **2021**, *68*, 2987–3000.

(34) Ruger, L.; Yang, E.; Gannon, J.; Sheppard, H.; Coutermarsh-Ott, S.; Ziemlewicz, T. J.; Dervisis, N.; Allen, I. C.; Daniel, G. B.; Tuohy, J.; Vlaisavljevich, E.; Klahn, S. *IEEE Trans. Biomed. Eng.* **2023**, *70*, 768–779.

(35) Vlaisavljevich, E.; Kim, Y.; Allen, S.; Owens, G.; Pelletier, S.; Cain, C.; Ives, K.; Xu, Z. *Ultrasound Med. Biol.* **2013**, *39*, 1398–1409.

(36) Arnold, L.; Hendricks-Wenger, A.; Coutermarsh-Ott, S.; Gannon, J.; Hay, A. N.; Dervisis, N.; Klahn, S.; Allen, I. C.; Tuohy, J.; Vlaisavljevich, E. *Ultrasound Med. Biol.* **2021**, *47*, 3435–3446.

(37) Lake, A. M.; Xu, Z.; Wilkinson, J. E.; Cain, C. A.; Roberts, W. W. *J. Urol.* **2008**, *179*, 1150–1154.

(38) Xu, Z.; Hall, T. L.; Vlaisavljevich, E.; Lee Jr, F. T. *Int. J. Hyperthermia* **2021**, *38*, 561–575.

(39) Guijarro, M. V.; Ghivizzani, S. C.; Gibbs, C. P. *Front. Oncol.* **2014**, *4*, 189.

(40) Ruger, L. N.; Hay, A. N.; Gannon, J. M.; Sheppard, H. O.; Coutermarsh-Ott, S. L.; Daniel, G. B.; Kierski, K. R.; Ciepluch, B. J.; Vlaisavljevich, E.; Tuohy, J. L. *IEEE Trans. Biomed. Eng.* **2022**, *PP*.

(41) Ruger, L. N.; Hay, A. N.; Vickers, E. R.; Coutermarsh-Ott, S. L.; Gannon, J. M.; Covell, H. S.; Daniel, G. B.; Laeseke, P. F.; Ziemlewicz, T. J.; Kierski, K. R.; Ciepluch, B. J.; Vlaisavljevich, E.; Tuohy, J. L. *Cancers (Basel)* **2023**, *15*, 741.

(42) Achari, P. F.; Vickers, E.; Ruger, L.; Vlaisavljevich, E.; Tuohy, J.; Collins, C. J. *Front. Vet. Sci.* **2026**, *12*.

(43) Mason, N. J. *Adv. Exp. Med. Biol.* **2020**, *1258*, 199–221.

(44) Lazarides, A. L.; Putterman, A. B.; Eward, W. C.; Eward, C. *Osteosarcoma–Biology, behavior and mechanisms* **2017**.

(45) Makielski, K. M.; Mills, L. J.; Sarver, A. L.; Henson, M. S.; Spector, L. G.; Naik, S.; Modiano, J. F. *Vet. Sci. China* **2019**, *6*.

(46) Simpson, S.; Rizvanov, A. A.; Jeyapalan, J. N.; de Brot, S.; Rutland, C. S. *Front. Vet. Sci.* **2022**, *9*, 965391.

(47) Dass, C. R.; Ek, E. T. H.; Choong, P. F. M. *J. Cancer Res. Clin. Oncol.* **2007**, *133*, 193–198.

(48) Berlin, O.; Samid, D.; Donthineni-Rao, R.; Akeson, W.; Amiel, D.; Woods Jr, V. L. *Cancer Res.* **1993**, *53*, 4890–4895.

(49) Khanna, C.; Prehn, J.; Yeung, C.; Caylor, J.; Tsokos, M.; Helman, L. *Clin. Exp. Metastasis* **2000**, *18*, 261–271.

(50) Asai, T.; Ueda, T.; Itoh, K., *Establishment and characterization of a murine osteosarcoma cell line (LM8) with high metastatic potential to the lung. I*, 1998.

(51) Walkley, C. R.; Qudsi, R.; Sankaran, V. G.; Perry, J. A.; Gostissa, M.; Roth, S. I.; Rodda, S. J.; Snay, E.; Dunning, P.; Fahey, F. H.; Alt, F. W.; McMahon, A. P.; Orkin, S. H. *Genes Dev.* **2008**, *22*, 1662–1676.

(52) Ng, A. J.; Mutsaers, A. J.; Baker, E. K.; Walkley, C. R. *Clin. Sarcoma Res.* **2012**, *2*, 19.

(53) Sereno, J.; Hendricks, A. D.; Allen, I. C.; Vlaisavljevich, E.; Imran, K. M.; Tuohy, J. *J. Immunol.* **2021**, *206*, 64.20–64.20.

(54) Hay, A. N.; Imran, K. M.; Hendricks-Wenger, A.; Gannon, J. M.; Sereno, J.; Simon, A.; Lopez, V. A.; Coutermarsh-Ott, S.; Vlaisavljevich, E.; Allen, I. C.; Tuohy, J. L. *Biomedicines* **2023**, *11*.

(55) Carriero, A.; Javaheri, B.; Bassir Kazeruni, N.; Pitsillides, A. A.; Shefelbine, S. J. *JBMR Plus* **2021**, *5*, e10467.

(56) Cheong, V. S.; Roberts, B. C.; Kadirkamanathan, V.; Dall'Ara, E. *Acta Biomater.* **2020**, *116*, 302–317.

(57) Berman, A. G.; Clauser, C. A.; Wunderlin, C.; Hammond, M. A.; Wallace, J. M. *PLoS One* **2015**, *10*, e0130504.

(58) Zhang, G.; Li, Z.; Li, N.; Shi, J.; Fan, H.; Mao, H. *J. Biomech.* **2022**, *144*, 111350.

(59) Jepsen, K. J.; Silva, M. J.; Vashishth, D.; Guo, X. E.; van der Meulen, M. C. H. *J. Bone Miner. Res.* **2015**, *30*, 951–966.

(60) Farooq, S.; Leussink, S.; Sparrow, L. M.; Marchini, M.; Britz, H. M.; Manske, S. L.; Rolian, C. *Sci. Rep.* **2017**, *7*, 10527.

(61) Brodt, M. D.; Silva, M. J. *J. Bone Miner. Res.* **2010**, *25*, 2006–2015.

(62) Oliviero, S.; Cheong, V. S.; Roberts, B. C.; Orozco Diaz, C. A.; Griffiths, W.; Bellantuono, I.; Dall'Ara, E. *Front. Endocrinol. (Lausanne)* **2022**, *13*, 915938.

(63) Gatenby, P.; Basten, A. *Cancer Immunol. Immunother.* **1980**, *8-8*, 95–102.

(64) Yahiro, K.; Matsumoto, Y.; Yamada, H.; Endo, M.; Setsu, N.; Fujiwara, T.; Nakagawa, M.; Kimura, A.; Shimada, E.; Okada, S.; Oda, Y.; Nakashima, Y. *Cancer Immunol. Immunother.* **2020**, *69*, 745–758.

(65) Hendricks-Wenger, A.; Weber, P.; Simon, A.; Saunier, S.; Coutermarsh-Ott, S.; Grider, D.; Vidal-Jove, J.; Allen, I. C.; Luyimbazi, D.; Vlaisavljevich, E. *IEEE Trans. Ultrason. Ferroelectr. Freq. Control* **2021**, *68*, 2953–2964.

(66) Otsu, N. *IEEE Trans. Syst. Man Cybern.* **1979**, *9*, 62–66.

(67) Kohler, T.; Stauber, M.; Donahue, L. R.; Müller, R. *Bone* **2007**, *41*, 659–667.

(68) Pelker, R. R.; Friedlaender, G. E.; Panjabi, M. M.; Markham, T.; Hausman, M.; Doganis, A. C.; McKay, J. *J. Orthop. Res.* **1985**, *3*, 91–95.

(69) Van Leeuwen, B. L.; Verkerke, G. J.; Hartel, R. M.; Sluiter, W. J.; Kamps, W. A.; Jansen, H. W. B.; Hoekstra, H. J. *Clin. Orthop. Relat. Res.* **2003**, *413*, 243–254.

(70) Nørregaard, K. S.; Jürgensen, H. J.; Gårdsvoll, H.; Engelholm, L. H.; Behrendt, N.; Søe, K. *Int. J. Mol. Sci.* **2021**, *22*, 6865.

(71) Cè, M.; Cellina, M.; Ueanukul, T.; Carrafiello, G.; Manatrakul, R.; Tangkittithaworn, P.; Jaovisidha, S.; Fuangfa, P.; Resnick, D. *Cancers (Basel)* **2025**, *17*.

(72) Cooper, D. M. L.; Kawalilak, C. E.; Harrison, K.; Johnston, B. D.; Johnston, J. D. *Curr. Osteoporos. Rep.* **2016**, *14*, 187–198.

(73) Rowe, P.; Koller, A.; Sharma, S. In *StatPearls*; StatPearls Publishing: Treasure Island (FL), 2025.

(74) Nyman, J. S.; Uppuganti, S.; Makowski, A. J.; Rowland, B. J.; Merkel, A. R.; Sterling, J. A.; Bredbenner, T. L.; Perrien, D. S. *BoneKEy Rep.* **2015**, *4*, 664.

(75) Alomari, A. H.; Wille, M.-L.; Langton, C. M. *Bone* **2018**, *107*, 145–153.

(76) Jilka, R. L. *J. Gerontol. A Biol. Sci. Med. Sci.* **2013**, *68*, 1209–1217.

(77) Seeman, E. *Rheumatology (Oxford)* **2008**, *47 Suppl 4*, iv2–8.

(78) Seeman, E. *Endocrinol. Metab. (Seoul)* **2015**, *30*, 419–428.

(79) Main, R. P.; Shefelbine, S. J.; Meakin, L. B.; Silva, M. J.; van der Meulen, M. C. H.; Willie, B. M. *J. Orthop. Res.* **2020**, *38*, 233–252.

(80) Garrison, J. G.; Gargac, J. A.; Niebur, G. L. *J. Biomech.* **2011**, *44*, 2747–2754.

(81) Perilli, E.; Baleani, M.; Ohman, C.; Fognani, R.; Baruffaldi, F.; Viceconti, M. *J. Biomech.* **2008**, *41*, 438–446.

(82) Wu, Y.; Adeeb, S.; Doschak, M. R. *Front. Endocrinol. (Lausanne)* **2015**, *6*, 80.

(83) Bala, Y.; Zebaze, R.; Ghasem-Zadeh, A.; Atkinson, E. J.; Iuliano, S.; Peterson, J. M.; Amin, S.; Bjørnerem, Å.; Melton 3rd, L. J.; Johansson, H.; Kanis, J. A.; Khosla, S.; Seeman, E. *J. Bone Miner. Res.* **2014**, *29*, 1356–1362.

(84) Steffey, M. A.; Garcia, T. C.; Daniel, L.; Zwingenberger, A. L.; Stover, S. M. *Vet. Surg.* **2017**, *46*, 539–548.

(85) Jiang, F.; Liu, S.; Chen, A.; Li, B.-Y.; Robling, A. G.; Chen, J.; Yokota, H. *Int. J. Orthop. (Hong Kong)* **2018**, *5*, 863–871.

(86) Pereira, A. F.; Javaheri, B.; Pitsillides, A. A.; Shefelbine, S. J. *J. R. Soc. Interface* **2015**, *12*, 0590.

Chapter 5

High-Intensity Focused Ultrasound as a Comparative Focused Ultrasound Modality

The following chapter characterizes the time-series structural and mechanical effects of high-intensity focused ultrasound (HIFU) ablation in a murine osteosarcoma (OS) model. While HIFU is not currently used as a curative treatment modality for OS, these findings provide a foundation for comparing how different focused ultrasound techniques interact with OS tumor-bearing bone. The manuscript highlighting the results of this study is currently under preparation.

5.1 Introduction

High-intensity focused ultrasound (HIFU) is a thermal focused ultrasound modality that concentrates energy at a focal point, rapidly heating targeted tissue to induce coagulative necrosis[1]. HIFU is clinically established for thermal ablation in soft-tissue tumors including breast[2], prostate[3], pancreatic[4], and hepatic[5] cancers, and is routinely applied for treatment of uterine fibroids[6]. HIFU has also been shown to stimulate bone remodeling, although excessive or misdirected heating can degrade cortical integrity[7,8]. In oncology, its primary role has been palliative rather than curative; by thermally ablating nociceptive nerve fibers

within tumor margins, HIFU can provide substantial pain reduction with minimal adverse side effects, particularly in patients with advanced disease[4,9–11].

Applications of HIFU in bone are limited due to challenging ultrasound-bone interactions; cortical bone absorbs roughly 50 times more ultrasound energy than soft tissue, producing steep temperature gradients in surrounding tissue and restricting penetration depth[1]. Nevertheless, investigating HIFU is important, as it is a clinically available modality for palliative treatment of primary bone tumors and induces thermal and biological effects that may differ from nonthermal modalities such as histotripsy. Characterizing these effects establishes a benchmark for understanding how different focused ultrasound therapies interact with tumor-bearing and healthy bone, informing the development of safe, effective, limb sparing treatment strategies.

Using the same orthotopic murine OS model detailed in the preceding chapter, HIFU ablation was performed on OS tumor-bearing limbs and changes in bone morphology and whole-bone mechanical performance were quantified. This study complements prior work with histotripsy ablation by providing comparative insights into how thermal and nonthermal focused ultrasound modalities affect the mechanics of tumor-bearing bone.

5.2 Methods

The tumor induction, animal handling, imaging, and mechanical testing protocols used in this study were identical to those described in Chapter 4.3, unless otherwise noted. Female C3H/HeJ mice (8-10 weeks old, n=12) were orthotopically injected with DLM8 murine OS cells into the right tibia. Approximately 10 days post-injection, mice underwent HIFU ablation and were subsequently sacrificed at 3 (n=4), 7 (n=4), or 14 (n=4) days post-treatment. HIFU-ablated tumor-bearing (AT) and contralateral, unablated normal (UN) tibiae were harvested and stored hydrated at -20 until μCT imaging and mechanical testing.

HIFU ablation was performed using a 1.15MHz single-element transducer integrated with the RK-300 focused ultrasound system (FUS Instruments Inc., Ontario, Canada) and a 9.4 T USR MR scanner (Fralin Biomedical Research Institute, Virginia Tech, Roanoke, VA). Mice were anesthetized and positioned on a custom, acoustically transparent platform above a degassed water reservoir containing the transducer. Tumors were visualized using a 2D Rapid Imaging with Refocused Echoes (RARE) sequence, and dimensions were measured assuming elliptical geometry. A single 30s sonication at 13W was delivered to the tumor center, achieving a target tissue temperature of approximately 60 °C based on preliminary data.

μCT imaging, mechanical testing, and statistical analyses were conducted as described in Chapter 4.3; however, analyses were restricted to the cortical ROI located 37% of tibial length distal to the proximal metaphysis and the trabecular ROI proximal to the growth plate.

Statistical analyses were conducted using a linear mixed-effects model (LMEM) to assess time-dependent effects of HIFU ablaton, with mouse included as a random effect to account for paired tibiae. If the interaction term was not significant, the model was reduced and main effects were interpreted. Post-hoc paired t-tests were performed where appropriate. p-values were adjusted using the Holm-Bonferroni method and statistical significance was defined as $\alpha = 0.05$.

5.3 Results

HIFU-treated tibiae exhibit altered cortical morphology

The LMEM did not reveal any significant interactions between group and time for any assessed morphometric parameters, including cortical porosity (Ct.Po), cortical thickness (Ct.Th), cortical area (Ct.Ar), and trabecular bone volume fraction (Tb.BV/TV), so the

model was simplified and main effects were interpreted. Overall, UN tibiae exhibited higher Tb.BV/TV than AT tibiae (p=0.050), with post-hoc tests confirming this difference at 3 and 7 days post-ablation (p=0.0472). No significant differences were detected for Ct.Ar or Ct.Po at the 37% site, although AT specimens trended toward higher porosity at later time points (7 and 14 days post-ablation, Figure 5.1). Ct.Th was significantly higher in UN than in AT overall (p<0.001), with post-hoc analysis confirming this difference at 14 days post-ablation (p=0.011).

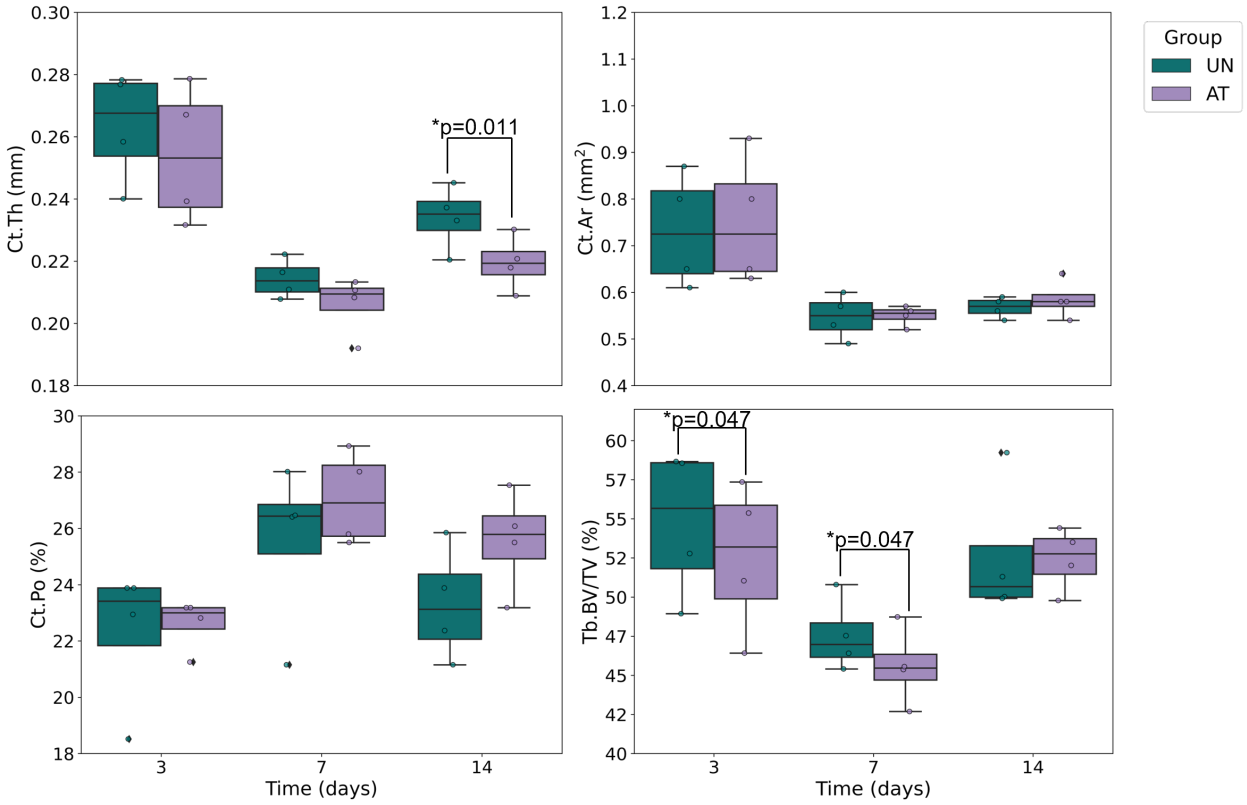

Figure 5.1: Select morphometric parameters for UN and AT groups 3, 7, and 14 days post-HIFU ablation at the 37% cortical site. * indicates statistical significance as determined by post-hoc analysis (p<0.05).

Mechanical effects of HIFU vary over time

The LMEM revealed a significant interaction between group and time for both stiffness and ultimate load (p < 0.001 and p=0.003, respectively), indicating that the effects of HIFU ablation varied over time. Overall, UN tibiae tended to exhibit greater stiffness and ultimate

load than AT tibiae ($p<0.001$ and $p=0.001$, respectively). At early time points (3 and 7 days post-ablation), stiffness did not differ significantly between UN and AT tibiae, although AT tibiae trended lower than controls ($p=0.064$, Table 5.1). By 14 days, however, stiffness was significantly higher in AT tibiae compared to UN controls ($p = 0.011$). Similarly, AT tibiae had lower failure load overall ($p = 0.001$), but this difference decreased over time, as indicated by significant positive group x time interaction terms at 7 and 14 days post-ablation ($p = 0.009$ and $p = 0.003$, respectively). However, post-hoc within-group comparisons across time revealed no significant differences in stiffness or failure load for either group. No significant differences in toughness were detected between UN and AT tibiae at any time point.

Table 5.1: Whole bone mechanical properties for UN and AT groups at 3, 7, and 14 days post-HIFU ablation. Data is reported as mean ± standard deviation.

Property / Group		Time point (days)		
		3	7	14
Ultimate load (N)	UN	65.5 ± 11.1	45.1 ± 11.8	49.1 ± 10.5
	AT	45.4 ± 7.02	48.0 ± 5.95	55.4 ± 3.22
Stiffness (N/mm)	UN	115 ± 9.12	117 ± 22.8	74.1 ± 16.7
	AT	72.4 ± 20.1	66.3 ± 16.5	96.7 ± 17.9
Toughness (MPa)	UN	2.57 ± 1.20	3.02 ± 2.40	2.72 ± 0.390
	AT	1.93 ± 0.710	3.52 ± 1.35	4.19 ± 1.91

5.4 Discussion

This study examined the effects of high-intensity focused ultrasound (HIFU) ablation on bone morphology and whole-bone mechanical properties in a murine osteosarcoma (OS) model. The results demonstrate that while HIFU may initially reduce load-bearing capacity and stiffness in OS tumor-bearing bone, these properties recover by 14 days post-ablation, suggesting an adaptive mechanical response consistent with early bone remodeling.

At early time points (3–7 days post-ablation), ablated tumor-bearing (AT) tibiae trended toward lower stiffness and failure load compared to unablated normal (UN) controls, consistent with OS-driven tissue disruption and weakening[12]. By 14 days, however, the stiffness of AT tibiae exceeded that of unablated controls and differences in failure load diminished, indicating partial recovery of load-bearing capacity. This mechanical recovery may reflect early remodeling processes triggered by HIFU-induced microdamage, localized heating, or vascular perturbation, mechanisms that have been shown in other preclinical[13] and clinical[14] applications to initiate osteogenesis and subsequent reinforcement of the ablated bone.

Morphometric analysis revealed significant differences between AT and UN tibiae, but no significant group x time interactions were observed. AT tibiae exhibited lower cortical thickness and Tb.BV/TV compared to UN controls, consistent with OS-driven osteolysis and potential post-ablation resorption.

Although direct comparison between the histotripsy and HIFU studies presented in this thesis is limited due to differences in animal age (4-6 weeks and 8-10 weeks, respectively) and associated disparities in baseline skeletal maturity, several qualitative trends highlight how these modalities distinctly interact with OS tumor-bearing and normal bone. Histotripsy primarily induced localized structural changes, reflected in alterations in cortical parameters, while largely preserving whole-bone mechanical properties in both tumor-bearing and normal tibiae. In contrast, HIFU produced a more pronounced, transient reduction in mechanical properties early post-ablation period, with stiffness and failure load initially suppressed in treated tibiae before recovering to or exceeding those unablated controls by 14 days. Notably, histotripsy did not produce significant group-time interactions in mechanical properties, suggesting a predominantly mechanical mechanism that alters geometry without producing a mechanical deficit. Conversely, HIFU likely induces early thermally driven alterations to tissue structure that temporarily weaken bone, which resolves as the bone remodels. Across both modalities, the partial recovery of properties over the observation period suggests adaptation consistent with active remodeling. Together, these findings suggest that

both modalities preserve long-term mechanical integrity of OS tumor-bearing bone, but in different ways; histotripsy through subtle, geometry-driven adaptation and HIFU through transient mechanical suppression followed by compensatory recovery.

5.5 Conclusions

The aim of this work was to evaluate the structural and mechanical effects of HIFU on OS tumor-bearing and contralateral healthy limbs. Overall, the findings indicate that HIFU ablation induces an early, transient reduction in mechanical performance in tumor-bearing bone, followed by structural and functional recovery within two weeks. This trajectory is consistent with previously observed patterns of bone adaptation to mechanical or thermal disruption, in which initial weakening is compensated for by remodeling and increased structural reinforcement. The absence of substantial morphological deterioration, along with preserved toughness, suggests that HIFU does not irreversibly compromise bone integrity. These results support the potential of HIFU as a minimally invasive, localized therapy capable of controlling tumor burden while maintaining or restoring bone strength, and provide a useful benchmark for comparison with nonthermal therapeutic modalities such as histotripsy.

5.6 Acknowledgments

The authors gratefully acknowledge the support of the National Institutes of Health (NIH) [R01CA289288], the Veterinary Memorial Fund at Virginia Tech, the Focused Ultrasound Foundation, and the Virginia Tech COE EFO-O Program. Elliana Vickers was supported by a Ruth L. Kirschstein Predoctoral Individual National Research Service Award from the National Cancer Institute [1F31CA294976-01] for the duration of this work. Lauren Ruger has an ongoing consulting relationship with Theraclion. Eli Vlaisavljevich is a cofounder

and stockholder of Sound Blade Medical.

Works Cited

(1) Yeo, S. Y.; Bratke, G.; Grüll, H. *Cancers (Basel)* **2022**, *15*, 108.

(2) Merckel, L. G.; Knuttel, F. M.; Deckers, R.; van Dalen, T.; Schubert, G.; Peters, N. H. G. M.; Weits, T.; van Diest, P. J.; Mali, W. P. T. M.; Vaessen, P. H. H. B.; van Gorp, J. M. H. H.; Moonen, C. T. W.; Bartels, L. W.; van den Bosch, M. A. A. J. *Eur. Radiol.* **2016**, *26*, 4037–4046.

(3) Uchida, T.; Ohkusa, H.; Nagata, Y.; Hyodo, T.; Satoh, T.; Irie, A. *BJU Int.* **2006**, *97*, 56–61.

(4) Wang, K.; Chen, Z.; Meng, Z.; Lin, J.; Zhou, Z.; Wang, P.; Chen, L.; Liu, L. *Int. J. Hyperthermia* **2011**, *27*, 101–107.

(5) Leslie, T.; Ritchie, R.; Illing, R.; Ter Haar, G.; Phillips, R.; Middleton, M.; Bch, B.; Wu, F.; Cranston, D. *Br. J. Radiol.* **2012**, *85*, 1363–1370.

(6) Hindley, J. et al. *AJR Am. J. Roentgenol.* **2004**, *183*, 1713–1719.

(7) Yeo, S. Y.; Arias Moreno, A. J.; van Rietbergen, B.; Ter Hoeve, N. D.; van Diest, P. J.; Grüll, H. *J. Ther. Ultrasound* **2015**, *3*, 13.

(8) Smith, N. B.; Temkin, J. M.; Shapiro, F.; Hynynen, K. *Ultrasound Med. Biol.* **2001**, *27*, 1427–1433.

(9) Wu, F.; Wang, Z.-B.; Zhu, H.; Chen, W.-Z.; Zou, J.-Z.; Bai, J.; Li, K.-Q.; Jin, C.-B.; Xie, F.-L.; Su, H.-B. *Radiology* **2005**, *236*, 1034–1040.

(10) Yu, W.; Tang, L.; Lin, F.; Yao, Y.; Shen, Z.; Zhou, X. *Surg. Oncol.* **2015**, *24*, 9–15.

(11) Li, C.; Zhang, W.; Fan, W.; Huang, J.; Zhang, F.; Wu, P. *Cancer* **2010**, *116*, 3934–3942.

(12) Nørregaard, K. S.; Jürgensen, H. J.; Gårdsvoll, H.; Engelholm, L. H.; Behrendt, N.; Søe, K. *Int. J. Mol. Sci.* **2021**, *22*, 6865.

(13) Bucknor, M. D.; Rieke, V.; Seo, Y.; Horvai, A. E.; Hawkins, R. A.; Majumdar, S.; Link, T. M.; Saeed, M. *Radiology* **2015**, *274*, 387–394.

(14) Napoli, A.; Anzidei, M.; Marincola, B. C.; Brachetti, G.; Ciolina, F.; Cartocci, G.; Marsecano, C.; Zaccagna, F.; Marchetti, L.; Cortesi, E.; Catalano, C. *Invest. Radiol.* **2013**, *48*, 351–358.

Chapter 6

μCT-Based Finite Element Modeling of Osteosarcoma Tumor-Bearing Limbs with Validation using Digital Image Correlation

6.1 Introduction

Noninvasive characterization of how osteosarcoma (OS) and focal ablation therapies influence whole-bone mechanics is essential for evaluating fracture risk and optimizing limb-salvage strategies. Mechanical testing provides direct measurements of whole-bone stiffness and failure load but is inherently destructive and incapable of resolving spatial strain heterogeneity or load distribution within the bone. As a result, there is a need for the development of noninvasive approaches that capture patient-specific mechanical behavior as a response to disease or therapy.

Image-based finite element (FE) models have advanced as a powerful tool for estimating patient-specific bone mechanics; however, their application to primary OS lesions remains limited. Standard clinical imaging modalities such as DXA, CT, and qCT are commonly used to assess bone strength and fracture risk, but these approaches can have significant limitations. DXA-based models rely primarily on bone mineral density, limiting predictive

accuracy[1,2], while CT-based FE models often struggle to distinguish tumor tissue and surrounding vasculature[3–5]. Existing CT-based FE models of OS have relied on simplified representations of tumor involvement, such as osteotomies and homogeneous material property assignments, which fail to capture the mixed osteolytic and osteoblastic regions characteristic of the disease[6,7].

Micro-computed tomography (μCT) overcomes many of these limitations by providing high-resolution, 3D characterization of cortical porosity, trabecular architecture, and localized variations in mineral density[8,9]. Although μCT is not clinically translatable due to radiation dose and field-of-view constraints, μCT-based FE models can be used to establish validated density-modulus relationships and assess model sensitivity to tumor- and treatment-induced heterogeneity[10]. Insights gained from such studies can improve interpretation of lower-resolution clinical data.

Experimental validation of FE predictions is critical, particularly for specimens with pronounced geometric and material heterogeneity. 3D digital image correlation (DIC) enables non-contact, full-field surface strain measurements throughout mechanical loading and is well-suited for bones with complex curvature or induced remodeling, which can produce nonuniform deformation patterns[11–13]. While prior studies have demonstrated good agreement between DIC-measured and FE-predicted surface strains in healthy murine long bones[14,15], validation of FE models in tumor-bearing or treatment-altered bone remains limited.

In this chapter, 3D DIC strain analysis was performed on murine tibiae across four experimental conditions: unablated normal (UN), histotripsy-ablated normal (AN), unablated OS tumor-bearing (UT), and ablated tumor-bearing (AT) limbs from 14 days following histotripsy ablation. Specimen-specific μCT-based FE models were generated for representative samples from each group, and FE-predicted surface longitudinal strains under elastic loading were compared directly to experimentally measured DIC strains within corresponding regions of interest. The primary objective of this study was to evaluate the feasibility of μCT-

based FE modeling for capturing pre-yield, tumor- and treatment-induced heterogeneity in whole-bone mechanics, informing future studies aimed at translating these computational tools to clinically relevant fracture risk prediction and treatment planning strategies in OS.

6.2 Methods

Tumor induction, histotripsy ablation, tissue harvesting, μCT image acquistion and processing, and mechanical testing protocols are described in Chapter 4.2.

Digital image correlation (DIC):

Prior to mechanical testing, tibiae were thawed at room temperature (20 °C) and hydrated with 1x PBS to preserve mechanical integrity. Each tibia was aligned vertically, along the primary axis of physiological loading, using a reference standard to minimize off-axis loading during mechanical tesing. Both proximal and distal ends were embedded in UV-curable resin using a custom cylindrical mold (Chapter 4.2 such that 3mm of each end were rigidly fixed.

After potting, the exposed anteromedial surface of each tibia was coated with a thin layer of matte white water-based paint, followed by a randomized black speckle pattern applied with a high-precision airbrush (Iwata, Tokyo, Japan). Speckle size and density were optimized in preliminary trials to maximize subset correlation while maintaining spatial resolution of the DIC data.

Two synchronized stereo cameras equipped with 100mm macro lenses (Schneider-Kreuznach, Germany) were positioned horizontally in front of the loading fixture to capture a stereoscopic field of view. Cameras were calibrated prior to each test using a 12mm x 9mm calibration grid (pitch: 0.89mm, Correlated Solutions, SC, USA), following standard stereo-DIC calibration procedures. A pair of LED light sources fitted with cross-polarizing filters were installed to illuminate the specimen while minimizing glare.

Images were acquired at 10Hz throughout compressive loading until failure using Vic-Snap. DIC analysis was performed using the complementary Vic-3D software (version 10, Correlated Solutions, SC, USA). Subset size was set to 85x85 pixels with a 9-pixel step size, resulting in approximately 10-15 speckles per subset and an effective spatial resolution of 0.35 mm. Longitudinal strain (ε_{yy}), aligned with the bone's longitudinal axis, was computed along the entire gauge length using Lagrangian strain formulation[vic3d10]. Apparent whole-bone stiffness was calculated from the linear elastic region (15-20N) of the force (450 N load cell) via a DIC-derived (digital extensometer) displacement curve, using fixed reference points. DIC-measured axial displacements between proximal and distal points on the exposed surface were tracked and synced to the force vs time data collected from the load frame (ElectroForce 3200, TA Instruments DE, USA). Qualitative assessment of post-yield DIC data was performed on select specimens to visualize changes in strain distributions closer to the point of fracture.

Two cortical ROIs were defined along the anteromedial surface of each tibia: (1) the 37% cortical ROI, spanning 1.75mm longitudinally and centered at 37% of total bone length from the proximal end, and (2) the proximal ROI, spanning 80% of the distance from the proximal surface to the tibiofibular junction. Strain fields were filtered using a Savistzky-Golay filter, and differences between raw and filtered values were quantified using the Wilcoxon signed-rank test.

Finite element mesh generation:

Micro-CT image stacks (voxel size: $8.44\mu m^3$) were imported into Mimics Core (version 27.0, Materialise, Belgium) for processing. Volumes were cropped to remove 3mm from each tibial end, ensuring consistency with the experimentally exposed gauge length and excluding resin contributions. Trabecular bone in the metaphysis was embedded and therefore excluded, focusing analyses on the cortical diaphysis. Cortical bone was segmented using global Otsu thresholding informed by specimen-specific grayscale histograms. Post-segmentation smooth-

ing and morphological operations were applied to reduce artifacts while preserving cortical geometry.

Surface meshes were generated from the cortical masks and converted to quadratic tetrahedral (tet10) volumetric meshes using 3-Matic (version 20.0, Materialise, Belgium). To balance computational efficiency and strain accuracy, a region-specific mesh refinement strategy was implemented; the distal length of the tibia was initially meshed with an element edge length of 0.25mm, while the proximal ROI, including the 37% cortical ROI, was subjected to refinement with element edge lengths of 0.25mm, 0.175mm, and 0.1mm. Mesh convergence was assessed by monitoring changes in global axial stiffness and proximal cortical strain. The final mesh configuration was selected such that further refinement resulted in <10% change in these quantities.

Material property assignment:

A dual-material linear elastic material model was implemented, consisting of cortical bone and marrow. No significant differences were observed in apparent stiffness measured from mechanical testing (Chapter 4.3), therefore homogeneous material properties were assigned to each tissue. Cortical bone was assigned a literature-based elastic modulus of 14.8GPa and a Poisson's ratio of 0.3.[16] Expected to contribute minimally to axial stiffness, marrow was assigned an elastic modulus of 50MPa to maintain numerical stability.

Boundary conditions and loading:

Boundary conditions were defined to replicate experimental uniaxial compression. The distal end was constrained in all translational degrees of freedom (DOF) to prevent rigid body motion. Axial displacement was applied to the proximal surface along the longitudinal (z) axis, and reaction forces were recorded. Contact between bone and loading surfaces was assumed frictionless, and all simulations were performed under quasi-static conditions.

Finite element simulations:

Uniaxial loading simulations were performed using Abaqus/CAE 2024 (Dassault Systèmes Simulia Corp., RI, USA) under static general step conditions. Nodal displacements, reaction forces, and axial strains (E33) were extracted from nodes corresponding to the proximal cortical ROI, using the same pre-yield load range (15-20N) as the analyzed DIC data for direct comparison. Solution convergence was verified by monitoring force-displacement behavior and ensuring numerical stability.

Experimental validation:

The cortical ROIs defined on the DIC surface were mapped to the corresponding FE model surface. Because element edge length (0.1mm-0.25mm) was smaller than the DIC subset size (0.35 mm), ROI-averaged FE-predicted strains inherently reflect comparable or finer spatial resolution. Post-yield behavior was qualitatively evaluated via strain maps at frames nearest to peak load for representative specimens, providing insight into local strain heterogeneity closer to fracture.

Statistical analysis:

Differences in local DIC-derived strain between experimental groups were assessed using Welch's ANOVA with Games-Howell post-hoc tests. Comparisons of FE-predicted and DIC-measured strains within the elastic regime were quantified using percent error. Normality and homogeneity of variance were assessed using the Shapiro-Wilk and Levene's tests, respectively. Data are presented as mean ± standard deviation for normally distributed data, and as median (IQR) for nonparametric data. Statistical significance was defined as $p<0.05$.

6.3 Results

All 8 mice completed the study. A total of 14 tibiae were analyzed; two ablated tumor-bearing samples were excluded from further DIC and FEA analysis due to substantial camera glare, which prevented reliable spatial correlation within the defined ROIs.

DIC reconstruction quality, quantified by the projection error, was highest in unablated tumor-bearing (UT, 2.41 ± 1.97 pixels) specimens relative to unablated normal (UN, 0.540 ± 0.528 pixels) and ablated normal (AN, 0.286 ± 0.178 pixels) specimens. Ablated tumor-bearing (AT, 0.582 ± 0.155 pixels) specimens are reported descriptively but were excluded from statistical comparisons due to small sample size (n=2). No significant differences were observed between raw and filtered strains for either 37% cortical or proximal cortical ROI measurements, indicating that filtering did not bias strain magnitude, therefore filtered strains were used for subsequent analyses.

Finite element mesh convergence:

Mesh convergence for the finite element models was assessed in a representative UN tibia. Global apparent axial stiffness converged to within <1% variance, while local strains sampled from the proximal cortical ROI achieved marginal convergence with a 10.8% variance at the final mesh resolution (Figure 6.1). Based on these results, the final mesh for all FE models was assigned an element edge length of 0.1mm in the proximal cortical region and 0.25mm in the distal region, balancing computational efficiency with adequate representation of both global and local behavior.

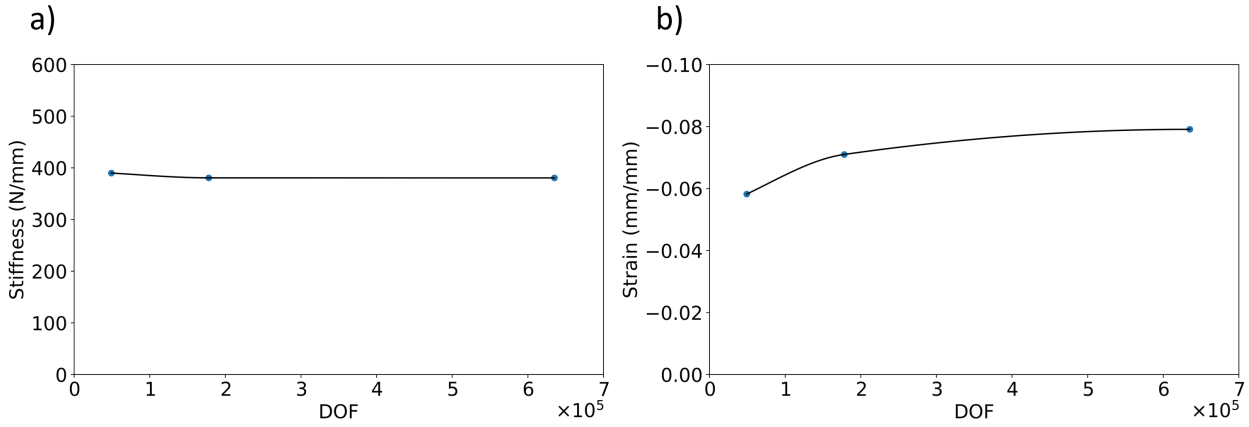

Figure 6.1: a) Convergence plot of global stiffness and b) local proximal cortical ROI strain vs DOF for a representative UN tibia. Variances of <1% and 10.8% were achieved, respectively.

Global stiffness and local strain comparative analysis

Apparent axial stiffness (N/mm) derived from DIC showed close agreement with FE predictions for representative UN, AN, and AT tibiae, with differences within 11%. In contrast, the UT tibia exhibited substantially higher DIC-derived stiffness compared to FE predictions (106%, Figure 6.2). Across groups, mechanical stiffness (measured from the load cell and crosshead displacements from Chapter 4.3) was reduced by approximately 6x relative to DIC measurements. Individual differences in mechanically and DIC-derived stiffnesses within specimens ranged from 1.5-12x, indicating a range in specimen or test-frame compliance recorded in the raw force-crosshead deflection data.

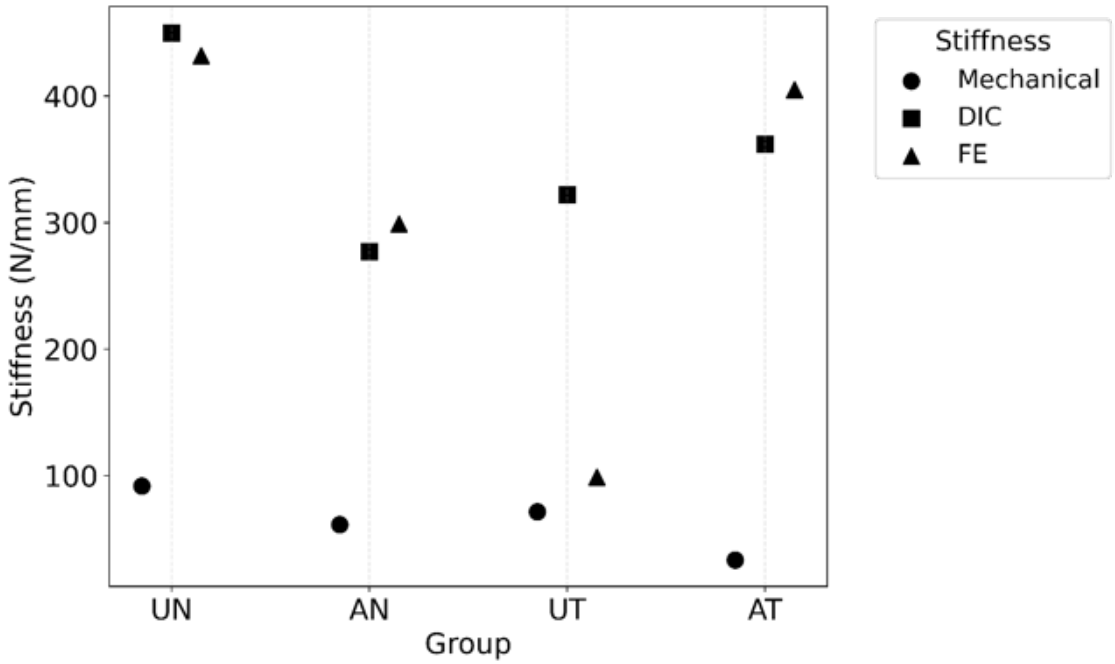

Figure 6.2: a) Mechanically-, DIC-, and FE-derived stiffnesses for representative UN, AN, UT, and AT tibiae 14 days post-histotripsy ablation.

FE-predicted axial strains of representative tibiae showed qualitative agreement with DIC-derived measurements at a 20N applied load, and preserved directional group-level trends for both the proximal cortical and 37% cortical ROIs (Figure 6.3). UT tibiae exhibited the greatest variability in local strain measurements and the largest percent error relative to FE predictions (Table 6.1), consistent with poorer DIC correlation quality and increased heterogeneous mechanical behavior due to tumor-induced surface irregularities.

No statistical differences in strain magnitude was observed between experimental groups, and strains were comparable between the proximal and 37% cortical ROIs within individual specimens. These findings suggest that strains measured within the proximal cortical ROI capture representative local mechanical behavior near the tumor induction site under elastic loading conditions.

Table 6.1: Average DIC-derived and FE-predicted strains for 37% cortical and proximal cortical ROIs by group. Values are reported as mean ± standard deviation. FE standard deviations represent spatial variability across surface nodes within the defined ROI. Percent error was calculated relative to DIC-derived mean strain magnitude for each specimen.

Group	DIC-derived strain (mm/mm)		FE-predicted strain (mm/mm)		Percent error (%)	
	Proximal ROI	37% ROI	Proximal ROI	37% ROI	Proximal ROI	37% ROI
UN	-0.00537 ± 0.00458	-0.00476 ± 0.00318	-0.00380 ± 0.00462	-0.00162 ± 0.00239	29.2	66.4
AN	-0.00770 ± 0.00334	-0.00379 ± 0.00253	-0.00232 ± 0.00278	-0.00221 ± 0.00315	69.9	44.6
UT	-0.00359 ± 0.00871	-0.00224 ± 0.00314	-0.00070 ± 0.00161	-0.00095 ± 0.00238	80.5	57.6
AT	-0.00294 ± 0.00378	-0.00324 ± 0.00252	-0.00209 ± 0.00220	-0.00194 ± 0.00264	28.8	40.1

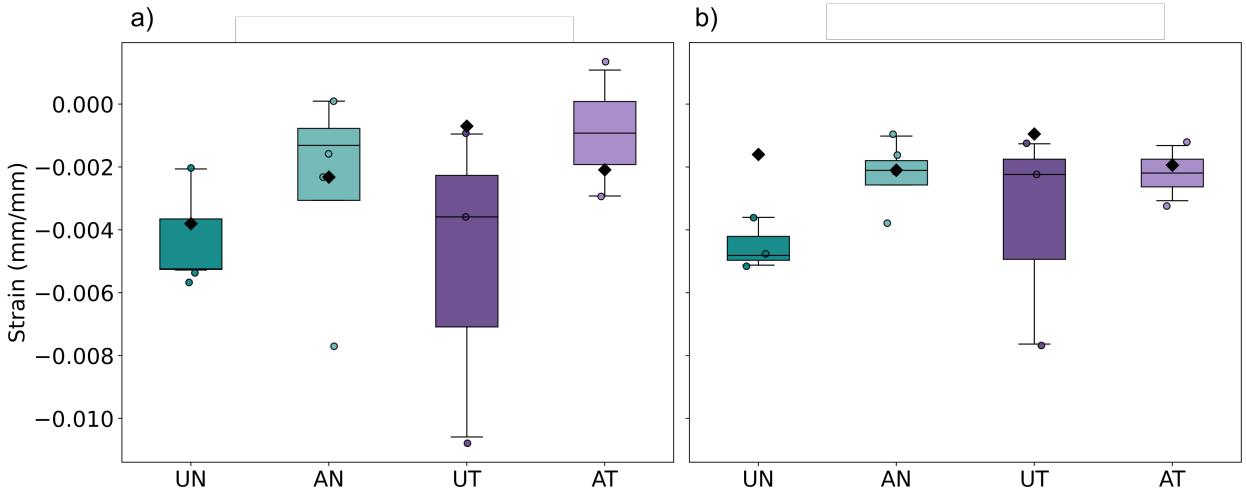

Figure 6.3: DIC-derived strain at 20N for all groups 14 days post-histotripsy ablation for the a) proxmial cortical ROI and b) 37% cortical ROI. FE-predicted strains are represented by ⧫.

Post-yield deformation was assessed qualitatively in representative specimens from each group. DIC-derived axial strain fields at 20N and at the frame nearest to peak load demonstrated progressive strain localization with increasing load, with pronounced heterogeneous

strain concentrations particularly visible in the UT tibia. FE models, which were limited to pre-yield conditions, exhibited similar spatial strain distribution patterns compared to DIC-derived distributions, but did not capture post-yield deformation or failure progression (Figure 6.4). These comparisons provide qualitative validation of the FE model's ability to identify regions of high strain while acknowledging quantitative limitations.

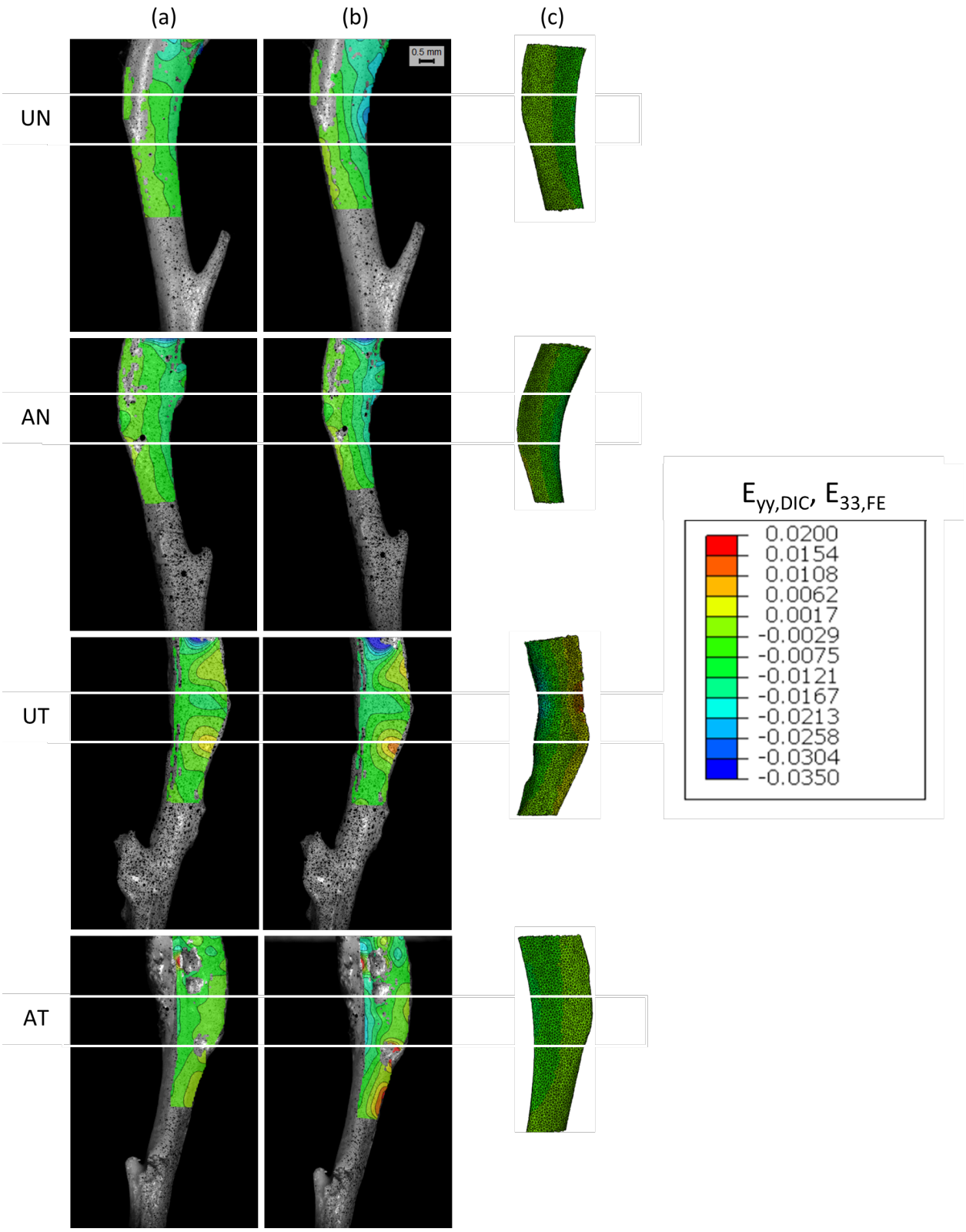

Figure 6.4: Strain distribution maps for the proximal cortical ROI of representative samples. a) and b) depict strains at 20N and at the frame nearest to peak load, respectively. c) depicts FE-predicted strains. Matched 37% cortical ROI boundary lines are shown in white.

6.4 Discussion

In this study, negligible discrepancies between stiffness measurements derived from DIC and those predicted by FE were observed in representative UN, AN, and AT tibiae (<11% error); however, DIC-derived stiffness was substantially higher in the UT tibia (106% error), despite identical homogeneous elastic properties and boundary conditions across all FE models. This discrepancy likely reflects local stiffening effects caused by irregular cortical thickening or periosteal expansion associated with tumor growth, which are captured by surface-based DIC measurements but not represented in simplified homogeneous FE models. In AT bone, this discrepancy was less pronounced, potentially due to the combined effects of tumor-induced periosteal expansion and ablation-induced cortical changes, including increased cortical porosity and decreased cortical thickness. These results indicate that while homogeneous FE models reliably capture global stiffness in normal and ablated bone, they may unreliably estimate stiffness in untreated tumor-bearing bone.

Local strain comparisons across cortical regions of interest further support this interpretation. Percent differences between FE-predicted and DIC-derived strains at a 20N load for representative specimens were lowest in UN and AT tibiae and highest in the UT tibia, consistent with the increased variance in DIC-derived strains in UT tibiae compared to other groups. These findings support previous studies reporting larger discrepancies between FE predictions and experimental results in altered or diseased bone relative to normal bone[17,18] and highlight the influence of tumor-induced heterogeneity on local mechanical behavior, features not captured in homogeneous FE models.

The selection of material properties strongly influenced model behavior. When FE stiffness was matched to mechanically-derived stiffness, the resulting elastic modulus was 3.56GPa, which is physiologically lower than expected for murine cortical bone[19]. In contrast, DIC-derived strains aligned closely with FE predictions using the literature-based cortical modulus value of 14.8GPa[16]. This suggests that mechanical testing underestimated stiffness due

to compliance within the testing setup, trabecular contributions, or other interface artifacts, and highlights the value of surface-level DIC measurements for validating FE models, particularly in heterogeneous bone where local mechanical behavior may not be reflected in global test measurements. Future studies should implement a CT phantom of known density and geometry to calibrate Hounsfield units to bone mineral density, reducing uncertainty while assigning density-based material properties and allowing for implementation of a heterogeneous material model that more accurately reflects bone behavior.

Finite element modeling inherently relies on several assumptions to simplify the complexity of bone structure and behavior, including homogeneity, isotropy, and simplified geometry. These approximations can limit the accuracy of model predictions and may contribute to the discrepancies observed in experimental measurements. Furthermore, node constraints within Abaqus limited resolution within the regions of interest; however, convergence analyses demonstrated acceptable variances, and the final models were able to capture both global stiffness and pre-yield spatial strain distribution. These results support the capability of FE models for assessing the linear elastic behavior of altered bone.

6.5 Conclusions

This study demonstrates the value of using DIC-derived and FE-predicted strain distributions in providing insight into the mechanical behavior of OS tumor-bearing and histotripsy-treated limbs. While homogeneous FE models accurately captured global stiffness in representative normal and ablated specimens, discrepancies observed in the unablated tumor-bearing tibia highlight the influence of tumor-induced structural heterogeneity on local mechanics. Surface-based DIC measurements revealed localized stiffening and strain heterogeneity that were not fully represented in the simplified FE model, emphasizing the importance of experimental validation, particularly when modeling diseased bone.

6.6 Acknowledgments

The authors gratefully acknowledge the support of the National Institutes of Health (NIH) [R01CA289288], the Veterinary Memorial Fund at Virginia Tech, the Focused Ultrasound Foundation, and the Virginia Tech COE EFO-O Program.

Works Cited

(1) Luo, Y.; Ahmed, S.; Leslie, W. D. *Comput. Methods Programs Biomed.* **2018**, *155*, 75–83.

(2) Leslie, W. D.; Luo, Y.; Yang, S.; Goertzen, A. L.; Ahmed, S.; Delubac, I.; Lix, L. M. *J. Clin. Densitom.* **2019**, *22*, 338–345.

(3) Imai, K. *World J Exp Med* **2015**, *5*, 182–187.

(4) Sternheim, A.; Giladi, O.; Gortzak, Y.; Drexler, M.; Salai, M.; Trabelsi, N.; Milgrom, C.; Yosibash, Z. *Bone* **2018**, *110*, 215–220.

(5) Matsumoto, T.; Ohnishi, I.; Bessho, M.; Imai, K.; Ohashi, S.; Nakamura, K. *Spine (Phila. Pa. 1976)* **2009**, *34*, 1464–1469.

(6) Brekhus, C.; Labus, K.; Seguin, B.; Puttlitz, C.; Gadomski, B. *Ann. Transl. Med.* **2024**, *12*, 5.

(7) Goyal, M.; Kalra, P. *Int. J. Sci. Res. (Raipur)* **2014**, *3*, 1848–1850.

(8) Shim, J.; Iwaya, C.; Ambrose, C. G.; Suzuki, A.; Iwata, J. *Sci. Rep.* **2022**, *12*, 8117.

(9) Tripp, J. A.; Squire, M. E.; Hedges, R. E. M.; Stevens, R. E. *Palaeogeogr. Palaeoclimatol. Palaeoecol.* **2018**, *511*, 462–471.

(10) Lindtner, R.; Kampik, L.; Putzer, D.; Klosterhuber, M.; Pallua, A. K.; Streif, W.; Schirmer, M.; Degenhart, G.; Arora, R.; Pallua, J. D. *Bioengineering (Basel)* **2025**, *12*.

(11) Thompson, M. S.; Schell, H.; Lienau, J.; Duda, G. N. *Med. Eng. Phys.* **2007**, *29*, 820–823.

(12) Lugas, A. T.; Terzini, M.; Stacchi, C.; Lombardi, T.; Di Donato, D.; Baldi, D.; Schierano, G.; Bignardi, C. *J. Phys. Conf. Ser.* **2022**, *2293*, 012011.

(13) Palanca, M.; Tozzi, G.; Cristofolini, L. *Int. Biomech.* **2016**, *3*, 1–21.

(14) Dickinson, A. S.; Taylor, A. C.; Ozturk, H.; Browne, M. *J. Biomech. Eng.* **2011**, *133*, 014504.

(15) Yang, B.; Irastorza-Landa, A.; Heuberger, P.; Ploeg, H.-L. In *ASME 2023 Verification, Validation, and Uncertainty Quantification Symposium*, American Society of Mechanical Engineers: Baltimore, Maryland, USA, 2023.

(16) Oliviero, S.; Roberts, M.; Owen, R.; Reilly, G. C.; Bellantuono, I.; Dall'Ara, E. *Biomech. Model. Mechanobiol.* **2021**, *20*, 941–955.

(17) Sas, A.; Sermon, A.; van Lenthe, G. H. *Sci. Rep.* **2022**, *12*, 7602.

(18) Soltani, Z.; Xu, M.; Radovitzky, R.; Stadelmann, M. A.; Hackney, D.; Alkalay, R. N. *Front. Bioeng. Biotechnol.* **2024**, *12*, 1424553.

(19) Chattah, N. L.-T.; Sharir, A.; Weiner, S.; Shahar, R. *Bone* **2009**, *45*, 84–90.

Chapter 7

Conclusions

This work establishes a comprehensive framework for evaluating the biomechanical effects of histotripsy on osteosarcoma tumor-bearing bone across preclinical and translational models. By combining mechanical testing, three-dimensional digital image correlation, μCT-based morphometric analysis, and finite element modeling, this framework directly links therapy-induced structural changes to the mechanical behavior of tumor-affected bone, contributing previously unexplored information to the field of osteosarcoma biomechanics.

In the clinical canine OS tissue study (Chapter 3), results indicate that histotripsy can selectively ablate *ex vivo* tumor tissue while preserving overall bone integrity, supporting its translational potential as a patient-specific, limb sparing treatment strategy for OS. In the preclinical murine OS whole bone study (Chapter 4), histotripsy preserved whole-bone mechanical strength while enhancing energy absorption and altering bone morphology, suggesting treatment-induced periosteal remodeling. The investigation of HIFU in a preclinical murine OS model (Chapter 5) revealed time-dependent ablation effects, supporting the capability of thermal focused ultrasound techniques to induce bone remodeling. Comparative DIC-FE analyses (Chapter 6) on histotripsy-treated bone demonstrated that homogeneous FE models capture global stiffness and general strain trends in both normal and ablated limbs, but less reliably predict local strains in untreated tumor-bearing limbs. These findings highlight the importance of accurate material property assignment and experimental validation. Together, these studies provide a foundation for translating histotripsy as a noninvasive, bone-sparing therapy for OS and for the mechanical characterization of OS

tumor-bearing limbs, advancing both preclinical understanding and the potential for clinical application.

A key objective of this work was to translate experimentally-derived structure-function relationships into a clinically relevant tool for noninvasively assessing fracture risk and guiding limb-sparing treatment of OS. The findings of this work support a reduced set of image-based, mechanically relevant parameters as primary determinants of whole-bone mechanical competence. Patients with preserved trabecular structure, low cortical porority, and high predicted failure load would be expected to tolerate treatment without increased fracture risk, while those with severe tumor-induced structural degradation may have an elevated risk of pathological fracture, requiring prophylactic placement or alternate interventions. Evaluation of post-yield mechanical behavior, such as energy absorption or toughness, provides additional insight into fracture resistance beyond stiffness and strength, which is particularly important for structurally compromised bone. The image-based modeling framework developed in this work enables patient-specific assessments of bone integrity and treatment eligibility. Integrating this approach with clinical imaging modalities such as HR-qPCT or CT will advance clinical translation, enabling noninvasive decision-making in limb-salvage strategies for OS.

While this work establishes a necessary foundation for characterization of OS and the effects of focused ultrasound techniques on OS-affected bone, extending these findings to a clinically relevant context remains a critical next step. Future studies should extend the μCT-derived relationships between material properties and mechanical behavior developed in this body of work to lower resolution clinical CT imaging to enable noninvasive, patient-specific assessments of bone integrity and treatment eligibility using clinically available imaging. Such adaptations could inform treatment planning and post-treatment management, including recommendations for load-bearing on the affected limb or prophylactic stabilization if necessary.

The FE models developed in this work rely on several assumptions to simplify the complexity of bone structure and behavior, including homogeneity, isotropy, linear behavior, and simplified geometry. These simplifications can introduce inaccuracies into model predictions, particularly in therapeutically altered or tumor-bearing bone. As demonstrated in this work, model fidelity is highly dependent on accurate representation of spatially heterogeneous material properties, particularly in tumor-bearing and treated bone. Incorporating disease-driven material property changes into subject-specific FE models will be essential for accurate fracture risk prediction. To this end, future studies could also incorporate more complex FE models that include damage or failure criteria to better predict comprehensive treatment effects. A well-characterized CT phantom should also be used to allow for heterogeneous material property assignment based on calibrated CT intensity. Additionally, complementary imaging approaches such as second harmonic generation (SHG) microscopy could be employed to quantify histotripsy's effects on collagen cross-linking in bone, a critical determinant of bone mechanical competence.

Another critical step in advancing histotripsy as a noninvasive, limb-sparing therapeutic option for OS is to define the dose-response relationships between histotripsy ablation parameters, including pulses per focal point and ultrasound energy output, and their effects on bone microstructure and whole-bone mechanical behavior. Establishing these relationships would enhance understanding of how varying histotripsy doses influence cortical and trabecular microarchitecture, local strain distributions, and global stiffness, all of which are essential for designing treatment protocols that maximize tumor ablation while preserving bone integrity. This understanding is particularly important in OS-affected limbs, which exhibit heterogeneous lytic and blastic lesions that may require spatially varying treatment doses across the tumor. Future studies could incorporate these findings into the DIC-FE framework developed in this work to allow for the development of predictive, patient-specific models capable of estimating fracture risk at varying treatment intensities and evaluating treatment eligibility.

Magnetic resonance imaging is a nonionizing imaging modality typically used for assessing soft tissue properties, but has become a standard tool in the staging, surgical planning, and treatment management of OS[1,2]. Integrating MRI with the image-based modeling framework developed in this work would enable evaluation of not only tumor-affected bone, but tumor regions with high soft tissue composition and surrounding musculature. To this end, future studies could integrate histotripsy treatment with MRI sequences sensitive to cortical bone, such as ultrashort echo time (UTE)[3,4] or pointwise encoding time reduction with radial acquisition (PETRA)[5], to complement μCT and FE analyses.

The mice used in the described studies were not skeletally mature, which can make it challenging to distinguish the effects of histotripsy from natural bone development driven by active growth plates in the tibia. Although skeletally immature mice better approximate the pediatric OS patient population, subsequent studies could use skeletally mature mice to further isolate histotripsy-specific effects. Mice are commonly employed in OS studies due to their genetic manipulability and well-characterized biology; however, the mechanical effects of tumor presence and histotripsy on trabecular bone, a key determinant of whole bone mechanical properties, remain underexplored, largely due to the small size of murine tibiae and their sparse trabecular network. Future studies could incorporate rat OS models, which have larger and denser limbs with more extensive trabecular architecture, providing a greater surface area for μCT-based morphometric analyses, high-resolution DIC strain assessments and FE predictions[6].

In summary, this work supports histotripsy as a noninvasive, limb-sparing therapeutic approach for OS that preserves the mechanical integrity of bone while achieving effective tumor ablation. Unlike conventional therapies that often degrade bone mechanical properties, histotripsy demonstrates the potential to preserve or enhance structural integrity, representing a shift in the treatment of bone malignancies. By linking morphological changes to mechanical behavior, this approach provides a foundation for patient-specific fracture risk prediction, treatment planning, and post-treatment management in OS and other bone malignancies.

Appendices

Appendix

Supplemental Information

Early time points post-histotripsy ablation exhibit altered cortical morphology but preserved mechanical behavior in tumor-bearing bone.

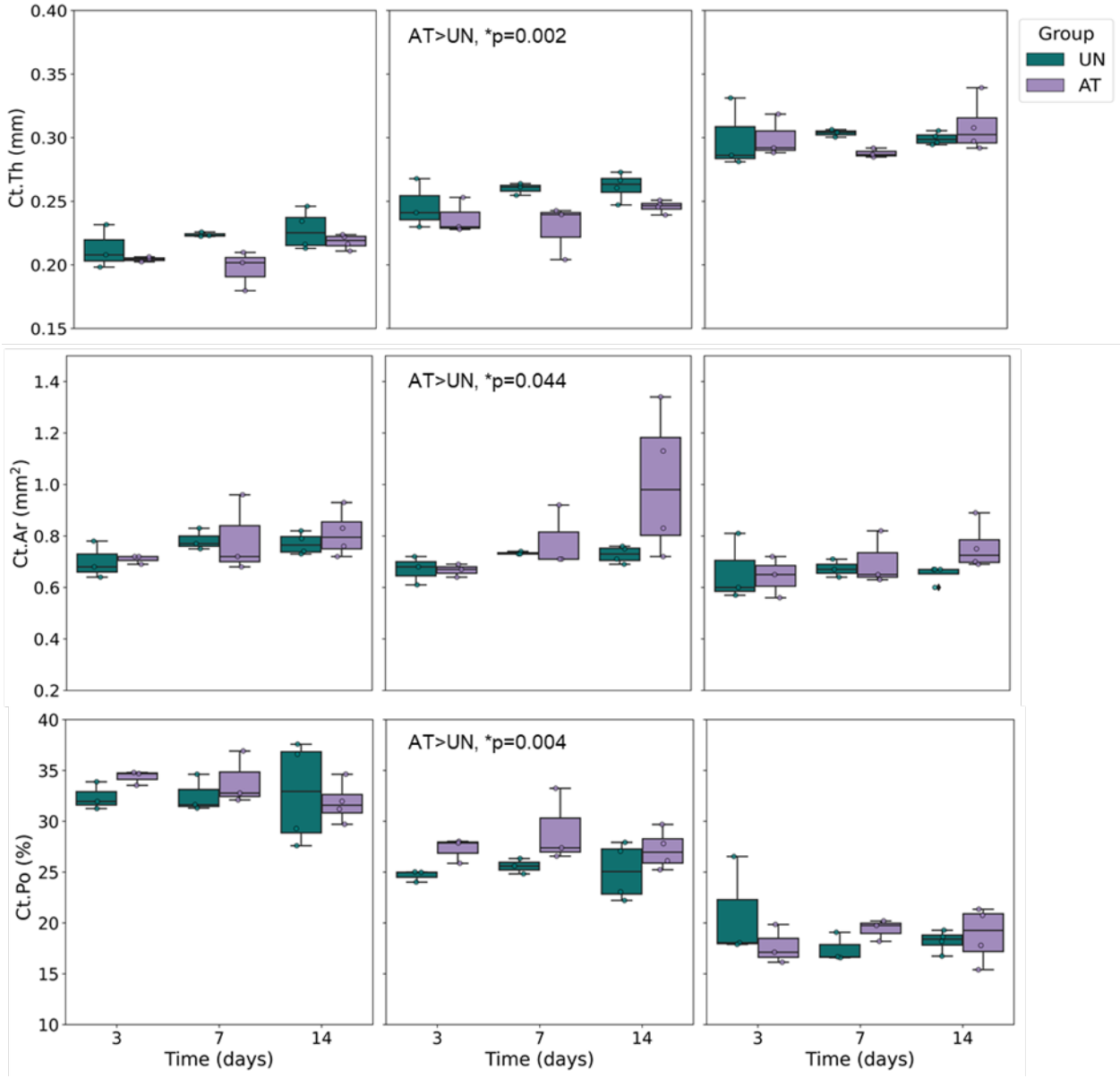

Figure 1: Morphometric data for unablated normal (UN) and ablated tumor-bearing (AT) groups 3, 7, and 14 days post-histotripsy ablation at each cortical site: a) 25%, b) 37%, and c) 75% distal to the proximal metaphysis. * indicates statistical significance ($p<0.05$) as determined by LMEM analysis.

Histotripsy induces a toughening effect and preserves mechanical integrity in normal bone despite morphometric changes 14 days post-ablation.

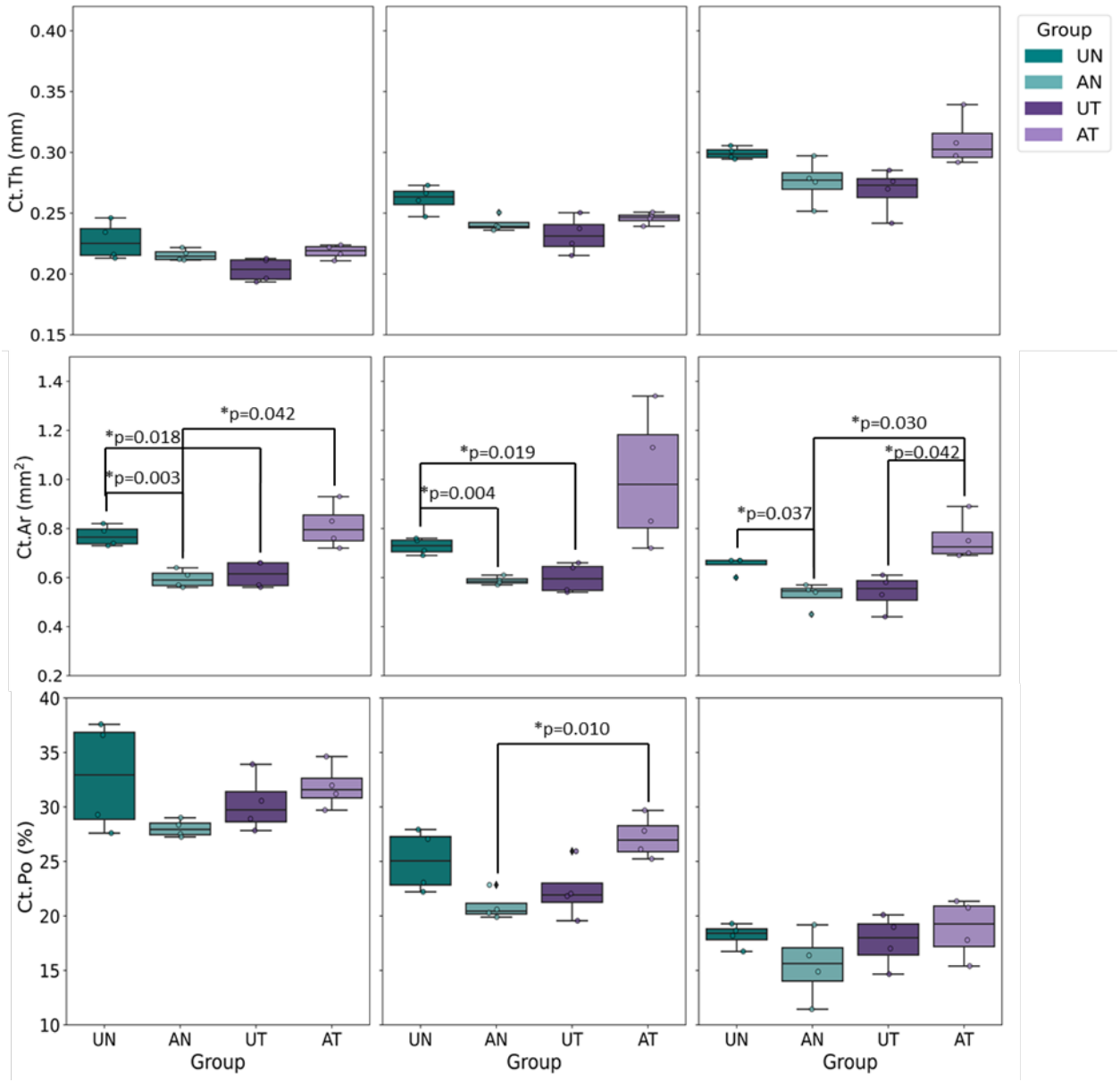

Figure 2: Morphometric data for all groups (UN, AN, UT, and AT) 14 days post-histotripsy ablation at each cortical site: a) 25%, b) 37%, and c) 75% distal to the proximal metaphysis. * indicates statistical significance ($p<0.05$) as determined by post-hoc analysis.

Distinct chronic effects of tumor burden and histotripsy ablation on normal bone 21 days post-ablation.

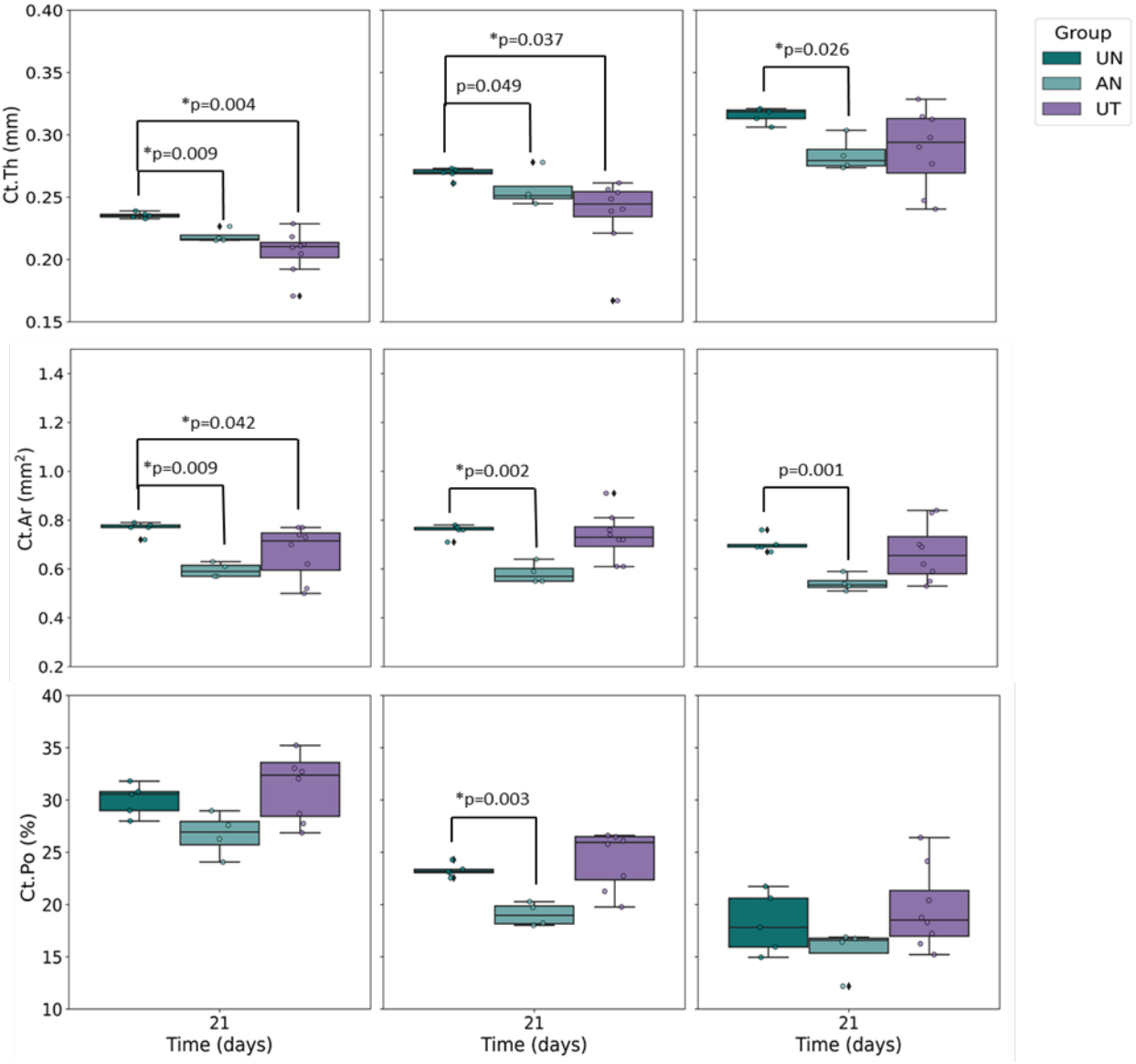

Figure 3: Morphometric data for unablated normal (UN), ablated normal (AN), and unablated tumor-bearing (UT) groups 21 days post-histotripsy ablation at each cortical site: a) 25%, b) 37%, and c) 75% distal to the proximal metaphysis. * indicates statistical significance ($p<0.05$) as determined by post-hoc analysis.

Curriculum Vitae

Preeya Achari

pfachari@vt.edu 212-729-8874

Education: **Virginia Tech, Blacksburg, VA**

- PhD Biomedical Engineering — May 2026
- B.S. Chemical Engineering — May 2020
- B.S. Biological Sciences — May 2020
  - Minor: Green Engineering

Research Experience:

Graduate Research Assistant, School of Biomedical Engineering and Sciences, Virginia Tech July 2022-Present

- Advisor: Dr. Caitlyn Collins, Assistant Professor, Department of Biomedical Engineering and Mechanics, Virginia Tech.
- Determining the mechanical effects of focused ultrasound-based cancer treatment on osteosarcoma tumor-affected bone via mechanical testing, medical image analysis, finite element modeling, and Python.
- Developing skills in computational modeling, mechanical testing methods, medical device optimization, grant writing, and academic/clinical collaborations.

Graduate Research Assistant, School of Biomedical Engineering and Sciences, Wake Forest University August 2020-July 2022

- Advisor: Dr. Boris Pasche, Professor, Department of Cancer Biology, Wake Forest University School of Medicine.
- Researched the therapeutic effects of amplitude-modulated radiofrequency electromagnetic fields (AM RF EMF) on cancerous cell lines using various cell culture methods.
  - *in vitro* work involved hepatocellular carcinoma cell lines HuH7 and Hep3B
  - *in vivo* work involved mammary tumor virus-neu (MMTVneu) mice
- Developed skills in cell culture, conducting various cellular assays including tritium assays, PCR, western blots, and proliferation/cytotoxicity assays on both normal and cancerous cells.

Undergraduate Researcher, Department of Chemical Engineering, Virginia Tech January 2017-May 2020

- Researched the molecular relationships between water and various chemical compounds using NAMD, LAMMPS, and Python for electronic device, sensor, and separation membrane applications.
  - Developed and optimized non-bonded interaction parameters between water molecules and substrates hexagonal-boron nitride and molybdenum disulfide.
  - Investigated computational models for curcumin and various metal-organic frameworks (MOFs) for potential use in cancer treatment.
  - Developed skills in using molecular dynamics simulation software, Python, and technical writing.

Unit Operations Lab, Denmark Technical University, Lyngby, Denmark July-August 2019

- Performed pilot plant experiments using equipment such as distillation columns, filter press, and evaporators.
- Discussed experimental data, analysis, and conclusions in the form of detailed technical reports.
- Created and presented a scaled-up heat exchanger prospect meeting specific heating requirements and costs.

Honors and Awards:

- ASBMR Student Cohort Program (April 2023-2025).
  - Granted free membership to society.
- Best Oral Presentation Award, ChEGSA Annual 2019 Symposium, Blacksburg, VA (March 2019).
  - 2nd place.
- Best Oral Presentation Award, Materials Research Society Fall 2018 Exhibit, Boston, MA (Nov. 2018).
  - Awarded in *Multiscale Modeling of Soft Materials and Interfaces* Symposium.

Presentations:

Oral Presentations

- **Achari, P.F.**, Vickers, E., Ruger, L., et al. "Biomechanical effects of histotripsy on osteosarcoma tumor tissue and normal bone". SBES Symposium, Virginia Tech, VA. (May 2024).
- **Achari, P.F.**, Bejagam, K.K, Singh, S., Deshmukh, S.A. "Development of non-bonded interaction parameters between hexagonal boron nitride and water". ChEGSA Annual 2019 Symposium, Blacksburg, VA. (March 2019).
- **Achari, P.F.**, Bejagam, K.K, Singh, S., Deshmukh, S.A. "Development of non-bonded interaction parameters between hexagonal boron nitride and water". Materials Research Society Fall 2018 Exhibit, Boston, MA. (Nov. 2018).

Poster Presentations

- **Achari, P.F.**, Vickers, E., Ruger, L., et al. "Tackling Heterogeneity- A Biomechanical Analysis of Histotripsy-treated and Untreated Bone". SB3C, Lake Geneva, WI. (June 2024).
- **Achari, P.F.**, Vickers, E., Ruger, L., et al. "Determination cof Biomechanical Effects of Histotripsy on Osteosarcoma in a Canine Comparative Oncology Model". SB3C, Vail, CO. (June 2023).
- **Achari, P.F.**, Vickers, E., Ruger, L., et al. "Determination of Biomechanical Effects of Histotripsy on Osteosarcoma in a Canine Comparative Oncology Model". SBES Symposium, Virginia Tech, VA. (May 2023).
- **Achari, P.F.,** McGrath, C.T., Jimenez, H., et al. "Inhibiting Breast Cancer Tumor Growth through Amplitude-Modulated Radiofrequency Electromagnetic Fields". SBES Symposium, Winston-Salem, NC. (May 2022).
- **Achari, P.F.**, Bejagam, K.K, Singh, S., Deshmukh, S.A. "Development of non-bonded interaction parameters between hexagonal boron nitride and water". Virginia Tech Chemical Engineering Research Symposium, Blacksburg, VA. (Apr. 2018).

Other abstracts

- Kabir, M.D.R., **Achari, P.F.**, Jing, Y., Collins, C.J., Han, A. *Speed of sound characterization in skull bone via microCT and ultrasound.* Acoustical Society of America Meeting, Honolulu, HI. (Dec. 2025).
- Kabir, M.D.R., **Achari, P.F.**, Jing, Y., Collins, C.J., Han, A. Investigation of skull bone speed of sound using computed tomography and ultrasound imaging. IEEE International Ultrasonics Symposium, Utrecht, Netherlands. Peer-reviewed conference proceeding. (Sep. 2025).

Publications:

- **Achari, P.F.**, Vickers, E., Ruger, L., Vlaisavljevich, E., Tuohy, J., Collins, C.J. (2026). Assessment of Histotripsy as a Bone-sparing Tumor Ablation Technique in Osteosarcoma Tumor-affected Limbs. *Frontiers in Veterinary Science,* 12.
- Sose, A.T., Mohammadi, E., **Achari, P.F.**, Deshmukh, S.A. (January 2022). Determination of accurate interaction parameters between the molybdenum disulfide and water to investigate their interfacial properties. *Journal of Physical Chemistry C*, 126, pp. 2013-2022.
- Blackstock, A.W., Benson, A., Kudo, M., Jimenez, H., **Achari, P.F.**, et al. (July 2021). Safety and efficacy of amplitude-modulated radiofrequency electromagnetic fields in advanced cellular carcinoma. *4Open*, 4.
- **Achari, P.F.**, Bejagam, K.K, Singh, S., Deshmukh, S.A. (April 2019). Development of non-bonded interaction parameters between hexagonal boron nitride and water. *Computational Materials Science*, 161, pp. 339-345.

Professional Outreach:

- HoChEs Virginia Tech Chemical Engineering Alumni Group — Feb. 2023-Present
  - Building a framework to increase diversity, alumni engagement, and student mentorship in the Department of Chemical Engineering at Virginia Tech.
- National Biomechanics Day lab tours — April 2023-2026
- CEED Women's Preview Weekend lab tours — April 2023-2024
- Judge, Behavioral and Social Sciences, Blue Ridge Highlands Regional Science Fair — March 2023-2026

Society Membership:

- American Society of Bone and Mineral Research (ASBMR) — January 2023-2025
- Inspiring Women in Lifelong Leadership (I WILL) Institute — August 2024-2026

Skills and Certifications:

- Proficient in Python, MATLAB, ABAQUS, Mimics
- Experienced in conducting independent research and writing technical reports/journal articles
- Excellent teamwork, management, and collaboration skills

Mentoring Experience:

- <u>Undergraduate students</u>
  - Ella Tomko
  - Lauren Mulligan
  - Kaayla Osborne
- <u>Graduate students</u>
  - Evan Carper
  - Hailey Levan
  - Bharath Kashyap